

**A New Grit Removal System for Applications in  
Municipal Wastewater Treatment Plants**

by

Biswajit Nandi

A thesis submitted in partial fulfillment of the requirements for the degree of  
Doctor of Philosophy  
in  
Water Resources Engineering

Department of Civil and Environmental Engineering  
University of Alberta

© Biswajit Nandi, 2016

## Abstract

There is a fundamental need to improve grit removal techniques for municipal wastewater treatment plants (WWTP) to meet newer effluent standards and to deal with the rapid growth of urbanization and industrialization. In response to this need, secondary and tertiary treatment processes are being developed, and these will continue to be limited without significant improvement of grit removal systems. Modern grit removal units separate fat, oil, grease and organic materials (hereafter named FOG) coated on grit particles by energetic turbulent flows followed by settling of the cleaned grit particles in quiescent flows contained in the same tank. Generating these two flows in a single tank is a problem due to complexities of tank design and operation. This research proposed a simplified grit removal system that comprised of a mixing tank equipped with multiple transverse jets for the separation of FOG and grit, and a grit tank for settling grit particles.

The preliminary experiments were carried out in a laboratory-scale hydraulic model of a mixing tank followed by a grit tank. The grit tank was a 1/15<sup>th</sup> scale model of a prototype aerated grit tank located at the Gold Bar WWTP in Edmonton, AB. The mixing tank, which was 42.7 cm square and 43.6 cm high, was set upstream of the grit tank.

Laboratory experiments included measurements of residence time distribution (RTD) and planar laser-induced fluorescence (PLIF). A total of 23 RTD

measurements were conducted with 18 repeats in the mixing tank, and six tests with three repeats were conducted in the PLIF measurements. The experimental variables were ten jet layouts ( $\Lambda$ ), six jet-Reynolds numbers ( $Re$ ) and two jet diameters ( $d$ ) in the RTD measurements to determine the values of  $\Lambda$ ,  $Re$  and  $d$  to achieve the maximum mixing performance of the mixing tank. Reynolds number of jets were varied in the PLIF measurements to test the effects of  $Re$  on the mixing performance and to visualize mixing flow in a plane.

Based on the laboratory experiments, a layout, diameter and a jet-Reynolds number were determined for field experiments at Gold Bar WWTP to test the effectiveness of the mixing tank in removing grit and FOG. Three repeated tests were conducted with the specified conditions of jets and other three repeated tests were conducted without jets (control test).

In analyzing the RTD measurements, a dispersive compartmental model (DCM) was developed with consideration of dispersive nature of the plug flow compartment. The DCM showed better performance in evaluating the effects of  $\Lambda$ ,  $Re$  and  $d$  on the mixing performance of the mixing tank than the conventional models of reactors. The best mixing performance of the tank was achieved at a layout with 8 jets, 5.3 mm diameter, and Reynolds number larger than 20600. In PLIF experiments, the DCM was used to estimate the mixing performance, which was reasonably matched with the mixing performance estimated in the RTD measurements. Mixing performance was increased with increases of Reynolds number larger than 16700, where dead flow zones were observed at a corner of

the tank. In the field experiments, the conditions of the tests with jets were the layout with eight jets, 5.3 mm jet-diameter, and Reynolds number of 41600. Reynolds number was increased to this value to ensure energetic turbulence that was required to clean grit from FOG. The results of the field experiments showed that concentration of total suspended solid (TSS) was reduced at the effluent of the grit removal system by 28.9% of influent to the system in the tests with transverse jets, whereas the tests without jet showed no significant difference in TSS between influent and effluent flows. The new system was able to remove larger amount of grit than the existing capacity of grit removal tank of Gold Bar WWTP. In addition, 95% of 44µm particles were removed in the new system. This indicated that the mixing tank was effective in cleaning grit from FOG that led to the settling of very fine particles in the grit tank.

This inclusion of a mixing tank for grit cleaning can be used in new WWTPs and, most importantly, can be easily added to the thousands of existing WWTPs in Canada to synergistically work with the other advanced technologies for meeting effluent standards.

## **Acknowledgements**

I would like to express my sincere gratitude to my supervisors, Dr. Mohamed Gamal El-Din and Dr. Mark Loewen, whose sincere patience, guidance, critiques and overall understanding on myself made this thesis completed. I deeply feel thankful to Dr. Gamal El-Din for introducing me the challenges of grit removal technologies. He showed his insight envision and encouraged me from the beginning to the end. I learned fascinating technologies from Dr. Loewen who allowed me to work on particle image velocimetry. He taught me on hands image processing, data acquisition, and problems associated with this technique. I could not reach at today's stage without his day-to-day directions.

I am very much thankful to Dr. Pamela Chelme-Ayala and Dr. Kerry McPhedran for their technical reviews, comments and recommendations on my dissertation and reports. I greatly appreciate Maria Demeter for assistance to my laboratory works. I also thank Perry Fedun and Chris Krath for their generous help in field works and laboratory setup. I am grateful to Abdul Mohammed and the staff of Gold Bar Wastewater Treatment Plant, Edmonton for their support. I am very much thankful to my friends and colleagues: Haitham Elnakar, Rajib Kamal, Shimiao Dong, Nian Sun, Zengquan Shu, Mohan Acharya, Ahmed Moustafa, Md Shahinoor Islam, Kai Wang, Mat Langford, and Vincent McFarlane.

This research was mainly funded by the Natural Sciences and Engineering Research Council of Canada (NSERC) and Edmonton Power Corporation (EPCOR) through a Collaborative Research and Development (CRD) Grant and through NSERC Discovery Grants to Drs. Mohamed Gamal El-Din and Mark Loewen. I am grateful for that support and the efforts that Drs. Gamal El-Din and Loewen did to assure continuous funding for me and my family during the entire Ph.D. duration.

Last but not the least, I would like to thank all of my family members for supporting me spiritually throughout writing this thesis and my life in general.

## Table of Contents

Chapter 1 : Introduction .....	1
1.1 Problem and Motivation.....	1
1.2 Background .....	4
1.3 Objectives.....	7
1.4 Outline of the Thesis .....	7
References.....	8
Chapter 2 Mixing with Multiple Transverse Jets in a Square Tank .....	14
2.1 Introduction .....	14
2.2 Experimental Setup .....	18
2.3 Experimental Methods .....	21
2.4 Analysis.....	24
2.5 Compartment model.....	26
2.6 Results .....	33
2.7 Conclusion.....	36
References.....	38
Tables.....	41
Figures.....	43
Chapter 3 : Planar Laser Induced Fluorescence (PLIF) Experiment in a Mixing Tank .....	62
3.1 Introduction .....	62
3.2 Experimental Setup and Methods .....	64
3.3 Analysis.....	68
3.4 Results .....	70

3.5	Conclusions .....	73
	Tables .....	84
	Figures .....	86
Chapter 4 : Field Assessment of a Model Grit Removal System at Gold Bar Wastewater Treatment Plant, Edmonton .....		
	4.1 Introduction .....	93
	4.2 Experimental Setup and Method .....	95
	4.3 Analysis .....	99
	4.4 Results .....	101
	4.4.1 Removal of TS and TSS .....	101
	4.4.2 Removal of Grit and FOG .....	103
	4.4.3 Grit Characteristics .....	105
	4.4.4 Significance of the New Grit Removal System .....	107
	4.4.5 Scale Effects .....	107
	4.5 Conclusion .....	111
	4.6 Reference .....	112
Chapter 5 : Conclusion .....		
	5.1 Summary of Conclusion .....	123
	5.2 Recommendations .....	125
	Reference .....	126
	Appendix .....	115

## List of Tables

Table 2.1: Layouts ( $A$ ) of transverse jets showing the position and number of jets by circles and crosses. Circles and crosses denote jets that are located on the near and far side walls, respectively. Arrows indicate direction of the mainstream flow. ....	41
Table 2.2: Layout ( $A$ ), Reynolds number ( $Re$ ) and jet diameter ( $d$ ) for all experiments. ....	42
Table 2.3: Hydraulic indices of an ideal PFR and perfect CSTR. ....	42
Table 3.1: Layouts ( $A$ ) showing the relative positions of cross jets by circles (open and closed), open circles are mounted on one sidewall and the closed on the opposite sidewall. Arrows are direction of mainstream flow. ....	84
Table 3.2: Test scenarios for the PLIF measurements. ....	84
Table 3.3: Fully mixed concentration, $C_{fm}$ over the plane and steady state concentration, $C_{ss}$ at the outlet for different Reynolds numbers. ....	85
Table 3.4: DCM predictions of plug flow volume, $V_p$ , mixed flow volume, $V_m$ and dead flow volume, $V_d$ using the RTD and PLIF measurements. ....	85
Table 4.1: Layouts ( $A$ ) showing the relative positions of cross jets by circles (open and closed), open circles are mounted on one sidewall and the closed on the opposite sidewall. Arrows are direction of mainstream flow. ....	115
Table 4.2: Test scenario for grit measurements at Gold Bar Wastewater Treatment Plant. ....	115
Table 4.3: Mean( $\mu$ ), probability (p-values), and efficiencies of removal ( $\eta$ ) of TSS, FSS and VSS, E0, E2 and E4 were the experiments without jets and E1, E3	

and E5 were the experiments with jets. TSS stands for total suspended solid, FSS for fixed suspended solid and VSS for volatile suspended solid. .... 116

Table 4.4: The fractions of volatile and fixed materials in solid and water phase, VS stands for total volatile solid, FS for total fixed solid and TS for total solid;  $f_{VS}$  and  $f_{FS}$  are fractions of volatile and fixed components in TSS, where TSS stands for total suspended solid, VSS for volatile suspended solid and FSS for fixed suspended solid. .... 116

Table 4.5: Estimates of grit removal capacity of this system and Gold Bar Wastewater treatment plant, Edmonton..... 117

Table 4.6: Analysis of grit size distribution of the tests, Habib(2008) and EWMCoE(2012)..... 117

Table A.1: Calculations for the differences of concentration of TSS, VSS, and the ratio of VSS/TSS and FSS/TSS, TSS = total suspended solid, VSS = volatile suspended solid, FSS = fixed suspended solid. ....115

Table A.2: Calculation of volatile and fixed fraction in scum, grit and water samples, TSS = total suspended solid, VSS = volatile suspended solid, FSS = fixed suspended solid, VS = volatile solid, FS = fixed solid and TS = total solid. ....115

Table A.3: Calculation of grit mass, FSS = fixed suspended solid, FS = fixed solid, and GBWWTP = Gold Bar Wastewater Treatment Plant, MGD = million gallon per day. ....116

Table A.4: Calculation of scum mass, FSS = fixed suspended solid, FS = fixed solid, and GBWWTP = Gold Bar Wastewater Treatment Plant, MGD = million gallon per day. ....116

## List of Figures

Fig. 2.1: Experimental setup for RTD measurements [MT: mixing tank, CHT: constant head tank, P1 and P2: centrifugal pumps; M1 and M2: magnetic flow meters; T1 and T2: tracer injection ports; V1,V2 and V3: globe valves].....	43
Fig. 2.2: Side view of the mixing chamber showing transverse jet position in circles [all dimensions are in cm]. .....	43
Fig. 2.3: Time series of raw, filtered and background corrected concentration for a single RTD measurement [ $A = H$ , $Re = 21600$ , $d = 5.3$ mm, run number 07], $C_r$ : raw concentration, $C_f$ : filtered concentration, and $C_f - C_b = C$ , injection time is 69.6s.....	44
Fig. 2.4: Cumulative exit age curve or F-curve for an experimental run with $A = H$ , $d = 5.3$ mm and $Re = 21603$ . $\theta$ is defined as dimensionless time, and $\theta_b$ , $\theta_{10}$ , $\theta_{50}$ and $\theta_{90}$ are the dimensionless times when 1% , 10%, 50% and 90% of tracer is recovered.....	44
Fig. 2.5: E-curves predicted using the (a) Axial Dispersion Model for different dispersion numbers, $N_D$ and (b) Tank in Series Model for different equivalent tank numbers, $N_T$ . Plots are based on mean residence time $\tau = 19.7$ s. ....	45
Fig. 2.6: Schematic diagram of the Dispersive Compartmental Model showing the plug, mixing and dead flow compartments: $V_p$ is the plug flow volume, $V_m$ is the mixed flow volume, and $V_d$ is the dead flow volume of a mixing tank; $Q =$ mainstream flow rate.....	46
Fig. 2.7: (a) E-curves and (b) F-curves predicted using the Dispersive Compartmental Model for various $v_p$ and $v_m$ , where $N_d = 0.01$ , $v_d = 0$ and $\tau = 19.7$ s. [here $b$ varies for varying $v_p/v_m$ ]. .....	47

Fig. 2.8: (a) E-curves and (b) F-curves predicted using the Dispersive Compartmental Model for arbitrary  $v_p$  and  $v_d$ , where  $v_m = 50\%$  and  $N_d = 0.01$  and  $\tau = 19.7$  s. [ here  $b$  varies for varying  $v_p/v_m$ ]. ..... 48

Fig. 2.9: (a) E-curves and (b) F-curves predicted using the Dispersive Compartmental Model for various  $v_m$  and  $v_d$ , where  $v_p = 50\%$  and  $N_d = 0.01$  and  $\tau = 19.7$  s. [ here  $b$  varies for varying  $v_p/v_m$ ]. ..... 49

Fig. 2.10: (a) E-curves and (b) F-curves predicted using the Dispersive Compartmental Model for various  $N_d$  and for constant value of  $v_m = v_p = 50\%$  and  $\tau = 19.7$  s. [here  $b$  varies for varying  $N_d$ ]. ..... 50

Fig. 2.11: Four model predicted E-curves are compared with the experimental E-curve of a test with a low mixed flow volume [ $A = H$ ,  $d = 3.8$  mm,  $Re = 5147$ ; Model parameters are:  $N_D$  of ADM is 0.34,  $N_T$  of TiSM is 2,  $v_p$  and  $v_m$  of CCM are 23%, 65% respectively and  $v_p$ ,  $v_m$ ,  $N_d$  and  $b$  of DCM are 30.3% , 45.8%, 0.02, 0.73 respectively]. ..... 51

Fig. 2.12: : Four model predicted E-curves are compared with the experimental E-curve of a test with a high mixed flow volume [ $A = H$ ,  $d = 5.3$  mm,  $Re = 26840$ ; Model parameters are:  $N_D$  of ADM is 0.24,  $N_T$  of TiSM is 2,  $v_p$  and  $v_m$  of CCM are 25.3%, 73.5% respectively and  $v_p$ ,  $v_m$ ,  $N_d$  and  $b$  of DCM are 31.9.3% , 66.8%, 0.013, 0.79 respectively]. ..... 51

Fig. 2.13: Experimental E-curves for two  $\Lambda$  with similar Reynolds number  $Re$ , where  $Re = 21400$  for  $\Lambda = C$  and  $Re = 21600$  for  $\Lambda = B$ , and  $d = 5.3$  mm for both tests. .... 52

Fig. 2.14: Experimental E-curves for two different number of jets ( $N_j$ ) with similar  $Re$ , where  $Re = 20700$  for  $A = B$  and  $Re = 21400$  for  $A = J$ , and  $d = 5.3$  mm for both tests. .... 52

Fig. 2.15: Experimental E-curves for two different  $Re$  with same layout  $A$ , where  $A = H$ ..... 53

Fig. 2.16: Plots of hydraulic indices  $\bar{\theta}_i$ ,  $\bar{\theta}_p$  and  $\bar{\theta}_{10}$  versus layout,  $A$  in (a) to (c) and versus Reynolds number,  $Re$  in (d) to (f).  $\bar{\theta}_i$  = mean dimensionless arrival time,  $\bar{\theta}_p$ = mean dimensionless time to peak and  $\bar{\theta}_{10}$  = mean dimensionless time to capture 10% tracer.. 54

Fig. 2.17: Plots of hydraulic indices  $\bar{\theta}_g$ ,  $\bar{\theta}_{50}$  and  $\bar{\theta}_{90}$  against layout,  $A$  in (a) to (c) and against Reynolds number,  $Re$  in (d) to (f). Dashed lines indicate standard values of the hydraulic indices for a perfect CSTR.  $\bar{\theta}_g$  = mean dimensionless residence time,  $\bar{\theta}_{50}$ = mean dimensionless median time and  $\bar{\theta}_{90}$  = mean dimensionless time to capture 90% tracer.. 55

Fig. 2.18: Means values of the dispersion number,  $\bar{N}_D$  obtained from axial dispersion model for varying (a) layout,  $A$  and (b) Reynolds number,  $Re$  and diameter,  $d$ . Note that each data point is the average of 14 to 18 repeated tests. . 56

Fig. 2.19: Means values of the dispersion number,  $\bar{N}_d$  of the plug flow compartment, obtained from dispersive compartmental model for varying (a) layout,  $A$  and (b) Reynolds number,  $Re$  and diameter,  $d$ . Note that each data point is the average of 14 to 18 repeated tests. .... 56

Fig. 2.20: Dispersive Compartmental Model estimated  $b$  for different (a) layouts,  $A$  and (b) Reynolds numbers,  $Re$  and diameters,  $d$  of jets. .... 57

Fig. 2.21: Dispersive Compartmental Model estimated volumes of percentages of plug flow volumes,  $v_p$ , mixed flow volumes,  $v_m$  and dead flow volumes,  $v_d$  for different layouts,  $A$  and with  $Re = 21,400$  and  $d = 5.3\text{mm}$ . Error bars are margin of error at the 95% confidence limit. .... 58

Fig. 2.22: Dispersive Compartmental Model estimated percentages of plug flow volume,  $v_p$ , for different Reynolds number,  $Re$  and jet diameter,  $d$ ..... 59

Fig. 2.23: Dispersive Compartmental Model estimated percentages of plug flow volume,  $v_p$ , for different Reynolds number,  $Re$  and jet diameter,  $d$ ..... 60

Fig. 2.24: Dispersive Compartmental Model estimated percentages of dead flow volume,  $v_d$ , for different Reynolds number,  $Re$  and jet diameter,  $d$ ..... 61

Fig. 3.1: A schematic diagram of PLIF setup showing a laser sheet, positions of laser and camera, and directions of mainstream flows and locations of cross jets. .... 86

Fig. 3.2: Concentration of fluorescent dye Rhodamine 6G,  $C$  ( $\mu\text{g/L}$ ) versus pixel intensity,  $P$ , measured at laser energy of 120 mJ(100%); The  $R^2$  value of the calibration curve is 0.980..... 86

Fig. 3.3: Position of field of view in the tank and Instantaneous concentration map, measured at  $t/\tau = 1.0$  in an experiment with Layout = B, Reynolds number = 10765 and diameter of a jet = 5.3 mm, where  $t$  = time and  $\tau$  = mean residence time. .... 87

Fig. 3.4: Time series plot of  $C/C_{ss}$  where  $C$  = concentration of tracer and  $C_{ss}$  = steady state concentration defined as the average concentration from  $t = 65$  to 85 sec at outlet. Solid line is model F-curve by Dispersive Compartmental Model (DCM), and dots are experimental values of F-curve. [Layout = B, diameter of jet = 5.3mm and Reynolds number = 27353]. .... 87

Fig. 3.5: Instantaneous concentration maps at  $t/\tau = 0.2, 0.5, 1.0, 2.0, 3.0$  and  $4.0$  of a PLIF experiment with Layout A (no jets)..... 88

Fig. 3.6: Instantaneous concentration maps at  $t/\tau = 0.2, 0.5, 1.0, 2.0, 3.0$  and  $4.0$  of a PLIF experiment with Layout B, Reynolds number of 27378 and jet-diameter of 5.3mm. .... 89

Fig. 3.7: Time series of dimensionless outlet concentration  $C/C_{ss}$  for varying Reynolds number,  $Re$ .  $C_{ss}$  is steady state concentration and  $\tau$  is residence time . [Layout A for  $Re = 0$  , and Layout B, and diameter of jets of 5.3 mm for all other  $Re$ ]..... 90

Fig. 3.8: Dimensionless concentration  $C_{ss}/C_{ss0}$ , where  $C_{ss}$  is average steady state concentration for the period of 65 to 85 sec, and  $C_{ss0}$  is the average concentration at outlet for Reynolds number (a)  $Re = 0$ , (b)  $Re = 10700$ , (c)  $Re = 16700$  and (d)  $Re = 27400$ . Diameter of jets were 5.3mm. .... 91

Fig. 3.9: Percentage of mixed flow volume,  $V_m$ , plug flow volume,  $V_p$  and dead flow volume,  $V_d$  for varying Reynolds number, estimated by DCM. .... 92

Fig. 4.1: Photo of experimental setup showing the components: (1) constant head tank, (2) mixing tank, (3) grit tank, (4) manifold for cross jets, (5) flow meter for the longitudinal flow and (6) flow meter for the transverse flow; Arrows show the flow direction. .... 118

Fig. 4.2: Imhoff cone experiment showing three samples of each of the two tests; Settleable grit is shown at bottom of the cones with black colors. .... 118

Fig. 4.3: Grit wash in a long settling tube, (A) shows final wash and (B) shows an initial wash of two samples. .... 119

Fig. 4.4: Concentrations of TFS and TVS at inlet and outlet; TFS stands for total fixed solid and TVS stands for total volatile solid. Error bars represent corresponding margin of errors ; E0, E2 and E4 were the experiments without jets and E1, E3 and E5 were the experiments with jets..... 120

Fig. 4.5: Concentrations of FSS and VSS at inlet and outlet; FSS stands for fixed suspended solid and VSS stands for volatile suspended solid. Error bars represent corresponding margin of errors; E0, E2 and E4 were the experiments without jets and E1, E3 and E5 were the experiments with jets..... 120

Fig. 4.6: Entrance section of the grit tank showing scum layer on the top of the water..... 121

Fig. 4.7: Settleable solids measured by Imhoff settling cone in the experiments with and without transverse jets; E0, E2 and E4 were the experiments without jets and E1, E3 and E5 were the experiments with jets..... 122

Fig. 4.8: Sieve analysis of grit deposit in the grit tank; E2 and E4 were the experiments without jets and E1, E3 and E5 were the experiments with jets; G1,G2 and G3 are the distributions of EWMCoE (2012) and H1 is the distribution of Habib(2008). ..... 122

## Chapter 1 : Introduction

---

### 1.1 Problem and Motivation

The clean water crisis is the highest global risk based on social impact (WHO 2015). Globally, municipal wastewater treatment plants (WWTPs) are cleaning trillion gallons of water each day. The cleaning processes and operations involve various levels of treatment, starting from preliminary to tertiary treatment (Tchobanoglous et al. 2003). At preliminary treatment, grit removal tanks are installed typically downstream of screen bars to remove inorganic grit particles, which are commonly agglomerated with fat, oil and grease (FOG) and other organic materials. The grit removal tanks are the first crucial unit operation. The failure of these tanks results in reduced capacity and effectiveness of downstream treatment units, such as membrane bioreactors, aeration tanks with fine bubble diffusers, and other biological and chemical reactors (Mansour-Geoffrion et al. 2010). Such failure also results in blockage in pipes and channels, as well as wear and tear to centrifuges, pumps, and other mechanical parts (Gang et al. 2010). Captured grit particles are collected from grit tanks and washed prior to landfill disposal. As a result, the failure of grit tanks also increases the cost of washing units. Thus, the operation and maintenance costs of a WWTP are increased, and the total capacity of the plant is reduced (Osei et al. 2010).

Scientific research on grit removal tanks is less common and less developed (do Prado and Campos 2009) than studies of secondary and tertiary treatment units, even though grit removal tanks may be responsible for up to one third of the operational costs of WWTPs (Wilson 1985). The efficiency of grit tanks is found to be declining in many WWTPs (Sherony and Herrick 2011). Moreover, the grit problems are increasing because the amount of grit particles (Le Cornu et al. 2000) and FOG (Pilli et al. 2011) is rapidly increasing in municipal WWTPs due

to urbanization. Therefore, it is essential to develop a functionally and economically effective grit removal unit.

Design of traditional grit removal tanks, governed by the settling velocities of discrete particles, is relatively very simple. These tanks are typically long rectangular channels. These are relatively long as the settling velocities of grit with FOG are less than those of clean grit particles. Moreover, extra channel length is required to retard entrance and exit turbulence (USJDAAF 1988). Aerated and vortex grit tanks add advantages over these traditional tanks by separating FOG from grit particles prior to settling of grit. Aerated grit tanks generate a helicoid flow about the longitudinal axis of a long tank using multiple transverse air jets. Vortex type tanks develop a vortex flow pattern about the vertical axis in cylinder-like or conical-like tanks. The energetic turbulent flow zone of these tanks is followed by a weak turbulent flow zone where clean particles settle. Several design factors control the development of adequate vortices in turbulent zones and a smooth separation of two dissimilar flow zones. Geometric configuration, airflow rates, position and spacing of air jets, total number of air nozzles, diameters of nozzles, and positions of baffling and geometric configuration are major design factors in aerated grit tanks (Sawicki 2004; Morales and Reinhart 1984). Velocities of inflow, outflow, underflow and overflow, shape and size of tanks and rotation of paddle are major factors in vortex type tanks (USEPA 2003). The relationship among the design factors is not well understood for aerated grit tanks (Sawicki 2004) or vortex tanks (Vatistas et al. 2005). As a result, these tanks are designed based on conventional shapes, which are developed based on many years of operational experiences. Aerated tanks are not environmentally friendly as organic materials generate odor, produce harmful volatile compounds and emit gases like methane due to aeration in these tanks (Wang et al. 2011). Capital and operational costs of both types of tanks are high (Anderson and Holmberg 2006). Moreover, it is expensive to modify vortex tanks as these tanks are mostly proprietary. These problems can be

solved by designing a simple tank, keeping the advantageous functions of the aerated and vortex tanks.

The primary function of the modern grit removal tank, especially aerated grit tank, is the creation of two dissimilar flows in the same tank. An energetic turbulent flow is required to separate organic coatings from the heavy inorganic grit particles, and a quiescent flow is required to allow settling of the grit particles. Generating these dissimilar flow conditions in the same tank is very difficult in terms of both the design and operation. This problem can be addressed by performing the two functions in separate tanks, which may be more efficient and cost effective than existing aerated grit tanks. The idea of splitting the two flow zones into separate tanks minimizes the design factors and ends in a simple geometry, low capital cost and easy operation. A simple square tank, known as a mixing tank could be used to separate organic coatings from grit particles using an energetic turbulent flow. A rectangular tank located downstream of the mixing tank, known as the settling tank could be used to capture clean grit particles. This idea of splitting flow zones has been used for separating grit particles from runoff water (Puprasert et al. 2004), where a strong turbulent zone in a conical vessel is followed by a weak turbulent zone in a grit pot. The two split flow zones in the conical vessel and the grit pot performed better than a conventional single vessel hydrocyclone. Brenner and Diskin (1991) experimented with the use of water jets instead of air jets in aerated grit tanks for generating a turbulent flow zone to separate coatings from grit particles. In the mixing tank, the energetic turbulent flow zone is developed by multiple transverse water jets mounted on the sidewalls. The positive results of Brenner and Diskin's (1991) experiments motivated us to develop the idea to use water jets in the mixing tank, which in turn reduces operational cost as operating water pumps is less expensive than air blowers (Sarikaya 1992).

The present study developed a new grit removal technique that was more efficient and has larger capacity than existing grit tanks. The addition of a mixing tank

equipped with transverse-jets was proposed that effectively separated FOG from grit and this cleaned grit can then be removed more efficiently in a downstream settling tank. Pilot-scale experiments were conducted to determine the transverse-jet configuration and operating conditions that produce homogeneous and energetic mixed flow condition in the mixing tank. Moreover, field experiments were completed at Gold Bar Wastewater Treatment Plant (GBWWTP), Edmonton, AB to determine the effectiveness of the new grit removal technique when processing real wastewater. The research results can be directly applied to existing Canadian WWTPs to improve grit removal efficiency and enhance the entire wastewater treatment process.

This research outcome is particularly important for the many WWTPs, which are upgrading their downstream secondary and tertiary units by introducing biotechnology-based techniques with no modification of grit removal units (Gravette et al. 2000). These downstream units need effective and efficient grit removal units, where the new grit removal approach with the mixing tank would be an effective solution. These mixing tanks could also be used to improve the capacity of existing aerated grit tanks. Presently, environmental regulators are imposing more controls on effluent quality for a better environment (Environment Canada 2010). This new grit removal technique should help to improve effluent quality and cope with the challenge of increasing grit and FOG loads in sewer flows to WWTPs.

## **1.2 Background**

Clean grit particles are heavy inorganic particles, ranging from a micron to a millimeter in size (Osei et al. 2010), while FOG and other organic materials are light particles, ranging in size from a nanometer to a micron (Coca et al. 2011; Kwon et al. 2009). These organic materials which may contain obnoxious components (Osei and Andoh 2008) are sorbed onto the surface of clean grit particles (Pignatello and Xing 1995) creating thick organic coatings that cause the grit particles to become less dense.

Under ideal conditions, grit removal tanks remove all fine and coarse particles in sewer flows, usually the particles in suspension and near the bed of sewers (Wilson et al. 2007). There is no strict guideline on the cut-point particle size, the size of particles to be removed completely from the water flow. Setting the cut point particle at 210 micron (65- mesh) is commonly accepted for designing grit tanks (Tchobanoglous et al. 2003). Current practice in many aerated grit tanks is to remove 95% of 100 micron particles (Munoz and Young 2009). However, the cut point particle size for effective membrane bioreactors is 75-106 micron (Andoh and Neumayer 2009). The challenges are increasing day after day to design grit tanks for very low cut-point particle sizes. It is not surprising that the increasing prevalence of pharmaceutical particles (~ 30 micron) is expected to lower the cut-point particle size.

Effective grit removal directly depends on grit cleaning efficiency, and the grit cleaning is a function of the factors that influence the coating formation. Brownian motion, fluid shear stress and differential velocities all affect the agglomeration of organic materials onto the surface of grit particles in sewer flows (Pedocchi and Piedra-Cueva 2005). The strength of this agglomeration is the result of the cumulative effect of the cohesive forces in the coating materials (Soos et al. 2008), and is a function of the material properties of the continuum phase (wastewater) and the coatings (Selomulya et al. 2002; Sarimeseli and Kelbaliyev 2004). The thickness of this agglomeration and surface texture of grit particles also affect the yield strength of the coatings (Ahimou et al. 2007).

The coating materials are separated from the grit when the external applied stresses are higher than the yield stress of the material (Bridgeman et al. 2010). Turbulent jets in a confined space are capable of generating high external stresses on the particles. These external forces that can separate coatings are either drag or lift forces. In turbulent flows, coated particles undergo lift forces (Magnus forces) due to spinning or drag forces (Pankajakshan et al. 2010). In pure shear flow only drag forces act to separate coatings from the particles. In many engineering

applications, these hydrodynamic stresses are applied in processes that contain fluid-particles mixtures. Washing organic contaminants from sediments (Libralato et al. 2008), breaking flocs (Yuan and Farnood 2010), separating particles of different specific gravities (Dueck et al. 2009) and oil film separation from sand particles (Matvienko and Evtushkin 2007) are all examples of applying turbulent jets in confined spaces. In these applications, turbulent stresses and turbulent energy dissipation rates are related to the cleaning, separation and/or breaking processes.

The mixing tanks are mixing reactors, where strong and uniform turbulent mixing lead to a high cleaning efficiency. Average turbulent mixing characteristics are typically studied by comparing two idealized reactors: the plug flow reactor (PFR) and the continuous stirred tank reactor (CSTR). In a PFR, fluid is mixed instantly in the transverse flow direction with no dispersion in the longitudinal flow direction, whereas in a CSTR, fluid is mixed instantly in all directions. Ideally, a perfect mixing tank is a CSTR and a settling tank is a PFR. However, practical mixing and settling tanks are not ideal. For the non-ideal reactors, mixing characteristics are quantified by two common models; the axial dispersion model and the tank-in-series model. The coefficient of axial dispersion,  $D$ , is used to describe how close the reactor is to a plug flow, where  $D = 0$  for an ideal PFR and  $D = \infty$  for an ideal CSTR. The tank-in-series model results in a number of equivalent CSTR,  $N$  which describes how close to an ideal CSTR the reactor is, where  $N = 1$  for an ideal CSTR and  $N = \infty$  for an ideal PFR.

The turbulent kinetic energy of water jets injected into a confined mixing tank is irrecoverable, as the energy dissipates in the tank via viscous mechanisms (Oldshu 2004). This dissipation has two components. The first is direct dissipation caused by gradients in the mean velocity components. The second is the dissipation caused by gradients in the turbulent velocity components, referred to as turbulent dissipation (Frohnafel et al. 2008). A small part of the dissipated energy works on separating coating materials from grit particles. The majority of

the dissipated energy is converted to heat without doing any work on the particles. The grit particles will follow numerous paths from the tank entrance to exit, and move through different flow regimes inside the tank, and thus are exposed to different dissipation rates and stresses. Boller and Blasé (1998) studied forces on aggregated flocs in different turbulent flow regimes. Ibemere and Kresta (2007) quantified turbulent intensities in different zones of a stirred tank to understand the mixing mechanism in these zones. Turbulent intensity increases with increases of applied kinetic energy of transvers jets. The kinetic energy is a function of the operating condition of jets. It is the challenge to determine the operating condition of jets and the separation of coating.

### **1.3 Objectives**

The ultimate goal of the proposed research is to provide an effective grit removal technique, where efficient grit cleaning in a mixing tank leads to an efficient separation of grit and organic materials in a settling tank. The critical objective is to demonstrate the hypothesis that the application of water jets is efficient and effective in cleaning grit particles in a mixing tank. The specific objectives of the proposed research are listed below:

- (1) Conduct experiments to determine the transverse-jet configuration and operating conditions that produce large dispersion numbers in the mixing tank.
- (2) Visualize mixing flow in a plane of the mixing tank to study mixing behavior for a range of operating conditions.
- (3) Conduct a series of experiments at the Gold Bar WWTP to determine if the new grit removal technique operates effectively when processing real wastewater.

### **1.4 Outline of the Thesis**

This dissertation is organized as follows. Chapter 2 presents experimental studies of mixing in the square tank. This chapter includes the development of a new

model to investigate the mixing characteristic of turbulent flows in a tank. This chapter determines the configurations of jets and operating condition. Chapter 3 shows the mixing flow in a plane for varying operating conditions of transverse jets based on the best configuration obtained in Chapter 2. The results of the Chapters 2 and 3 are used to carry out field experiments that are described in Chapter 4. The performance of the model in removing grit is presented in this chapter.

## References

Ahimou, F., Semmens, M. J., Novak, P. J., and Haugstad, G. (2007). "Biofilm cohesiveness measurement using a novel atomic force microscopy methodology." *Appl. Environ. Microbiol.*, 73(9), 2897-2904.

Anderson, R., and Holmberg, M. (2006). "Energy Conservation in Wastewater Treatment Operation." Lund University, Sweden: Master Thesis.

Andoh, R. Y. G., and Neumayer, A. (2009). "Fine Grit Removal Helps Optimize Membrane Plants." *WaterWorld*, 25(1), 28-28.

Boller, M., and Blaser, S. (1998). "Particles under stress." *Water Science and Technology*, 37(10), 9-29.

Brenner, A., and Diskin, M. H. (1991). "Model study of jet-circulated grit chamber." *J. Environ. Eng.*, 117(6), 782-787.

Bridgeman, J., Jefferson, B., and Parsons, S. A. (2010). "The development and application of CFD models for water treatment flocculators." *Adv. Eng. Software*, 41(1), 99-109.

Coca, J., Gutiérrez, G., and Benito, J. (2011). "Treatment of Oily Wastewater." *Water Purification and Management*, 1-55.

do Prado, G. S., and Campos, J. R. (2009). "The use of image analysis to determine particle size distribution of grit carried by sewage." *Engenharia Sanitaria E Ambiental*, 14(3), 401-410.

Dueck, J., Pikushchak, E., and Minkov, L. (2009). "Modelling of change of the classifier separation characteristics by water injection into the apparatus." *Thermophysics and Aeromechanics*, 16(2), 247-258.

Environment Canada. (2010). *Wastewater Systems Effluent Regulations*. Canada.

Frohnappfel, B., Lammers, P., and Jovanović, J. (2008). "The role of turbulent dissipation for flow control of near-wall turbulence." *New Results in Numerical and Experimental Fluid Mechanics VI*, 268-275.

Gang, D. D., Rakesh, B., and Shankha, B. (2010). "Wastewater: Treatment Processes." *Encyclopedia of Agricultural, Food, and Biological Engineering, Second Edition*, 1(1), 1825-1836.

Gravette, B., Strehler, A., Finger, D., and Palepu, S. (2000). "Troubleshooting a Grit Removal System." *Proceedings of the Water Environment Federation*, 2000(11), 332-369.

Ibemere, S., and Kresta, S. (2007). "Modelling the Mixing and Dissolution Kinetics of Partially Miscible Liquids." *Chem.Eng.Res.Design*, 85(5), 710-720.

Kwon, B., Shon, H. K., and Cho, J. (2009). "Characterizations of Colloidal Organic Matter Isolated from Surface Water." *Sep.Sci.Technol.*, 44(13), 3224.

Le Cornu, P., Faram, M., and Andoh, R. (2000). "A Novel Device for the Removal of Grits and Oils." *CIWEM/AETT Millennium Conference; 'Wastewater Treatment: Standards and Technologies to meet the Challenges of the 21st Century'*, 727-738.

Libralato, G., Losso, C., Arizzi, N. A., Citron, M., Della, S., Stefano, Zanutto, E., Cepak, F., and Volpi Ghirardini, A. (2008). "Ecotoxicological evaluation of industrial port of Venice (Italy) sediment samples after a decontamination treatment." *Environmental Pollution*, 156(3), 644-650.

Mansour-Geoffrion, M., Dold, P. L., Lamarre, D., Gadbois, A., Deleris, S., and Comeau, Y. (2010). "Characterizing hydrocyclone performance for grit removal from wastewater treatment activated sludge plants." *Minerals Eng*, 23(4), 359-364.

Matvienko, O., and Evtushkin, E. (2007). "Theoretical investigation of the process of cleaning oil-polluted soil in hydrocyclone apparatuses." *Journal of Engineering Physics and Thermophysics*, 80(3), 502-510.

Morales, L., and Reinhart, D. (1984). "Full-Scale Evaluation of Aerated Grit Chambers." *Journal (Water Pollution Control Federation)*, 56(4), pp. 337-343.

Munoz, A., and Young, S. (2009). "Two-dimensional model for predicting performance of aerated grit chambers." *Canadian Journal of Civil Engineering*, 36(9), 1567-1578.

Oldshu, J. Y. (2004). "Fluid Mixing." *Encyclopedia of Physical Science and Technology*, 79-104.

Osei, K., and Andoh, R. (2008). "Optimal Grit Removal and Control in Collection Systems and at Treatment Plants." ASCE.

Osei, K., Mody, A., and Andoh, R. Y. G. (2010). "Field assessment of grit removal systems." *World Environmental and Water Resources Congress 2010: Challenges of Change, May 16, 2010 - May 20*, American Society of Civil Engineers, Providence, RI, United states, 3756-3763.

- Pankajakshan, R., Mitchell, B. J., and Taylor, L. K. (2010). "Simulation of unsteady two-phase flows using a parallel Eulerian–Lagrangian approach." *Comput.Fluids*.
- Pedocchi, F., and Piedra-Cueva, I. (2005). "Camp and Stein's Velocity Gradient Formalization." *J.Environ.Eng.*, 131 1369.
- Pignatello, J. J., and Xing, B. (1995). "Mechanisms of slow sorption of organic chemicals to natural particles." *Environ.Sci.Technol.*, 30(1), 1-11.
- Pilli, S., Bhunia, P., Yan, S., LeBlanc, R., Tyagi, R., and Surampalli, R. (2011). "Ultrasonic pretreatment of sludge: A review." *Ultrason.Sonochem.*, 18(1), 1-18.
- Puprasert, C., Hebrard, G., Lopez, L., and Aurelle, Y. (2004). "Potential of using Hydrocyclone and Hydrocyclone equipped with Grit pot as a pre-treatment in run-off water treatment." *Chemical Engineering and Processing: Process Intensification*, 43(1), 67-83.
- Sarikaya, H. Z. (1992). "Discussion of" Model Study of Jet-Circulated Grit Chamber"." *J.Environ.Eng.*, 118(6).
- Sarimeseli, A., and Kelbaliyev, G. (2004). "Modeling of the break-up of deformable particles in developed turbulent flow." *Chemical Engineering Science*, 59(6), 1233-1240.
- Sawicki, J. M. (2004). "Aerated grit chambers hydraulic design equation." *J.Environ.Eng.*, 130(9), 1050-1058.
- Selomulya, C., Bushell, G., Amal, R., and Waite, T. (2002). "Aggregation mechanisms of latex of different particle sizes in a controlled shear environment." *Langmuir*, 18(6), 1974-1984.

Sherony, M., and Herrick, P. (2011). "A fresh look at an old problem: Design criteria for effective grit removal." *Journal of New England Water Environment Association*, 45(1), 25-31.

Soos, M., Moussa, A. S., Ehrl, L., Sefcik, J., Wu, H., and Morbidelli, M. (2008). "Effect of shear rate on aggregate size and morphology investigated under turbulent conditions in stirred tank." *J. Colloid Interface Sci.*, 319(2), 577-589.

Tchobanoglous, G., Burton, F., and Stensel, H. D. (2003). *Wastewater Engineering: Treatment and Reuse*. McGraw Hill, NY.

USEPA. (2003). "Wastewater Technology Fact Sheet, Screening and Grit Removal."  
[Http://Water.Epa.Gov/Aboutow/Owm/Upload/2004\\_07\\_07\\_septics\\_final\\_sgrit\\_removal.Pdf](http://Water.Epa.Gov/Aboutow/Owm/Upload/2004_07_07_septics_final_sgrit_removal.Pdf), dated Nov 15, 2011.

USJDAAF. (1988). "Domestic Wastewater Treatment." *Technical Manual, no. 5-814-3/AFM 88-11, United States Joint Department of the Army and Air Force*; 3.

Vatistas, G. H., Jawarneh, A. M., and Hong, H. (2005). "Flow characteristics in a vortex chamber." *Can.J.Chem.Eng.*, 83(3), 425-436.

Wang, J., Zhang, J., Xie, H., Qi, P., Ren, Y., and Hu, Z. (2011). "Methane emissions from a full-scale A/A/O wastewater treatment plant." *Bioresour.Technol.*, 102(9), 5479-5485.

WHO, U. (2015). "Progress on Sanitation and Drinking Water: 2015 Update and MDG Assessment." *Geneva: World Health Organization*.

Wilson, G. E. (1985). "Is there grit in your sludge?" *Civil Engineering—ASCE*, 55(4), 61-63.

Wilson, G., Tchobanoglous, G., and Griffiths, J. (2007). "The Nitty Gritty." *Water Environ.Technol.*, 19(9), 115-118.

Yuan, Y., and Farnood, R. R. (2010). "Strength and breakage of activated sludge flocs." *Powder Technol*, 199(2), 111-119.

## Chapter 2 Mixing with Multiple Transverse Jets in a Square Tank<sup>1</sup>

---

### 2.1 Introduction

The efficient removal of inorganic grit particles is a major concern in many municipal wastewater treatment plants (WWTPs). Inefficient grit removal causes operational and maintenance problems downstream in the WWTP (Gang *et al.* 2010). Grit removal is hampered when the inorganic particles are coated with organic material, referred to as FOG or fat, oil and grease, making them more buoyant. If the FOG can be separated from the grit, the particles settle more rapidly and the grit removal is more efficient. Grit is often cleaned by using compressed air jets in aerated grit tanks, which are not commonly designed for removing grit finer than 210 micron (Tchobanoglous *et al.* 2003). The air jets generate transverse spiral motions and produce a velocity field with energetic turbulent flow in the upper region and quiescent flow in the lower region (Morales and Reinhart 1984). The system is designed in such way that the strong velocity gradients occurring in the upper region produce shear stresses that separate FOG and grit, while quiescent flow allows the settling of grit particles (Hay 1946). Generating the two opposite flow conditions in a same tank is a tough challenge from the design and operational points of view. Aerated grit tanks produce odor and harmful volatile components due to aeration with putrescible materials in water (Habib 2008). Aeration, which involves compressing and injecting air into water, is expensive and has high operational costs (Anderson and Holmberg 2006). In the last half century, there has not been any major change in the design of aerated grit tanks (Gravette *et al.* 2000). However, Environment Canada (2010) has identified approximately 1,000 WWTPs that need to be

---

<sup>1</sup> A version of this chapter will be submitted to The Canadian Journal of Chemical Engineering

upgraded in order to meet national effluent standards. To achieve this goal, upgrading the grit removal system is imperative. The upgrading is also urgent in order to cope with the increasingly large amounts of FOG and grit associated with the growth of cities and industries (Pilli 2011; Cornu et al. 2000), and to remove fine grit particles for meeting stringent national effluent standards.

In order to achieve an effective separation of FOG from grit, the factors that determine the strength of the organic coatings are to be considered. Coating materials agglomerate on the surface of grit particles due to Brownian motion, fluid shear forces, and differential velocities (Pedocchi et al. 2005). The strength of this agglomeration is the result of the cumulative effect of cohesive forces in the coating materials (Soos et al. 2008). This strength is a function of the material properties of the continuum phase (wastewater) and the coatings (Selomulya et al. 2002; Sarimeseli and Kelbaliyev 2004). The coating materials are removed from the grit when the external applied stresses are higher than the yield stress of the material (Bridgeman et al. 2010).

Turbulent water jets in a confined space are used in many engineering applications to process fluid particle mixtures. Washing out organic contaminants on sediments, (Libralato *et al.* 2008), breaking flocs (Yuan and Farnood 2010), damage of plant cells (MacLoughlin *et al.* 2000) and animal cells (Chisti 2001), separating particles of different specific gravity (Dueck *et al.* 2009), and oil film separation from sand particles (Matvienko and Evtyushkin 2007) are all examples of applying turbulent jets in confined spaces. In these applications, turbulent stresses and energy dissipation rates are related to removal, breaking or damages.

Brenner and Diskin (1991) demonstrated the use of water jets instead of air jets to reduce operational cost in a model aerated grit tank. In this study, experiments were conducted to relate jet-flows with water velocities at several control locations to confirm spiral motion and quiescent flows. The developing two dissimilar flows in the tank was considered a difficult task, similar to that in an

aerated grit tank. The study opened up the idea of using water jets for grit removal system in WWTPs. However, the separation of FOG from grit was not investigated which is considered an important step for developing an effective grit removal system. In another study, Habib (2008) investigated a mixing reactor equipped with multiple transverse jets to determine the bulk mixing characteristics of the reactor. The study was limited within a small range of experimental factors; however, estimated characteristics of a mixed flow tank in which turbulent shear stresses possibly could separate FOG from grit were not investigated. Therefore, the design and operational complexities of aerated grit tanks can be avoided and costs can be reduced by introducing a mixing tank in series with a settling tank as a new grit removal system for WWTPs. This system performs two functions. The mixing tank, located just upstream of a settling tank, performs FOG separation from grit. Several water jets inject high momentum into the mixing tank from sidewall to generate intense turbulence to separate the FOG. This tank requires no aeration. It is a simple cubical shaped tank with the same width of the downstream settling tank. The second tank is a traditional type-settling tank, which generates a quiescent flow to settle previously cleaned grit at the bottom and to float separated FOG at the surface. Capital costs of the mixing tank are very low, because of its simple geometric shape. The costs of grit tanks are also low, as a smaller space is required for settling particles due to the increase of particle settling velocities and for simplicity in the design. Replacing air jets with water jets reduces substantial operational costs because of inexpensive pump operation instead of expensive compressor and blower (Sarıkaya 1991). The advantages of this grit removal system are that the designs of the tank are simple, and operating costs are substantially reduced compared to those in existing aerated grit tanks.

Research challenges remain in designing a mixing tank for effective cleaning grit. The grit cleaning is effective when there is a strong and uniform turbulent stresses so that FOG coated grit are exposed to the stresses. The flow with strong turbulent

stresses possibly leads to a uniform mixed flow in a tank. Then the mixing characteristics of the tank are assumed to be functionally related to the configurations and operating conditions of transverse jets. Therefore, as a first step of the research for the effective grit cleaning, it is reasonable to determine the conditions of transverse jets that generate uniform mixed flow or close to a uniform mixed flow in a tank.

A mixing tank with spaces where turbulent jets are used is referred to as a mixing reactor. The reactor is typically described by their bulk mixing characteristics considering two idealized reactors. Two idealized reactors are defined: the plug flow reactor (PFR) and the continuous-stirred tank reactor (CSTR). In a PFR, fluid is fully mixed in the radial direction and not in the axial direction, whereas in a CSTR, fluid is perfectly mixed in all directions. Mixing characteristics of a reactor is studied by residence time distribution (RTD), which is a tracer concentration at outlet for injection of tracer at inlet. In a perfect CSTR, RTD shows an instant peak and an exponential decay for pulse injection of a tracer at inlet. In an ideal PFR, RTD is a Dirac-delta function at a delayed time. In non-ideal reactors, RTD is used to compute hydraulic indices, which are the time when the peak, mean, and a specified percentage of a tracer are detected. Characterizing mixing by hydraulic indices is fast and good as initial interpretation of the flow pattern of the reactor (Liem *et al.* 1999). The bulk mixing characteristics are determined by using a tank in series model (TiSM) or an axial dispersion model (ADM). Besides, there are several compartmental models of Levenspiel (1999) used to understand the details of the mixing characteristics. In compartmental models, the total tank volume is compartmentalized to plug flow, mixed flow and dead flow compartments. Compartmental models determine the mixing characteristics of each compartment.

The overall objective of this study is to obtain a jet configuration that approaches to a uniform mixed flow in a square tank. In order to achieve the jet configuration,

a dimensional analysis was carried out to relate a model parameter of uniform mixed flow with the jet-parameters as experimental factors. Then, a series of tracer study (RTD experiments) was conducted to obtain a model parameter by applying RTD models. A new RTD model was developed based on the compartmental models of Levenspiel (1999) to quantify the effects of experimental factors. Finally, a design criterion was proposed that approaches to a complete mixed flow in a square tank with multiple transverse jets.

## **2.2 Experimental Setup**

A series of RTD measurements was conducted on a model scale-mixing tank at the University of Alberta. The model mixing tank, which was used by Habib (2008) and available at the University, was selected for this present study because of its simple geometry. The geometric variability of the tank was not considered in this study because the priority was to prove the effectiveness of the technology with the mixing tank in series with a grit tank. The grit tank, which was used by Habib (2008), was a 1/15<sup>th</sup> scale model of an aerated grit tank of Gold Bar Wastewater Treatment Plant, Edmonton, and this tank was used in the present study. The experimental setup is shown in Fig. 1, including the 42.7 cm square and 43.6 cm deep mixing tank. Pump P1 (BVE-S75, Monarch, Canada) supplied the longitudinal mainstream flow in the mixing tank by pumping water from the sump tank to the constant head tank, which delivered a constant flow rate to the mixing tank. The longitudinal flow rate was held constant at 3.5 L/s and the water depth at 41.5 cm in the tank throughout the entire study. The second pump P2 (66-1-1/4 WE, Baldor, China) was used to supply water from the sump tank to a manifold that evenly distributed water to multiple transverse jet nozzles located on either side of the mixing tank as illustrated in Fig. 1. Fig. 2 shows twelve possible jet-locations for mounting nozzles. The mainstream and jet flow rates were controlled by two globe valves, V1 and V2 and the water level in the tank was controlled by valves V3 and V4. The flow rates were monitored using two magnetic flow meters: M1 (MAG2IC-050PA1LSDAAAT2-XX-X, FoxBoro,

Japan) for the mainstream flow, and M2 (IMT25-SEATB10K-BG, FoxBoro, China) for the jet flow. The tracer used for the RTD measurements was injected into the inlet pipes through two injection ports T1 and T2 as shown in Fig. 1 and 2.2. Fig. 1 also shows a 2.4 m long grit tank that maintains a constant water level in the mixing tank. The grit tank was 1/15<sup>th</sup> scale of an aerated grit of Gold Bar Wastewater Treatment Plant, Edmonton, and that was also available in the University.

A dimensional analysis was used to reduce the number of independent variables. In this study, the dependent variable should be a measure of mixing homogeneity, which in this case can be quantified by using one of three variables: dispersion number, the number of tanks, or mixed flow volume. The dispersion number  $N_D$  is a dimensionless parameter from the axial dispersion model, defined by  $N_D = D_a/U_a L_a$ , where  $D_a$  (m<sup>2</sup>/s) is the dispersion coefficient,  $U_a$  (m/s) is axial velocity, and  $L_a$  (m) is an axial length. This number measures the turbulent diffusivity along the direction of  $U_a$ . The number of tanks,  $N_T$  is a parameter of the tank in series model (TiSM) and it is defined as the number of completely mixed flow tanks in a series. These two variables by their definitions are dimensionless. However, the mixed flow volume,  $V_m$ , which has a dimension of  $L^3$ , is a parameter in the compartmental model defined as the volume of completely mixed flow inside the tank. Any one of these variables could be used as the dependent variable; however, the mixed flow volume ( $V_m$ ) was selected for this dimensional analysis. The goal is to maximize the value of  $V_m$ , which is related to a number of independent variables as shown in the following equation,

$$V_m = f_1(\Lambda, u, d, U, D, L, H, \rho, \mu, g) \quad (2.1)$$

where,  $\Lambda$  is the jet layout,  $u$  is the jet velocity,  $d$  is the jet diameter,  $U$  is the inlet velocity of the mainstream flow,  $D$  is the diameter of the pipes,  $L$  is the horizontal dimension of the mixing tank,  $H$  is the water depth,  $\rho$  is the density of water, and

$\mu$  is the absolute viscosity of water. The jet layout  $\Lambda$  is defined by the jet configuration, i.e., the number of cross jets and their positions on the sidewalls. The dimensional analysis reduces Eq. (2.1) to the following dimensionless equation,

$$\frac{V_m}{V_T} = f_2 \left( \Lambda, \frac{u}{U}, \frac{D}{d}, \frac{H}{d}, \frac{L}{d}, Re, Fr \right) \quad (2.2)$$

where,  $V_m/V_T$  is the fractional mixed flow volume,  $V_T = HL^2$  is the volume of the tank,  $u/U$  is the dimensionless jet velocity,  $D/d$  is the dimensionless diameter of the inlet and outlet pipes,  $H/d$  is the dimensionless water depth,  $L/d$  is the dimensionless horizontal length of the mixing tank,  $Re = \rho ud/\mu$  is the jet Reynolds number, and  $Fr = U/\sqrt{gH}$  is the Froude number of the longitudinal flow.

The number of dimensionless variables was reduced to three by excluding  $u/U$ ,  $D/d$ ,  $H/d$ ,  $L/d$  and  $Fr$  from Eq. (2.2) because the values of  $U$ ,  $D$ ,  $H$  and  $L$  were held constant in all experiments,  $\rho$  and  $\mu$  were assumed constant because the water temperature was held approximately constant at  $21^\circ\text{C} \pm 2^\circ\text{C}$ , and the influence of  $u$  and  $d$  were combined in  $Re$ . This reduces the Eq. (2.2) to the following equation,

$$\frac{V_m}{V_T} = F(\Lambda, Re) \quad (2.3)$$

A number of dimensional groups ( $D/d$ ,  $H/d$  and  $L/d$ ) related to  $d$  were excluded in the dimensional analysis, and, therefore, the effect of the jet diameter  $d$  was investigated after evaluating the relationship established in Eq. (2.3).

Based on the dimensional analysis, the experiments were conducted in which  $\Lambda$ ,  $Re$  and  $d$  varied to determine what layouts and Reynolds numbers produced  $V_m/V_T$  approaching unity. In the first set of experiments,  $Re$  was held constant at 21,400 and ten different layouts,  $\Lambda$  were tested (please refer to Table 2.1). The layout producing the largest mixed flow volume was held constant for the next set of experiments, in which  $Re$  varied up to 27,000. In addition to these tests, the effect

of  $d$  was investigated by testing two different diameters. The values of  $A$ ,  $Re$  and  $d$  for all the tests are listed in Table 2.2.

### 2.3 Experimental Methods

The method used to introduce the tracer was pulse injection and potassium chloride (KCl) was used as the tracer material. KCl was used because it is inexpensive and nonreactive. For producing a pulse injection, the tracer must be injected quickly enough so that the pulse injection approximates a Dirac-delta function (Liem *et al.* 1999). In injecting the tracer material, manual syringes were used and 40 mL of KCl from each syringe was injected manually. In ten trial injections, the time required to inject 40 mL was recorded using a stopwatch and the average duration was  $0.40 \pm 0.06$  sec. Thirumirthi (1969) recommended that to simulate a pulse injection the tracer should be injected quicker than  $1/50^{\text{th}}$  of theoretical residence time, where theoretical residence time is the ratio of the volume of a reactor and the flow rate through the reactor. The measured injection time of 0.4 s meets this criterion because the theoretical residence time for the mixing tank was 22 s.

Time series of the KCl concentration were measured on the centerline of the outlets using two conductivity probes (YSI 3418, USA) and two conductivity meters (YSI 34, USA). A data acquisition (DAQ) system consisting of a PC equipped with a DAQ board (AT-MIO 16XE -50, National Instrument, Austin, TX) and LabVIEW (National Instrument, Austin, TX) software was used to digitize the voltage signals from the conductivity meters at a sampling frequency of 400 Hz. In order to measure the background concentration, the DAQ system was triggered manually to start acquiring data for a period of at least 30 sec prior to the tracer injection. Data were collected for approximately 5 min after injecting the tracer. The time at which the tracer was injected was measured using a stopwatch, which was manually synchronized with the start time of the data acquisition system. Each experiment was repeated 18 times to reduce the

statistical uncertainty. The digital time series of voltage data from each experiment was then converted to time series of concentration using three calibration factors.

The calibration factors were  $K_1$ , which converted voltage ( $V$ ) to conductivity ( $S$ ),  $K_2$  converted conductivity to specific conductivity ( $S'$ ), and  $K_3$  converted specific conductivity to concentration ( $C$ ). Seven KCl aqueous solutions were used, with the concentrations ranging from 0.0 to 1.0 g/L. The calibration factor  $K_1$  was determined by inserting the probe into each KCl solution and recording the digital voltage using the DAQ system for a period of 4 to 5 seconds and then computing a time average voltage. At the same time, conductivity readings were manually recorded from the conductivity meter. The voltages and conductivities of the seven KCl solutions were used to compute a linear regression of  $S = K_1 V$  and the value of  $K_1$  was obtained. The second calibration factor  $K_2$  is called the cell constant of the probe, which is needed to account for possible erosion of the platinum electrode coatings. The cell constant is the ratio of the standard conductivity (1.414 mS/cm) of a 0.01M KCl aqueous solution at 25<sup>0</sup>C and the measured conductivity of that solution at 25<sup>0</sup>C. This factor is determined by using the relationship  $S' = K_2 S$ . The conductivity of a 0.01M KCl solution was measured at a room temperature of 20.6<sup>0</sup>C, and corrected to a temperature of 25<sup>0</sup>C using the standard thermal correction equation (AWWA 1998). The measurements were repeated five times to reduce the random error. The value of  $K_2$  was obtained by averaging the ratios of the standard and temperature compensated measured conductivities. The third calibration factor  $K_3$  was obtained by performing a linear regression analysis of  $C_r = K_3 S'$ , where the values of  $C_r$  were known and  $S' = K_2 K_1 V$ . In these regression analyses for determining  $K_3$  and  $K_1$ ,  $R^2$  values were larger than 0.9997. In determining  $K_2$ , the margin of error was less than 3% at the 95% confidence limit.

A MATLAB (R2012a, 7.14.0.739, Mathworks, USA) program was written to process the digital voltage time series sampled from the conductivity meters. The

program first loaded a raw voltage-time series and then converted it to a raw concentration-time series,  $C_r(t)$  using the calibration factors. Time series of  $C_r(t)$  were processed to estimate power spectrum density by using a MATLAB tool, *pwelch*. The estimates of the power spectrum density led to select 5 Hz as a cut off frequency for removing high frequency noise. Details of the noise removal analysis are presented in Appendix B. The raw concentration-time series was passed through a low pass digital filter to remove high frequency noise and a filtered concentration-time series,  $C_f(t)$  was obtained. The low pass filter was an 8<sup>th</sup> order “Butterworth” filter with a cutoff frequency of 5 Hz that was selected after evaluating the frequency spectra of  $C_r(t)$ . The background concentration  $C_b$  was estimated by averaging  $C_f(t)$  for a period from the start time of data acquisition to a time just prior to the tracer injection, which was typically 30 to 50 sec.  $C_b$  was then subtracted from  $C_f(t)$  to obtain the final concentration  $C(t)$ . A typical raw, filtered and final concentration time series are plotted in Fig. 3. This figure shows that the raw data contained noise that was removed by the low pass filter. The final time series concentration  $C(t)$  was the response at an outlet for impulse tracer injection at an inlet in the mixing tank. This time series was used for subsequent RTD analysis.

In subsequent RTD analysis, each  $C(t)$  time series was converted to an exit age curve or E-curve  $E(t)$  and to a cumulative exit age curve  $F(t)$ . The equations for computing these curves are,

$$E(t) = \frac{C(t)}{\int_0^{\infty} C(t)dt} \quad (2.4)$$

$$F(t) = \int_0^t E(t)dt \quad (2.5)$$

The E-curve is a probability density function and, therefore, it satisfies the following equation,

$$\int_0^{\infty} E(t) dt = 1 \quad (2.6)$$

RTD measurements are considered reliable if the tracer mass detected at the outlet is at least 90% of the injected tracer mass (AWWA 1991; Liem *et al.* 1999). The total mass of tracer detected at the outlet  $M_{outlet}$  is given by,

$$M_{outlet} = Q \int_0^{\infty} C(t) dt \quad (2.7)$$

where  $Q$  is the volumetric flow rate in the tank. This criterion was applied to the 18 repeated runs of each test and in all cases at least 14 of the runs met this criterion.

## 2.4 Analysis

An initial assessment of the tank mixing was carried out by extracting hydraulic indices from the cumulative exit age curves  $F(t)$  and comparing these indices to values for ideal PFR and perfect CSTR (Wahl *et al.* 2012). The hydraulic indices used in the analysis were  $t_i$ ,  $t_{10}$ ,  $t_p$ ,  $t_{50}$ ,  $t_g$  and  $t_{90}$ , where,  $t_i$  is the initial time when 1% of tracer is recovered;  $t_{10}$ ,  $t_{50}$  and  $t_{90}$  are the times when 10%, 50% and 90% tracer is recovered;  $t_p$  is the time when the peak tracer concentration is detected; and  $t_g$  is the mean time of a RTD curve. These indices are typically divided by the mean residence time,  $\tau$  to make them dimensionless; here  $\tau = V/Q$ ,  $V$  is the volume of water and  $Q$  is the mainstream flow rate. The value of  $\tau$  was 21.9 s when there was no transverse jet and it decreased for increasing flow rates of transverse jets. The dimensionless hydraulic indices defined by dividing  $t_i$ ,  $t_{10}$ ,  $t_p$ ,  $t_{50}$ ,  $t_g$  and  $t_{90}$  by  $\tau$  are  $\theta_i$ ,  $\theta_{10}$ ,  $\theta_p$ ,  $\theta_{50}$ ,  $\theta_g$  and  $\theta_{90}$ , respectively. Fig. 4 shows a typical plot of  $F(t)$  and the corresponding dimensionless hydraulic indices. Hydraulic indices of the standard reactors are listed in Table 3. An ideal PFR has hydraulic indices that are equal to unity, because in this case  $C(t)$  is a  $\tau$ -delayed Dirac-delta function for the Dirac-delta input at time  $t = 0$ . A perfect CSTR has  $\theta_p = 0$  because the peak value

occurs at  $t = 0$  due to instantaneous mixing of the tracer. The hydraulic indices related to the percentages of tracer mass recovery were obtained by using the Eq. (2.4), which was derived from the exit curve of a perfect CSTR described in Levenspiel (1999),

$$\theta_x = -\log_e(1 - x\%) \quad (2.8)$$

Two simple RTD models for non-ideal reactors, the one-dimensional (1-D) ADM and the TiSM (Levenspiel 2012), were used to investigate the bulk mixing in the tank (Philipossian and Mitchell 2003). The 1-D ADM, uses the advection diffusion equation to estimate the dispersion number  $N_D$ ; and the TiSM is used to compute the equivalent tank number,  $N_T$ . These model parameters,  $N_D$  or  $N_T$  were obtained by fitting the modelled E-curves to the experimental E-curves.

The ADM model E-curves were obtained by first solving the following advection diffusion equation

$$\frac{\partial C}{\partial t} + U \frac{\partial C}{\partial x} = D \frac{\partial^2 C}{\partial x^2} \quad (2.9)$$

where,  $C$  is the instantaneous tracer concentration,  $U$  is the average axial velocity, and  $D$  is the axial dispersion coefficient. The boundary conditions are  $C = 0$  at  $x=0$  and  $\partial C/\partial x = 0$  at  $x = L$ , where  $L$  is the axial length of the reactor. Analytical solution of this problem is possible if the flow does not deviate much from an ideal PFR ( $N_D \sim 0.01$ ) and the boundary condition is open-open (Levenspiel 2012). However, the boundary condition of the mixing tank was closed-closed as there was a sudden expansion at the inlet and a sudden contraction at the outlet. The Reynolds number of the longitudinal flow was 22000, which indicated that the flow in the mixing tank would have significantly more dispersion than that in a PFR (Hart *et al.* 2013). Therefore, the Eq. (2.9) was solved numerically using a finite difference scheme and the computed  $C(t)$  curves were then substituted into the Eq.(2.4) to obtain the modelled E-curves.

The TiSM E-curves were computed by combining the effects of a series of  $N_T$  CSTRs. The concentration time series of concentration,  $C(t)$  or C-curve of a single CSTR is given by,

$$C(t) = C_0 e^{-t/\tau} \quad (2.10)$$

where  $C_0$  is the inlet concentration,  $\tau$  is the mean residence time, and  $t$  is time. The C-curve of  $N_T$  CSTR in series is given by,

$$E_{th}(\theta) = N_T \frac{(N_T \theta)^{N_T-1}}{(N_T - 1)!} e^{-N_T \theta} \quad (2.11)$$

where  $\theta = \frac{t}{\tau_t}$  and  $\tau_t$  is the combined residence time of  $N_T$  CSTRs. The E-curves predicted by using these two models are plotted in Fig. 5 for a range of  $N_D$  and  $N_T$  values. Larger values of  $N_D$  and smaller values of  $N_T$  are associated with a high degree of mixing. For a perfect CSTR,  $N_T = 1$ , whereas for an ideal PFR  $N_D = 0$  (Philipossian and Mitchell 2003).

## 2.5 Compartment Model

Reactors modelled using a conventional compartmental model (CCM) may be comprised of plug flow, mixed flow, and dead flow compartments, and the flow through the reactor may include active, bypass and recycle flow (Levenspiel 1999). In this study, a dispersive compartmental model (DCM) was developed for investigating the mixing performance in the tank. Based on the shape of the measured E-curves (see Fig. 3), the DCM was configured with plug flow and mixed flow compartments in series with the remaining part of the total tank volume assumed to be dead flow. Fig. 6 shows a schematic of the DCM, where the plug flow, mixed flow, and dead flow compartment volumes are defined as  $V_p$ ,  $V_m$  and  $V_d$ , respectively. This schematic diagram is also applicable for a CCM.

Typically, in CCM's the plug flow compartment is assumed to be an ideal PFR and the mixed flow compartment to be a perfect CSTR. The predicted E-curve of PFR follows a Dirac-delta function and the dispersion number is zero (Gutierrez *et al.* 2010), and that of CSTR is an exponential decay curve with a delay due to convection in the PFR. In order to conserve the mass of tracer, the peak of the E-curve is determined by the peak of the CSTR. The E-curve is then defined in two time intervals as shown in the following expression,

$$E_{CCM}(t) = \begin{cases} 0 & , \quad 0 \leq t \leq \frac{V_p}{Q} \\ \frac{Q}{V_m} e^{\left(-\frac{Qt}{V_m} + \frac{V_p}{V_m}\right)} & , \quad \frac{V_p}{Q} < t \leq \infty \end{cases} \quad (2.12)$$

where,  $V_p$  is the volume of the plug flow compartment,  $V_m$  is the volume of mixed flow compartment, and  $Q$  is the flow rate.

The E-curve of the DCM was predicted based on the CCM and the measured E-curves. The measured E-curves increased rapidly but not instantaneously (see Fig. 3) as would be expected for an ideal PFR, indicating that the flow in the plug flow compartment was significantly dispersive. To account for the dispersive nature of this flow, dispersion was introduced into the plug flow compartment by applying the axial dispersion model (ADM) with a modification. Therefore, Eq. (2.9) was assumed to be the governing equation for the flow in the plug flow compartment which leads to the following analytical solution,

$$E(t) = \frac{Q}{V_p \sqrt{\pi N_d}} e^{-\left(\frac{1-tQ/V_p}{2\sqrt{N_d}}\right)^2} \quad (2.13)$$

where,  $N_d$  is the axial dispersion number of the plug flow compartment,  $V_p$  is volume of the plug flow compartment, and  $Q$  is the flow rate. A modification was applied in predicting the peak value of E-curve. In modeling mixed flow

compartment, a solution of perfect CSTR, which is shown in Eq.(2.12), was used in the DCM with a modification.

$$E(t) = \frac{Q}{V_m} e^{\left(-\frac{tQ}{V_m} + \frac{V_p}{V_m}\right)} \quad (2.14)$$

where,  $V_m$  is the volume of the mixed flow compartment and  $Q$  is flow rate.

A modification was applied in order to predict the peak value of E-curves. The peak value in Eq. (2.12) is function of  $Q$ ,  $V_p$  and  $N_d$  and that in Eq. (2.13) is function of  $Q$  and  $V_m$ . But in the DCM, the peak value was assumed to be a function of all variables:  $Q$ ,  $V_p$ ,  $V_m$  and  $N_d$ . Therefore, a coefficient  $b$  was added in Eq. (2.14) by choice to account the all variables for the modification and the modified peak was used in the Eq. (2.13) to formulate a continuous curve. The coefficient indicated the deviation of the performance of the mixed flow compartment from a perfect CSTR. The resulting compartment model predicts E-curves in two separate time intervals as follows,

$$E_{DCM}(t) = \begin{cases} \frac{bQ}{V_m} e^{-\left(\frac{\frac{tQ}{V_p} + 1}{2\sqrt{N_d}}\right)^2}, & 0 \leq t \leq \frac{V_p}{Q} \\ \frac{bQ}{V_m} e^{\left(-\frac{Qt}{V_m} + \frac{V_p}{V_m}\right)}, & \frac{V_p}{Q} < t \leq \infty \end{cases} \quad (2.15)$$

where,  $V_p$  is the volume of the plug flow compartment,  $V_m$  is the volume of mixed flow compartment, and  $N_d$  is the axial dispersion number. In the DCM, the rising limb of the E-curve (i.e.,  $t \leq V_p/Q$ ) is dominated by the ADM and the falling limb (i.e.,  $t > V_p/Q$ ) by the CSTR.

The  $E_{DCM}$  must satisfy the Eq. (2.6) which results in the following expression of  $b$ ,

$$b = \frac{1}{\frac{V_p}{V_m} \sqrt{\pi N_d} \operatorname{erf}\left(\frac{1}{2\sqrt{N_d}}\right) + 1} \quad (2.16)$$

By using the falling limb of the DCM in the Eq. (2.6), it is possible to show that the magnitude of  $b$  indicates the mass under the falling limb of  $E_{DCM}$  and the  $1-b$  must be the mass under the rising limb. Larger mass under the falling limb indicates more positive skewness of E-curves and the performance of the mixed flow compartment is closer to a perfect CSTR. Thus, the value of  $b$  is related to skewness of the E-curves.

It is important to note on the modification of the peak that an alternative coefficient  $b_a$  could be added to Eq. (2.13) instead of adding  $b$  to Eq. (2.14) and used the modified peak in Eq. (2.14) to formulate the DCM continuous. With few algebraic steps, it is possible to show the following relation between  $b_a$  and  $b$ ,

$$b_a = \frac{V_p}{V_m} \sqrt{\pi N_d} b \quad (2.17)$$

The DCM was applied with following other constraints considering the total volume of the tank as  $V$ ,

$$V_m + V_p \leq V \quad (2.18)$$

$$V_p > 0 \quad (2.19)$$

$$V_m > 0 \quad (2.20)$$

$$b \leq 1 \quad (2.21)$$

Low value of  $b$  is determined in such a condition that satisfies a positive skewness of E-curve. Note that the dead flow volume  $V_d$  is given by,

$$V_d = V - V_p - V_m \quad (2.22)$$

Fig. 7 shows the predicted E- and F-curves using the DCM for a reactor with zero  $v_d$  and various  $v_m$  and  $v_p$  with  $N_d$  kept constant at 0.01, where  $v_d$ ,  $v_m$  and  $v_p$  are dead, mixed and plug flow volumes, respectively, in percentage of total volume,  $V$ . The E-curves are delayed more for larger  $v_p$ , because increasing  $v_p$  results in longer convection times. The delay becomes very small when  $v_p$  approaches zero (i.e., 1%) because  $v_m$  approaches the total active flow volume. An extreme end of the DCM is the condition when the total reactor volume is a perfect CSTR (i.e.,  $v_m = 100\%$ ). At this condition, the DCM turns to a CCM. The DCM is applicable to real reactors since these typically have non-zero plug flow and mixed flow volumes. The magnitude of the peak in the E-curve decreases for increasing  $v_m$  because more reactor volume performs as CSTR. Therefore, the lowest peak value is observed at  $v_m = 99\%$  as shown in Fig. 7(a). The predicted F-curves in Fig. 7 have milder slopes for higher mixed flow volumes, because the exponential decay of the concentration is slower for the higher mixed flow volumes. Longer exponential decay also corresponds to positive skewness of E-curve, which results in larger values of  $b$ .

Fig. 8 and Fig. 9 show the predicted E and F-curves for diverse  $v_d$ , keeping  $v_m$  (in Fig. 8) or  $v_p$  (in Fig. 9) constant, and  $N_d$  constant (Fig. 8 and Fig. 9). In Fig. 8,  $v_m$  is held constant at 50% and  $v_d$  varies from 1% to 49% such that  $v_d + v_p = 50\%$ . In Fig. 9,  $v_d$  varies from 5% to 35%,  $v_d + v_m = 50\%$  and  $v_p$  is held constant at 50%. The E-curves in both figures delay because of the increases of  $v_p$  and show higher peak values due to a decrease of  $v_p$  in Fig. 8(a) and an increase of  $v_m$

in Fig. 9(a). The F-curves in Fig. 8(b) do not vary in slopes because of constant  $v_m$ . The F-curves in Fig. 9(b) show milder slope for increasing  $v_m$ , which corresponds to slow exponential decay in E-curves in Fig. 9(a). The effect of dead flow volume is observed by comparing the E-curves in Fig. 7(a) and Fig. 8(a) or Fig. 7(a) and Fig. 9(a). The magnitudes of higher peak value are observed for larger dead flow volumes. Larger dead flow volume associated with low dispersion of the tracer because of small active volume that results in higher peak values.

Finally, Fig. 10 shows the predicted E- and F-curves using the DCM for different  $N_d$  where  $v_m$  and  $v_p$  are kept constant at 50%. The values of  $N_d$  vary from 0.001 to 0.05. The E-curves plotted in Fig. 10(a) show that lower values of  $N_d$  correspond to less dispersion and, therefore, higher peak values. Higher values of  $N_d$  cause the tracer to be more dispersed, the E-curves spread out and the peaks are reduced. The F-curves are plotted in Fig. 10(b) and the effect of increasing  $N_d$  is that the curves rise earlier and their slope is reduced slightly.

The DCM is not applicable to reactors with large plug flow volumes because of the dispersive plug flow. If the mixed flow volume occupies a significant fraction of the active flow volume, the E-curve is skewed to the right (i.e., high positive skewness). As the mixed flow volume is decreased, the E-curve becomes less skewed (i.e., small but positive skewness) and the point where it becomes approximately symmetric is the limit of applicability for the DCM (i.e., skewness approaches to zero). If the mixed flow volume is decreased past this limit or the plug flow volume is above this limit, the E-curve becomes skewed to the left (i.e., negative skewness) and this is physically unrealistic. These limits vary with the dispersion number and for  $N_d$  values of 0.01 and 0.05, while the limits on  $v_p/(v_m+v_p)$  are 84% and 72%, respectively.

A nonlinear optimization method was used to compute the optimal model parameters by minimizing the difference between the modelled and measured E-

curves. The model parameters that were optimized are  $N_D$  for the ADM,  $N_T$  for the TiSM, and  $V_m$ ,  $V_p$ ,  $b$  and  $N_d$  for the DCM. The Levenberg-Marquardt algorithm (LMA) was used to search for the minimum value of the sum of square error ( $SSE$ ) defined as,

$$SSE = \sum_{i=1}^n (E_m(i) - E_e(i))^2 \quad (2.23)$$

where,  $E_m$  is the modelled curve and  $E_e$  is the measured curve. A MATLAB optimization tool (*patternsearch*) was used to compute the minimum SSE, where  $E_m$  was used as an object function. The numerical form of Eq. (2.9) was used as the object function for optimizing  $N_D$ , Eq.(2.11) for optimizing  $N_T$ , Eq(2.12) for optimization CCM parameters ( $V_p$  and  $V_m$  only), and Eq. (2.15) for optimizing the DCM parameters ( $V_p$ ,  $V_m$ ,  $N_d$  and  $b$ ). No constraints were used in the optimization for ADM and TiSM. However, when performing the optimization of the DCM the constraints listed in Eqs.(2.18-2.22) were imposed and Eqs.(2.18 to 2.20 and 2.22) were used as constraints in the CCM.

Fig. 11 and Fig. 12 are two examples of comparison between modelled and experimental E curves for small and large mixed flow compartments. For a better visualization in the plot, the measured E-curve data are plotted at 4 Hz, whereas all data were used for the optimization. The plots show that the E-curves predicted by the DCM were better fits to the experimental E-curves than the curves predicted using the ADM, TiSM and CCM. The root mean square error (RMSE) between the modelled and experimental data was computed and the values of RMSE were 0.0071, 0.0132, 0.0074 and 0.0036 for the ADM, TiSM, CCM and DCM, respectively (Fig. 11). In Fig. 12, RMSE were 0.0100, 0.0056, 0.0061 and 0.0033 for the ADM, TiSM, CCM and DCM, respectively. The average values of the RMSE were 0.0109, 0.0104, 0.0074, 0.0046 for the ADM, TiSM, CCM and DCM, respectively. These estimates of RMSE clearly show that the DCM performs significantly better than the other three models.

The reason of having a good match of the DCM and experimental E-curves is that the DCM modelled the critical and characteristic part of the experimental E-curve. The critical and characteristic part was the peak value, and the slope of the limb to the peak and that of the falling limb from the peak. These parts were better matched by the DCM than those predicted by the other three models. However, the tail part of experimental E-curves was poorly matched with the DCM when there was a significant volume as a dead flow as shown in Fig. 11. The DCM matched the tail part of the experimental E-curves very well in case of the low dead flow volume as displayed in Fig. 12.

## **2.6 Results**

Three pairs of measured E-curves are shown in Fig. 13 to Fig. 15 to explain the effects of layout and Reynolds number. The effects of jet-positions on the layouts are shown in Fig. 13, where jets are opposing to each other and close to inlets/outlets in layout C, and jets are staggered and away from inlets/outlets in layout H. Both E-curves showed that the tank is not a perfect CSTR as the peaks are observed at delayed time. The delays are almost the same for both layouts. The peaks were observed at 6.0 sec for layout C and at 7.6 sec for layout H. The characteristics of plug flow in both cases are similar. However, the characteristics can be quantified later by applying hydraulic indices and model parameters. The figure clearly shows that the peak value of the E-curve is significantly higher and the falling limb of the E-curve is steeper for layout C than those in layout H. The high peak value and steep falling limb for layout C indicate that high-concentrated inlet tracer was not mixed very well inside the tank. The low peak for layout H indicates well mix of the inlet tracer in the tank. The peaks of two E-Curves in Fig. 14 are also delayed almost by same time. The effects of jet numbers are not observed in the plug flow characteristics. However, the slopes of the falling limbs are not significantly different in large part of the falling limbs, even though the magnitude of the peak for 12 jets is higher than that for 4 jets. The peak values indicated that more number of jets is not necessary to increase the mixing

characteristics of the flow. The effect of Reynolds number is shown in the plots of two E-curves in Fig. 15. These plots clearly show less mixing flow characteristics for low Reynolds number and more mixed flow for increased Reynolds number.

In Fig. 16 and Fig. 17, the hydraulic indices,  $\overline{\theta}_t$ ,  $\overline{\theta}_p$ ,  $\overline{\theta}_{10}$ ,  $\overline{\theta}_g$ ,  $\overline{\theta}_{50}$  and  $\overline{\theta}_{90}$  are plotted for different  $A$ ,  $Re$  and  $d$  values. Note that the over bar indicates the mean value of 14 to 18 repeated measurements used to compute the plotted indices. The standard error of the mean varied from 0.4% to 3.6%, indicating that the measurements were very repeatable. It is evident from Fig. 16 that the mean values of the three hydraulic indices  $\overline{\theta}_t$ ,  $\overline{\theta}_p$  and  $\overline{\theta}_{10}$ , did not vary significantly with  $A$ ,  $Re$  and  $d$ . The maximum variation, measured by standard error of the mean, was 0.5%. The plots of  $\overline{\theta}_g$ ,  $\overline{\theta}_{50}$  and  $\overline{\theta}_{90}$  in Fig. 17 show that these indices vary significantly with  $A$ ,  $Re$  and  $d$ , but they are close in magnitude to the standard values of a perfect CSTR (see Table 2.3). The difference between the computed indices and the CSTR values varied from 0.6% to 17.0%, indicating that the flow in the mixing tank was similar to a CSTR. The values of all six indices indicate that the mixing occurring in the tank was closer to a CSTR than to a PFR.

The TiSM was used to compute the values of  $N_T$  for each repeated run of all 23 experiments. The value of  $N_T$  was 2 for 91.4%, 1 for 1.3%, and 3 for 7.3% of the experimental runs. The average value of  $N_T$  was 2.06 with a margin of error of  $\pm 0.01$  at a confidence level of 95%. These results clearly indicated that the TiSM model predicting the mixing performance of the tank was very close to a CSTR, and that the experimental factors had no significant effects on  $N_T$ .

The ADM was applied to each repeated run of all 23 experiments to determine the effects of  $A$ ,  $Re$  and  $d$  on the dispersion number  $N_D$ . The mean value of  $N_D$  defined as  $\overline{N}_D$  computed for each experiment is plotted in Fig. 18 for different  $A$ ,  $Re$  and  $d$ . The values of  $\overline{N}_D$  varied within a very narrow range, from 0.24 to 0.38 for different layouts  $A$  and from 0.24 to 0.42 for varying  $Re$  and  $d$ . ANOVA

(analysis of variance) was performed and it was found that less than 12% of test-pairs were significantly different. Therefore, it was concluded that  $N_D$  did not vary significantly with  $A$ ,  $Re$  or  $d$ . The average value of  $\overline{N_D}$  computed over all tests was 0.33 which indicates that the flow in the tank was highly dispersed or that the mixed flow volume occupies a high percentage of the tank (Levenspiel 2012).

In Figs. 19, the values of  $\overline{N_d}$  predicted by the DCM for the plug flow compartment are plotted for different  $A$ ,  $Re$  and  $d$ . For different layouts, the value of  $\overline{N_d}$ , varied from 0.013 to 0.025 with a mean value of 0.016 as shown in Fig. 19(a). This variation was considered within a very small range. However, there were no significant variations of  $\overline{N_d}$  for different  $Re$  and  $d$  as shown in Fig. 19(b). All values of  $\overline{N_d}$  indicated that the dispersion number of the plug flow compartment was low compared to the dispersion number of a PFR with high  $Re$  ( $\sim 10^4$ ) (Hart *et al.* 2013).

The values of  $b$ , predicted by the DCM are plotted in Fig. 20 for varying  $A$ ,  $Re$  and  $d$ . The largest  $b$  in the plot of Fig. 20(a) is 0.80 for the layouts B and G. This indicates high mixed flow volumes for the layout B and G. Fig. 20(b) shows that the values of  $b$  are not significantly different from 0.80 at Reynolds number from 21400 and 27300, where the values varied from 0.74 to 0.81. The lowest  $b$  is 0.67 in Fig. 20(b) at  $Re$  of 10500 and  $d$  of 5.3 mm for layout B. The lowest  $b$  indicated the lowest mixed flow volume.

The estimates of  $v_m$ ,  $v_p$  and  $v_d$  made using the DCM for different  $A$  are plotted in Fig. 21 for  $Re = 21,400$  and  $d = 5.3$  mm. The DCM predicted that  $v_p$  did not vary significantly, but both  $v_m$  and  $v_d$  varied significantly as the layout was changed. The average value of the plug flow volume  $v_p$  was  $29.0 \pm 0.012\%$  estimated within 95% confidence limits. The mixed flow volume  $v_m$  varied from 42.9% to 67.9% and the dead flow volume  $v_d$  varied from 1.5% to 31.5%. The wide ranges in the predicted values of  $v_m$  and  $v_d$  indicate that varying the jet layout has a significant effect on the mixing in the tank. Layouts B and H had the largest values of  $v_m$  of

67.9% and 67.6%, respectively, indicating that these two layouts produced the most effective mixing in the tank.

The effect of varying  $Re$  and  $d$  on  $v_m$ ,  $v_p$  and  $v_d$  was investigated for layouts  $B$  and  $H$ . Fig. 22 shows  $v_p$  as a function of  $Re$  for two values of  $d$ . It is evident that  $v_p$  did not vary with neither with  $Re$  nor with  $d$ . The mean value of  $v_p$  in this figure was 27.9%, which is not significantly different from the mean of  $v_p$  for different layouts shown in Fig. 21. Fig. 23 presents  $v_m$  versus  $Re$  for two values of  $d$ .  $v_m$  is approximately 44% for  $Re \leq 5000$  and then increases to approximately 67.9% at  $Re = 27,400$ . Large values of  $v_m$ , (i.e.,  $\geq 65.3\%$ ) were observed at  $Re = 21400$  and  $27000$  for 5.3 mm diameter jets. The 3.8 mm diameter jets produced  $v_m = 67.7\%$  only at  $Re = 27,400$ . However, the maximum value of  $v_m$  was 67.9%, obtained at  $Re$  of 20700 with 5.3 mm jets and layout B. In Fig. 24  $v_d$  is plotted as a function of  $Re$  for two values of  $d$ . It can be seen that  $v_d$  values were relatively high (i.e.,  $\sim 32\%$ ) at low  $Re$  and decreased with increasing  $Re$ . The lowest values of  $v_d$  ( $\sim 1.5\%$ ) were observed at the highest  $Re$ . The results in Fig. 23 and Fig. 24 show the effect of varying  $d$  varied with  $Re$ . At  $Re = 5200$  and  $10500$ ,  $v_m$  was predicted to be significantly greater for  $d = 3.8$  mm compared to that at 5.3 mm. At  $Re = 21400$ ,  $v_m$  was predicted to be significantly greater for larger diameter jets and at  $Re = 27300$ . The two jet diameters were predicted to have approximately equal  $v_m$ .

## 2.7 Conclusion

The goal of the study was to determine the jet-configuration and operational condition of transverse jets for the removal of FOG from grit where the first step was to develop high mixed flow volume by the jets. The best jet-configuration and operational condition was the layouts B or H with Reynolds numbers of 21400 and 27300 for 5.3 mm jets or with Reynolds number 27300 for 3.8 jets. Their conditions allowed setting the general guidelines for designing a reactor as a CSTR or close to a CSTR. Jets were penetrated to locations where ambient velocities were low. The locations were away from inlets and outlets. According

to jet theories, more of this momentum ratio causes more mixing in the flow (Rajaratnam 1976). Based on the results of two jet diameters, larger diameter of jets were better in producing more mixed flow volume. Larger diameter of jets causes larger expansion of jets, resulting in more mixed flow volume because of more agitation of ambient fluid. It was concluded from the results of layouts C to H that larger ambient fluid was agitated when jets from opposite walls were placed with an offset distance. The two opposite jets with the offset distance caused the development of local eddies that increased the mixing of fluids. For an effective and economic design, layout B with a Reynolds number of 21000 and 5.3 jets was chosen because this configuration and operating condition required minimum jet flow rate and minimum input energy.

The values of  $N_D$  computed by ADM were close to the values of  $N_D$  in highly dispersive pipe flows with Reynolds number of  $10^4$  to  $10^5$  (Hart et al. 2013) which is not surprising because Reynolds number of the mainstream flow was 21,400. Therefore, the mainstream flow had a stronger influence on  $N_D$  than the transverse jets because the jets contributed mostly to radial dispersion. The values of  $N_D$  were thus obtained within a narrow range. The strong dispersive mainstream flow also contributed mostly on  $N_T$ , which was estimated by TiSM. Transverse jets had insignificant contribution on  $N_T$  as well. Therefore, the effects of  $A$ ,  $Re$ , and  $d$  were not observed on the values of  $N_D$  or  $N_T$ .

The effects of  $A$ ,  $Re$ , and  $d$  were strongly observed on the model parameters of the DCM. The DCM estimated constant plug flow volume and varying mixed flow volumes for varying  $A$ ,  $Re$ , and  $d$ . The plug flow volume was constant because the mainstream flow, which was unchanged, mostly contributed to this volume. The remaining part of the tank volume was influenced by the transverse jets; therefore, mixed flow volumes varied because of varying jet-parameters ( $A$ ,  $Re$ , and  $d$ ).

The DCM was the best model among the four models discussed in this study because the RMSE of the DCM was significantly lower than that of the other

models. The RMSE of CCM was closest to that of the DCM. The DCM was more advantageous than the CCM because the DCM estimated the dispersive nature of the plug flow compartment. This model can be used for almost all real reactors where the E-curve shows a single peak. The DCM modelled the E-curves in two time intervals separated by the peak time. However, the DCM can be modified for the E-curves with multiple peaks by defining the equations of E-curves for more than two time intervals.

## References

Anderson, R., and Holmberg, M. (2006). "Energy Conservation in Wastewater Treatment Operation." Lund University, Sweden: Master Thesis.

Brenner, A., and Diskin, M. H. (1991). "Model study of jet-circulated grit chamber." *J. Environ. Eng.*, 117(6), 782-787.

Chisti, Y. (2001). "Hydrodynamic damage to animal cells." *Crit. Rev. Biotechnol.*, 21(2), 67.

Dueck, J., Pikushchak, E., and Minkov, L. (2009). "Modelling of change of the classifier separation characteristics by water injection into the apparatus." *Thermophysics and Aeromechanics*, 16(2), 247-258.

Gang, D. D., Rakesh, B., and Shankha, B. (2010). "Wastewater: Treatment Processes." *Encyclopedia of Agricultural, Food, and Biological Engineering, Second Edition*, 1(1), 1825-1836.

Gravette, B., Strehler, A., Finger, D., and Palepu, S. (2000). "Troubleshooting a Grit Removal System." *Proceedings of the Water Environment Federation*, 2000(11), 332-369.

Gutierrez, C. G., Dias, E. F., and Gut, J. A. (2010). "Residence time distribution in holding tubes using generalized convection model and numerical convolution for non-ideal tracer detection." *J.Food Eng.*, 98(2), 248-256.

Habib, A. (2008). "Investigating the performance of an aerated grit chamber." *M.Sc. thesis*, University of Alberta (Canada), Canada.

Hart, J., Guymer, I., Jones, A., and Stovin, V. (2013). "Longitudinal Dispersion Coefficients within Turbulent and Transitional Pipe Flow." *Experimental and Computational Solutions of Hydraulic Problems*, Springer, 133-145.

Hay, T. T. (1946). "Experience in Grit Removal and Handling at Racine, Wis." *Sewage Works Journal*, 18(1), 54-65.

Levenspiel, O. (2012). *Tracer Technology: Modeling the Flow of Fluids*. Springer.

Levenspiel, Octave. "Chemical reaction engineering." *Industrial & engineering chemistry research* 38.11 (1999): 4140-4143.

Libralato, G., Losso, C., Arizzi, N. A., Citron, M., Della, S., Stefano, Zanutto, E., Cepak, F., and Volpi Ghirardini, A. (2008). "Ecotoxicological evaluation of industrial port of Venice (Italy) sediment samples after a decontamination treatment." *Environmental Pollution*, 156(3), 644-650.

Liem, L., Stanley, S., and Smith, D. W. (1999). "Residence time distribution analysis as related to the effective contact time." *Canadian Journal of Civil Engineering*, 26(2), 135-144.

MacLoughlin, P. F., Malone, M., Murtagh, J. T., and Kieran, P. M. (2000). "The effects of turbulent jet flows on plant cell suspension cultures." *Biotechnology and Bioengineering*, 58(6), 595-604.

Matvienko, O., and Evtyushkin, E. (2007). "Theoretical investigation of the process of cleaning oil-polluted soil in hydrocyclone apparatuses." *Journal of Engineering Physics and Thermophysics*, 80(3), 502-510.

Morales, L., and Reinhart, D. (1984). "Full-Scale Evaluation of Aerated Grit Chambers." *WPCF J*, 56(4), 337.

Philipossian, A., and Mitchell, E. (2003). "Dispersion number studies in CMP of interlayer dielectric films." *J.Electrochem.Soc.*, 150 G854.

Rajaratnam, N. (1976). *Turbulent jets*. Elsevier Science Limited.

Tchobanoglous, G., Burton, F., and Stensel, H. D. (2003). *Wastewater Engineering: Treatment and Reuse*. McGraw Hill, NY.

Thirumurthi, D. (1969). "A break-through in the tracer studies of sedimentation tanks." *Journal Water Pollution Control Federation*, 41(11), 405-418.

Wahl, M. D., Brown, L. C., Soboyejo, A. O., and Dong, B. (2012). "Quantifying the hydraulic performance of treatment wetlands using reliability functions." *Ecol. Eng.*, 47(0), 120-125.

Yuan, Y., and Farnood, R. R. (2010). "Strength and breakage of activated sludge flocs." *Powder Technol.*, 199(2), 111-119.

## Tables

Table 2.1: Layouts (*A*) of transverse jets showing the position and number of jets by circles and crosses. Circles and crosses denote jets that are located on the near and far side walls, respectively. Arrows indicate direction of the mainstream flow.

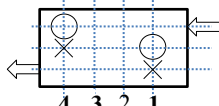
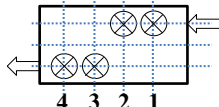
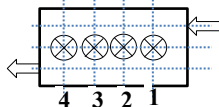
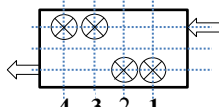
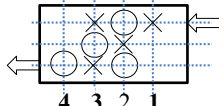
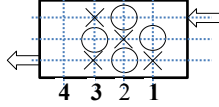
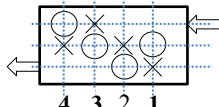
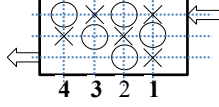
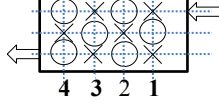
<i>A</i>	Layout
A	 <p style="text-align: center;">4 3 2 1</p>
B	 <p style="text-align: center;">4 3 2 1</p>
C	 <p style="text-align: center;">4 3 2 1</p>
D	 <p style="text-align: center;">4 3 2 1</p>
E	 <p style="text-align: center;">4 3 2 1</p>
F	 <p style="text-align: center;">4 3 2 1</p>
G	 <p style="text-align: center;">4 3 2 1</p>
H	 <p style="text-align: center;">4 3 2 1</p>
I	 <p style="text-align: center;">4 3 2 1</p>
J	 <p style="text-align: center;">4 3 2 1</p>

Table 2.2: Layout ( $A$ ), Reynolds number ( $Re$ ) and jet diameter ( $d$ ) for all experiments.

Experiment No.	$A$	$Re$	$d$ (mm)
1	A	0	5.3
2	B	20700	5.3
3	C	21500	5.3
4	D	21500	5.3
5	E	21100	5.3
6	F	21600	5.3
7	G	21700	5.3
8	H	21600	5.3
9	I	21400	5.3
10	J	21400	5.3
11	B	5200	5.3
12	B	10600	5.3
13	B	16300	5.3
14	B	27000	5.3
15	H	16400	5.3
16	H	26800	5.3
17	H	5100	3.8
18	H	10400	3.8
19	H	21600	3.8
20	H	27000	3.8
21	B	10300	3.8
22	B	22000	3.8
23	B	27300	3.8

Table 2.3: Hydraulic indices of an ideal PFR and perfect CSTR.

Hydraulic Indices	Ideal PFR	Perfect CSTR
$\theta_i$	1	0.01
$\theta_{10}$	1	0.11
$\theta_p$	1	0
$\theta_{50}$	1	0.69
$\theta_g$	1	1
$\theta_{90}$	1	2.30

**Figures**

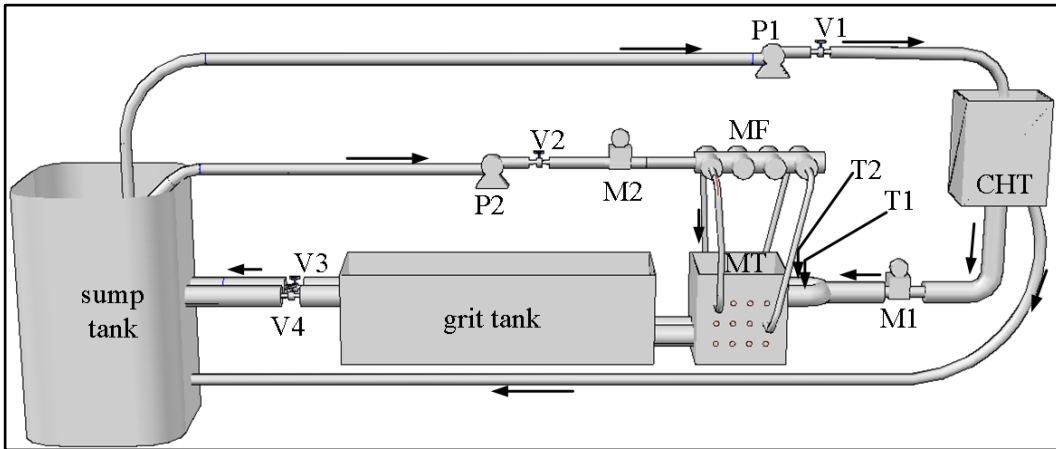


Fig. 1: Experimental setup for RTD measurements [MT: mixing tank, CHT: constant head tank, P1 and P2: centrifugal pumps; M1 and M2: magnetic flow meters; T1 and T2: tracer injection ports; V1, V2 and V3: globe valves].

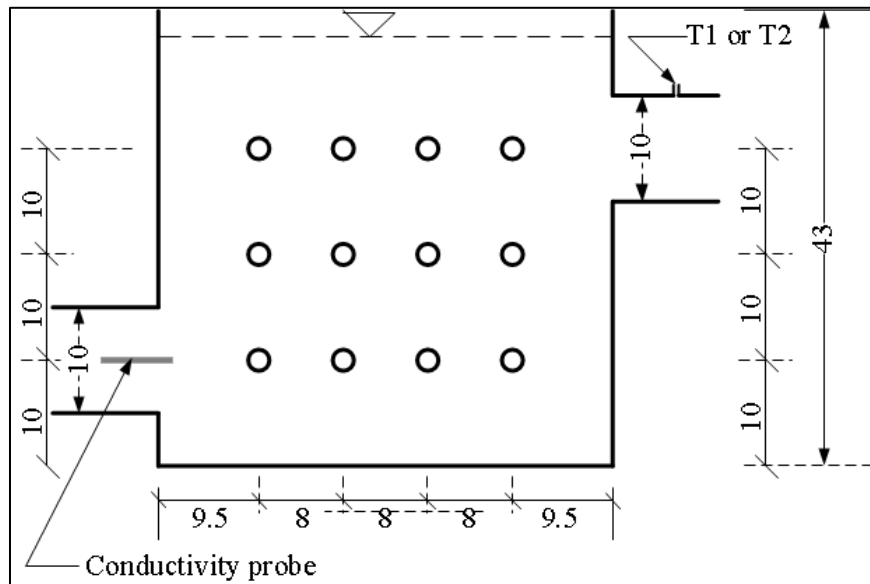


Fig. 2: Side view of the mixing chamber showing transverse jet position in circles [all dimensions are in cm].

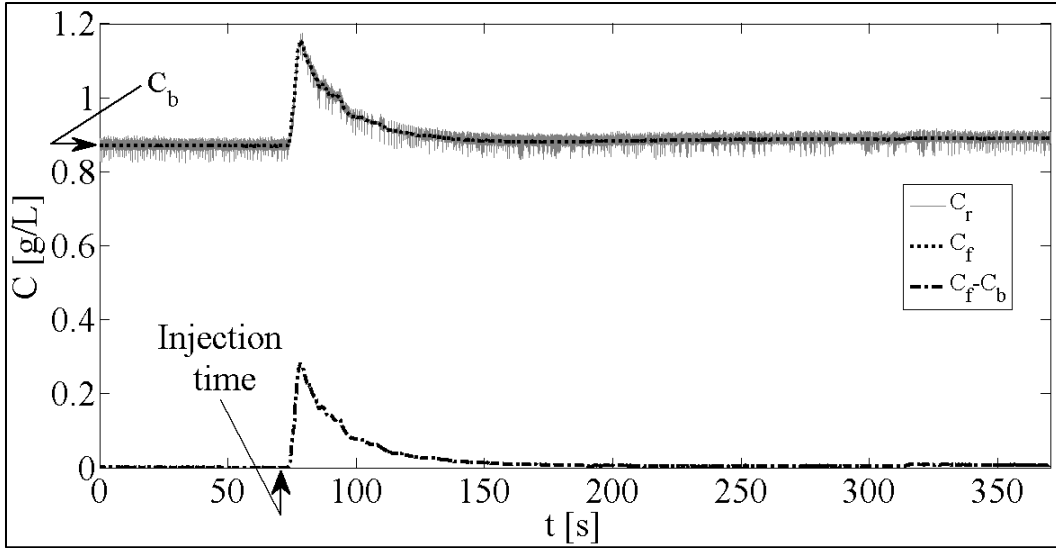


Fig. 3: Time series of raw, filtered and background corrected concentration for a single RTD measurement [ $\Lambda = H$ ,  $Re = 21600$ ,  $d = 5.3$  mm, run number 07],  $C_r$ : raw concentration,  $C_f$ : filtered concentration, and  $C_f - C_b = C$ , injection time is 69.6s.

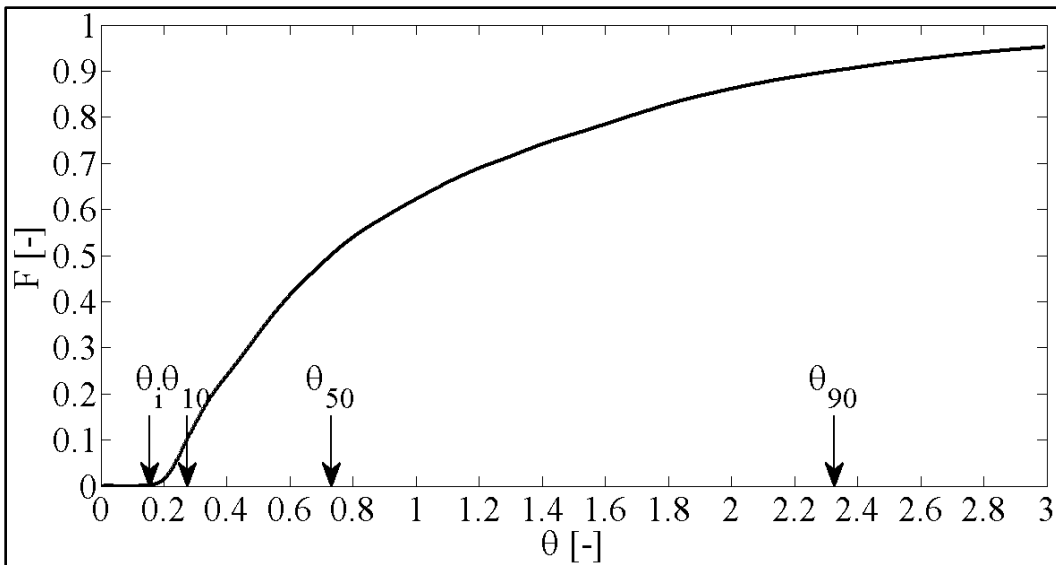


Fig. 4: Cumulative exit age curve or F-curve for an experimental run with  $\Lambda = H$ ,  $d = 5.3$  mm and  $Re = 21603$ .  $\theta$  is defined as dimensionless time, and  $\theta_i$ ,  $\theta_{10}$ ,  $\theta_{50}$  and  $\theta_{90}$  are the dimensionless times when 1% , 10%, 50% and 90% of tracer is recovered.

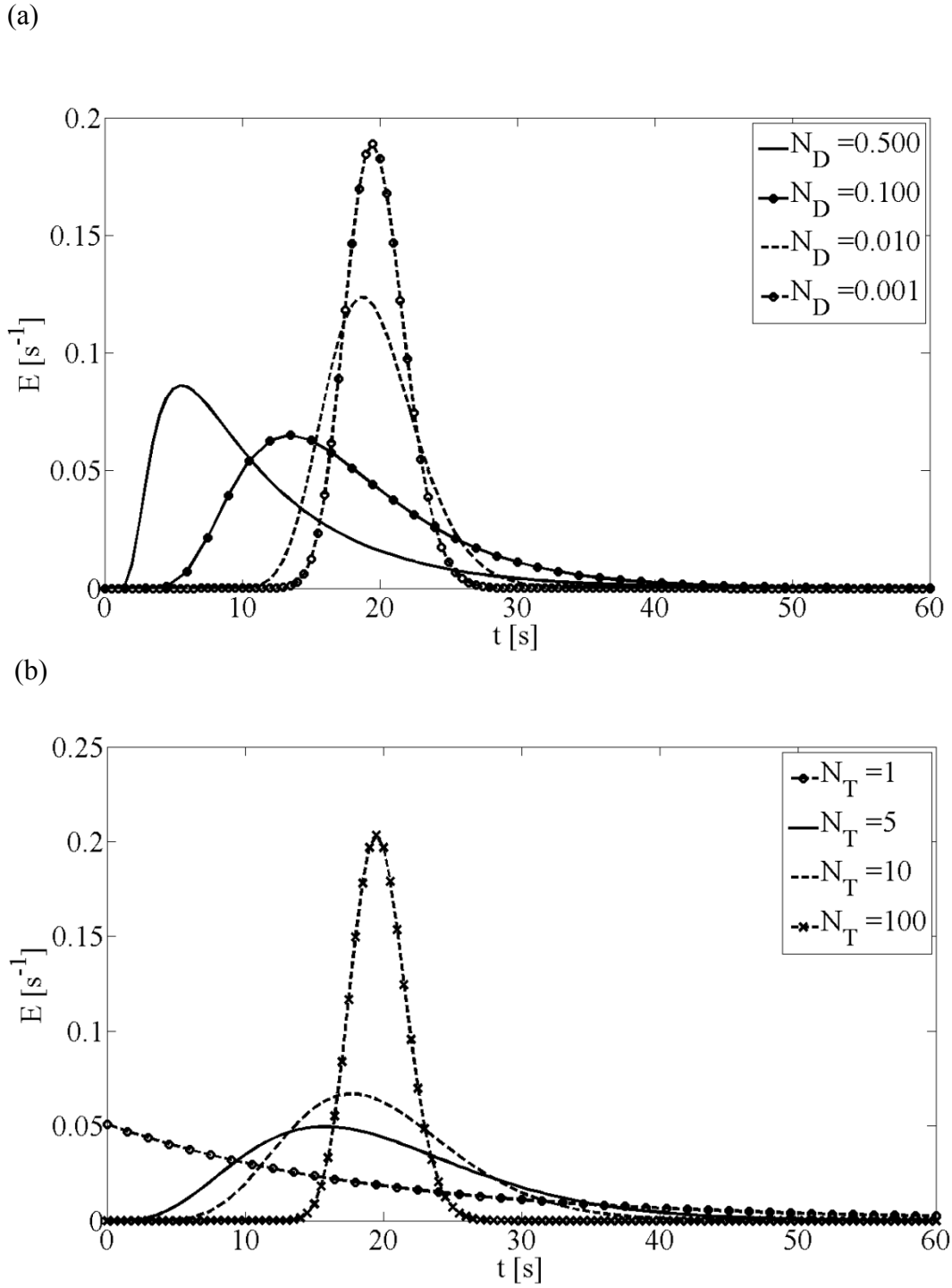


Fig. 5: E-curves predicted using the (a) Axial Dispersion Model for different dispersion numbers,  $N_D$  and (b) Tank in Series Model for different equivalent tank numbers,  $N_T$ . Plots are based on mean residence time  $\tau = 19.7$  s.

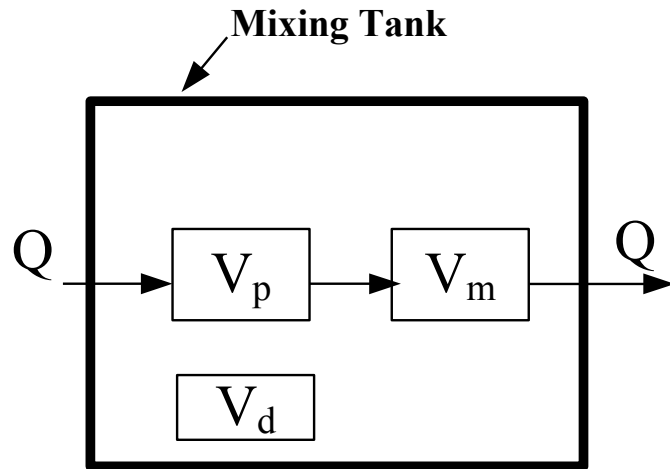


Fig. 6: Schematic diagram of the Dispersive Compartmental Model showing the plug, mixing and dead flow compartments:  $V_p$  is the plug flow volume,  $V_m$  is the mixed flow volume, and  $V_d$  is the dead flow volume of a mixing tank;  $Q$  = mainstream flow rate.

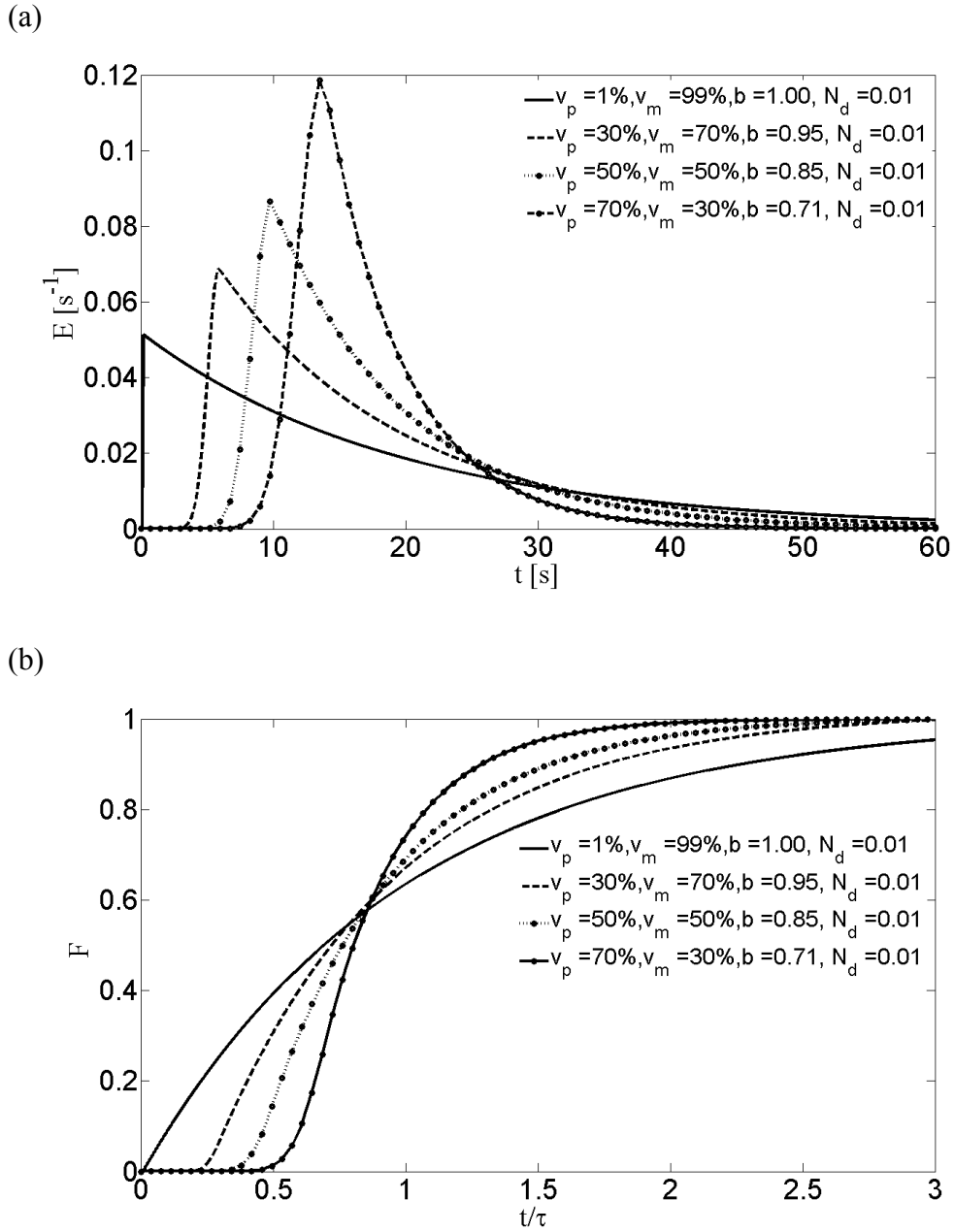


Fig. 7: (a) E-curves and (b) F-curves predicted using the Dispersive Compartmental Model for various  $v_p$  and  $v_m$ , where  $N_d = 0.01$ ,  $v_d = 0$  and  $\tau = 19.7$  s. [here  $b$  varies for varying  $v_p/v_m$ ].

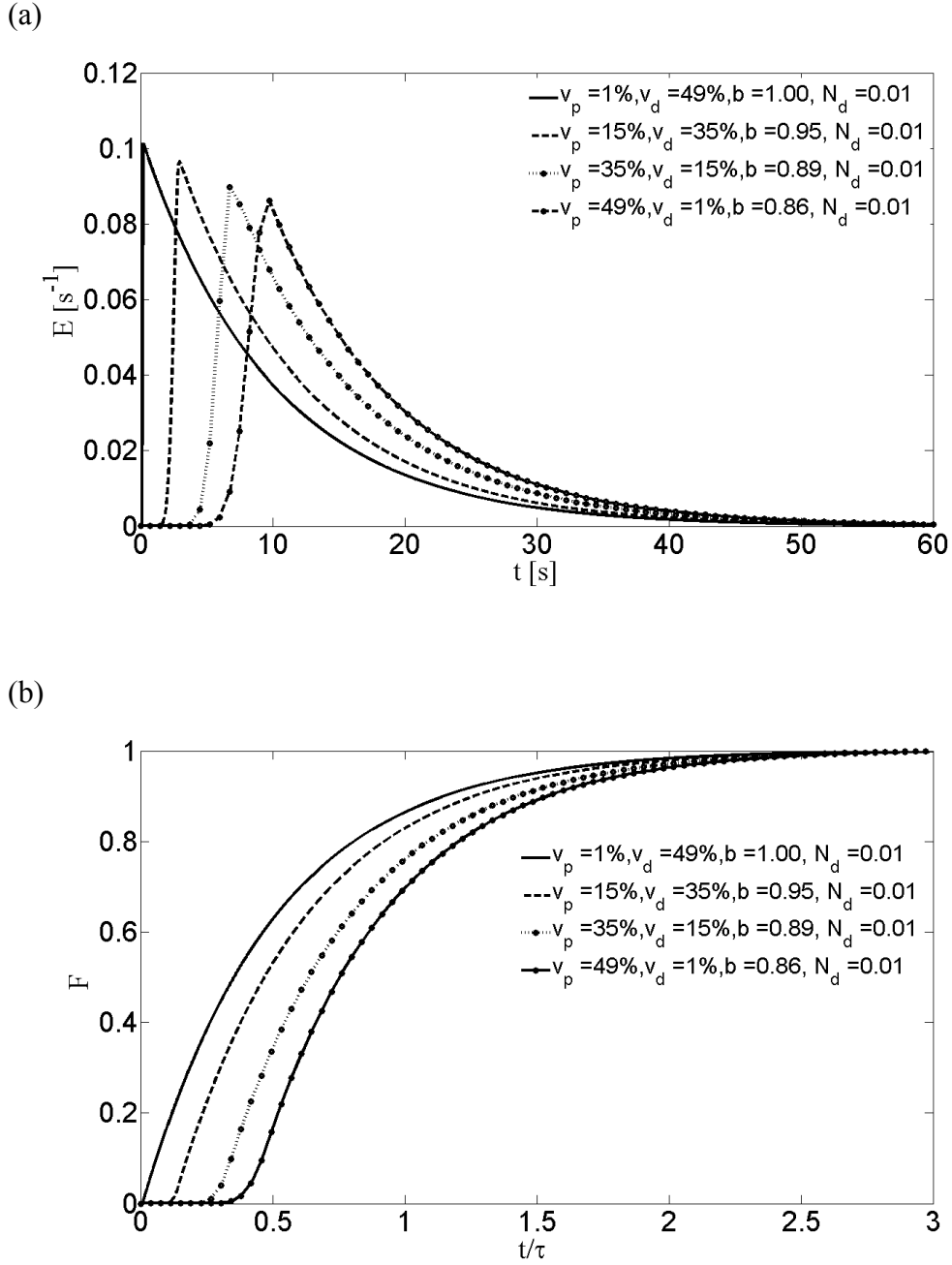


Fig. 8: (a) E-curves and (b) F-curves predicted using the Dispersive Compartmental Model for arbitrary  $v_p$  and  $v_d$ , where  $v_m = 50\%$  and  $N_d = 0.01$  and  $\tau = 19.7$  s. [ here  $b$  varies for varying  $v_p/v_m$ ].

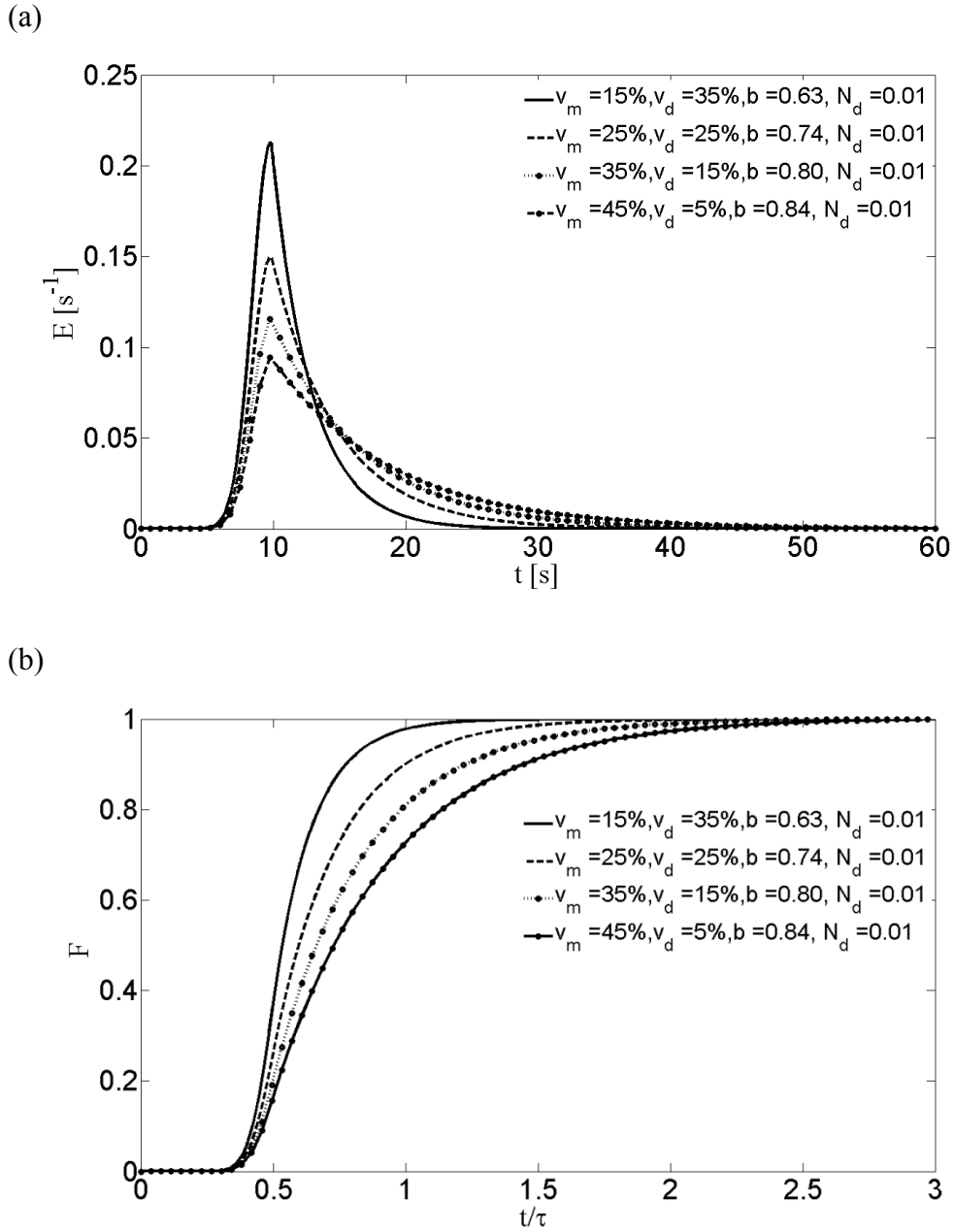


Fig. 9: (a) E-curves and (b) F-curves predicted using the Dispersive Compartmental Model for various  $v_m$  and  $v_d$ , where  $v_p = 50\%$  and  $N_d = 0.01$  and  $\tau = 19.7$  s. [here  $b$  varies for varying  $v_p/v_m$ ].

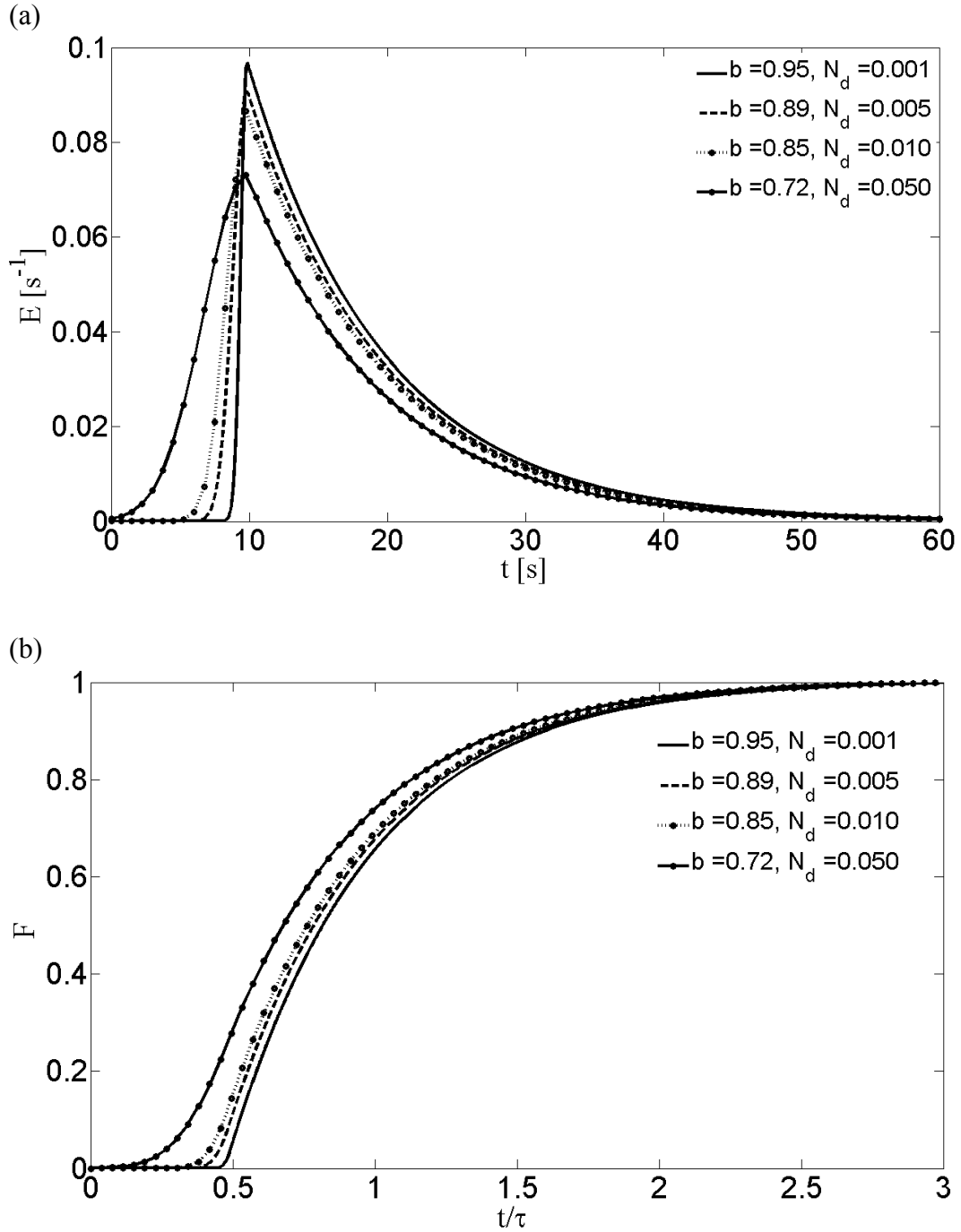


Fig. 10: (a) E-curves and (b) F-curves predicted using the Dispersive Compartmental Model for various  $N_d$  and for constant value of  $v_m = v_p = 50\%$  and  $\tau = 19.7$  s. [here  $b$  varies for varying  $N_d$ ].

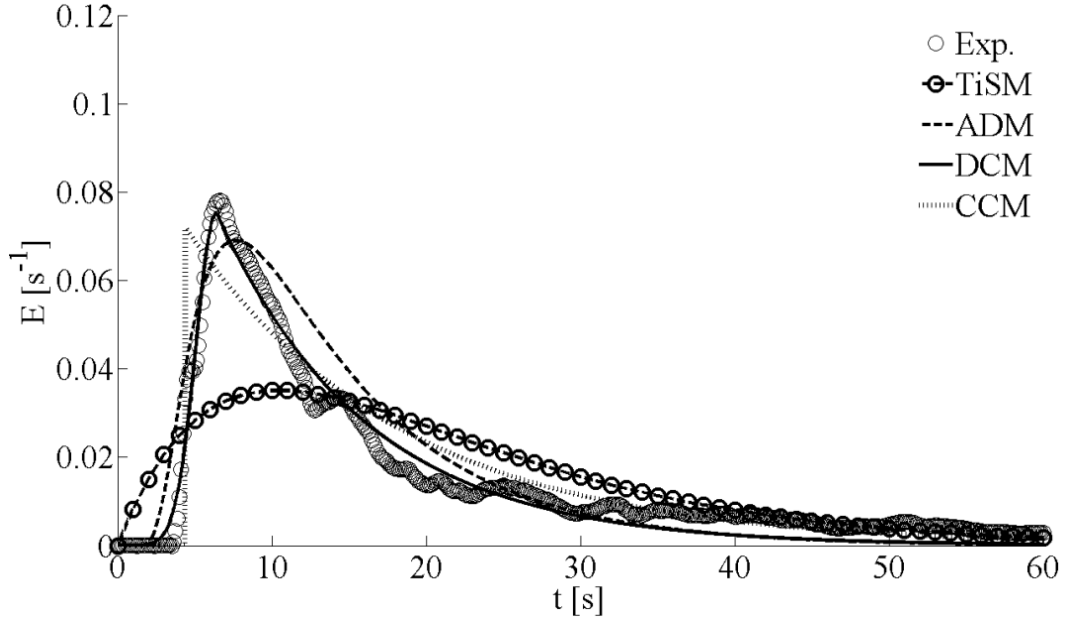


Fig. 11: Four model predicted E-curves are compared with the experimental E-curve of a test with a low mixed flow volume [ $A = H$ ,  $d = 3.8$  mm,  $Re = 5147$ ; Model parameters are:  $N_D$  of ADM is 0.34,  $N_T$  of TiSM is 2,  $v_p$  and  $v_m$  of CCM are 23%, 65% respectively and  $v_p$ ,  $v_m$ ,  $N_d$  and  $b$  of DCM are 30.3% , 45.8%, 0.02, 0.73 respectively].

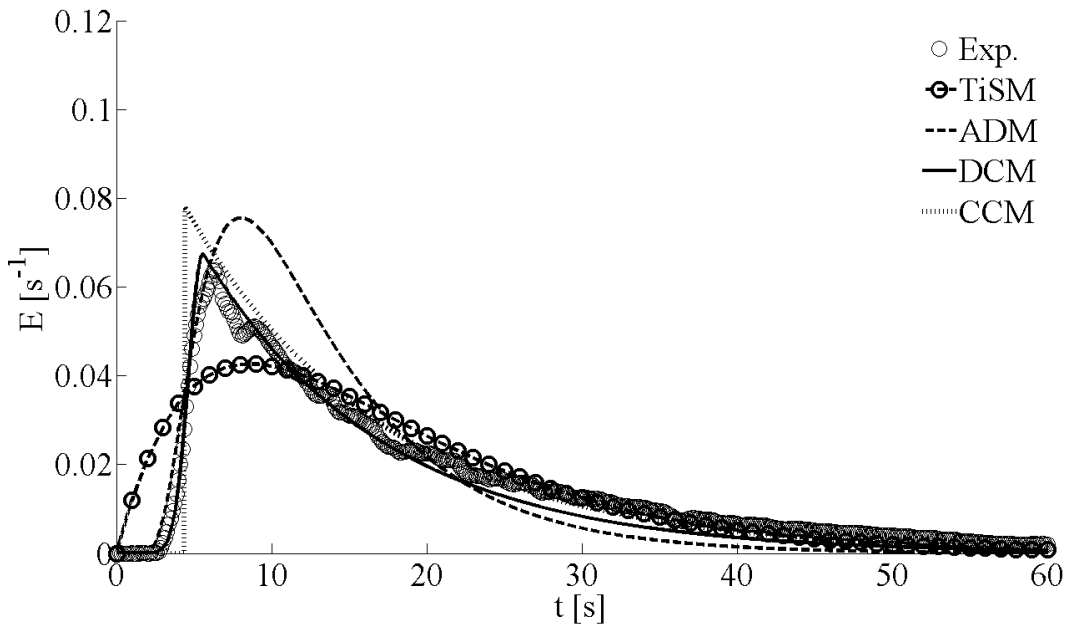


Fig. 12: : Four model predicted E-curves are compared with the experimental E-curve of a test with a high mixed flow volume [ $A = H$ ,  $d = 5.3$  mm,  $Re = 26840$ ; Model parameters are:  $N_D$  of ADM is 0.24,  $N_T$  of TiSM is 2,  $v_p$  and  $v_m$  of CCM are 25.3%, 73.5% respectively and  $v_p$ ,  $v_m$ ,  $N_d$  and  $b$  of DCM are 31.9.3% , 66.8%, 0.013, 0.79 respectively].

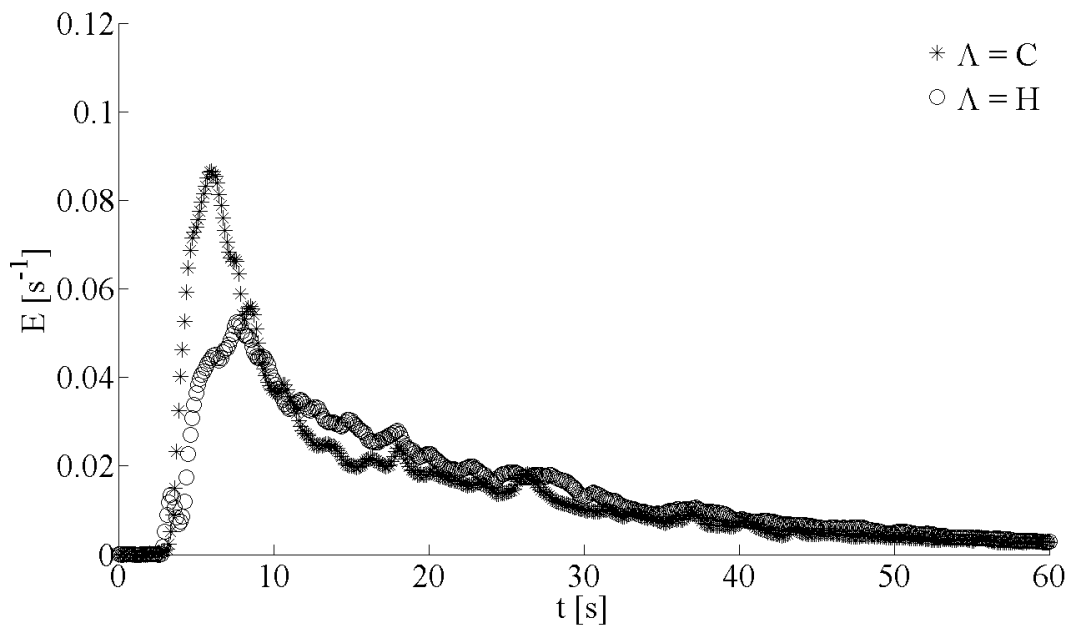


Fig. 13: Experimental E-curves for two  $\Lambda$  with similar  $Re$ , where  $Re = 21400$  for  $\Lambda = C$  and  $Re = 21600$  for  $\Lambda = H$ , and  $d = 5.3$  mm for both tests.

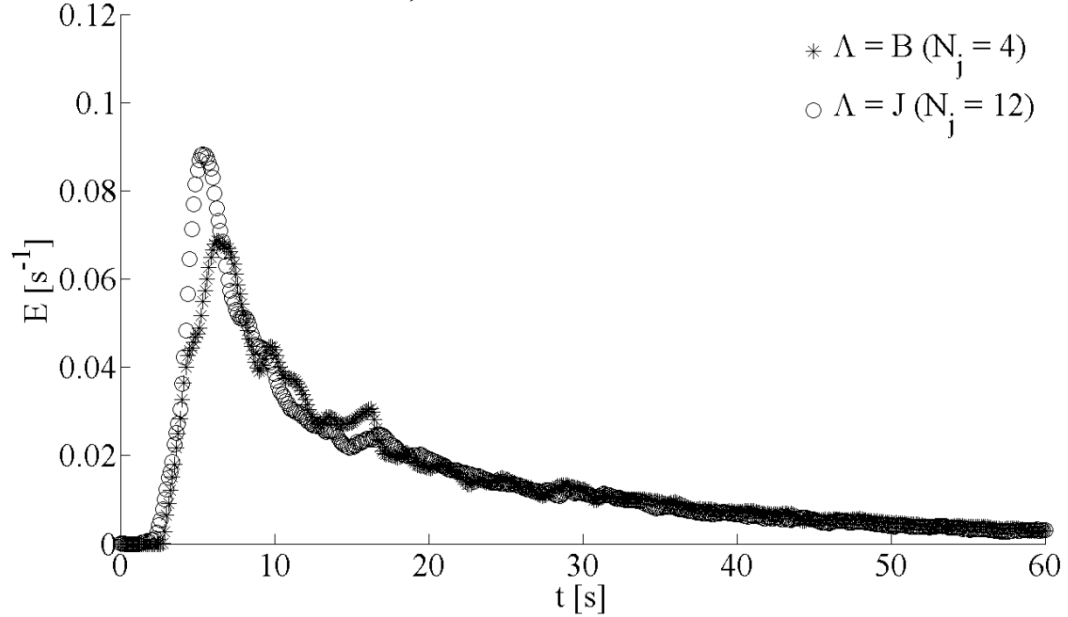


Fig. 14: Experimental E-curves for two different number of jets ( $N_j$ ) with similar  $Re$ , where  $Re = 20700$  for  $\Lambda = B$  and  $Re = 21400$  for  $\Lambda = J$ , and  $d = 5.3$  mm for both tests.

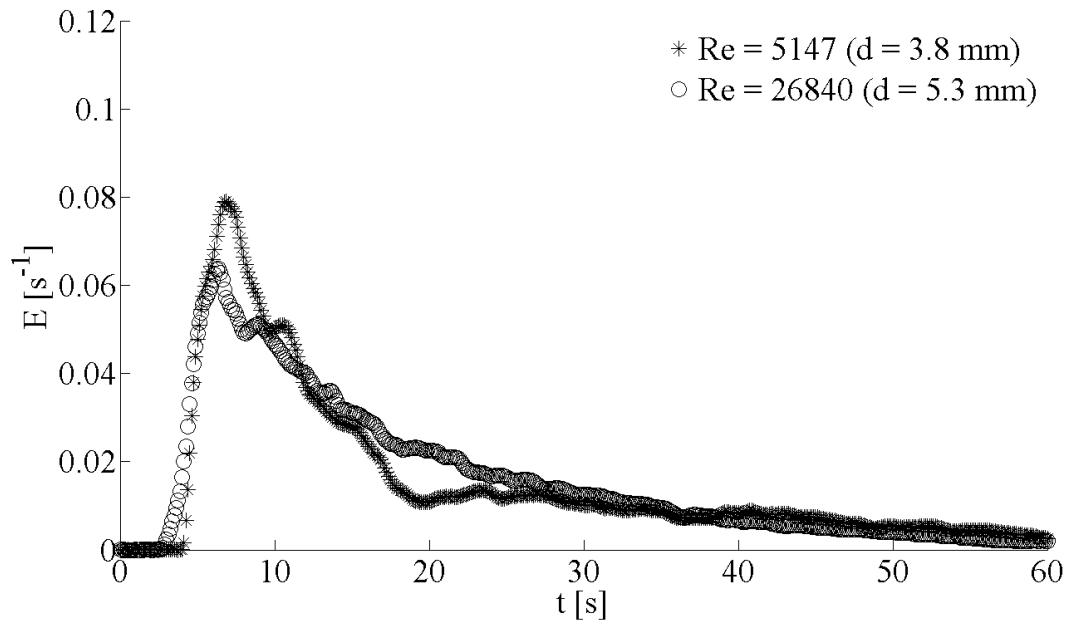


Fig. 15: Experimental E-curves for two different  $Re$  with same layout  $A$ , where  $A = H$

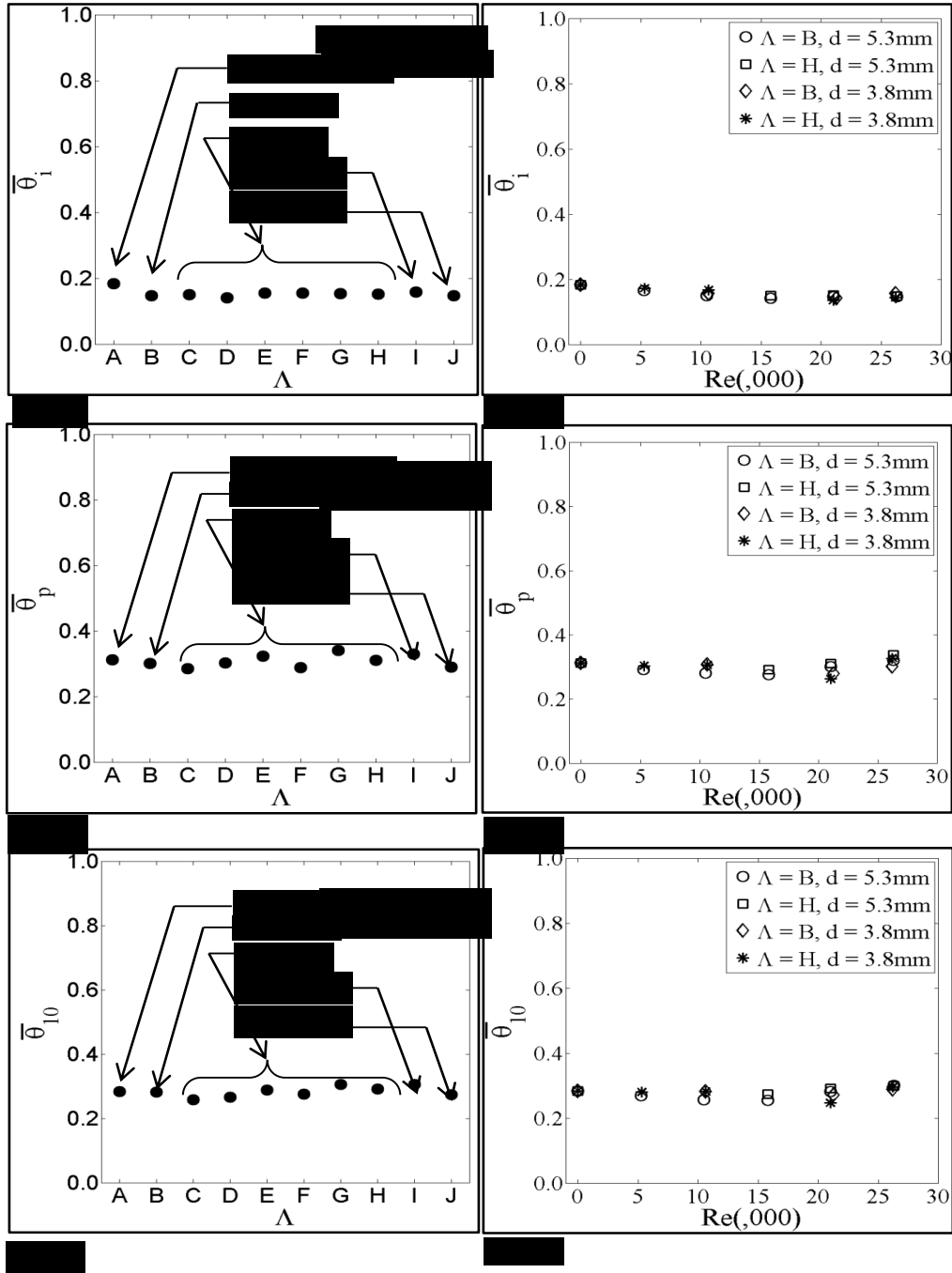


Fig. 16: Plots of hydraulic indices  $\bar{\theta}_i$ ,  $\bar{\theta}_p$  and  $\bar{\theta}_{10}$  versus layout,  $\Lambda$  in (a) to (c) and versus Reynolds number,  $Re$  in (d) to (f).  $\bar{\theta}_i$  = mean dimensionless arrival time,  $\bar{\theta}_p$  = mean dimensionless time to peak and  $\bar{\theta}_{10}$  = mean dimensionless time to capture 10% tracer.

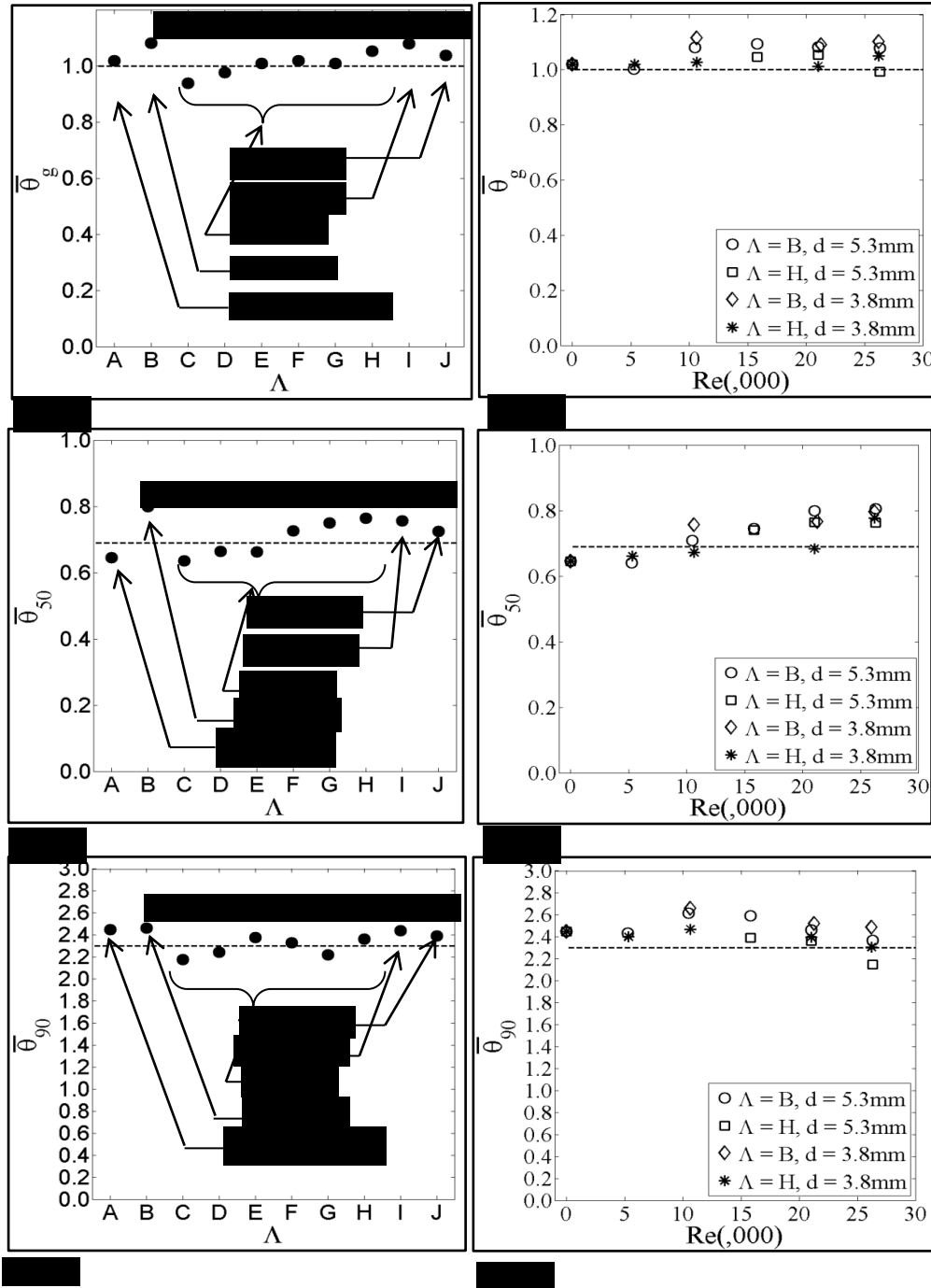


Fig. 17: Plots of hydraulic indices  $\bar{\theta}_g$ ,  $\bar{\theta}_{50}$  and  $\bar{\theta}_{90}$  against layout,  $\Lambda$  in (a) to (c) and against Reynolds number,  $Re$  in (d) to (f). Dashed lines indicate standard values of the hydraulic indices for a perfect CSTR.  $\bar{\theta}_g$  = mean dimensionless residence time,  $\bar{\theta}_{50}$  = mean dimensionless median time and  $\bar{\theta}_{90}$  = mean dimensionless time to capture 90% tracer.

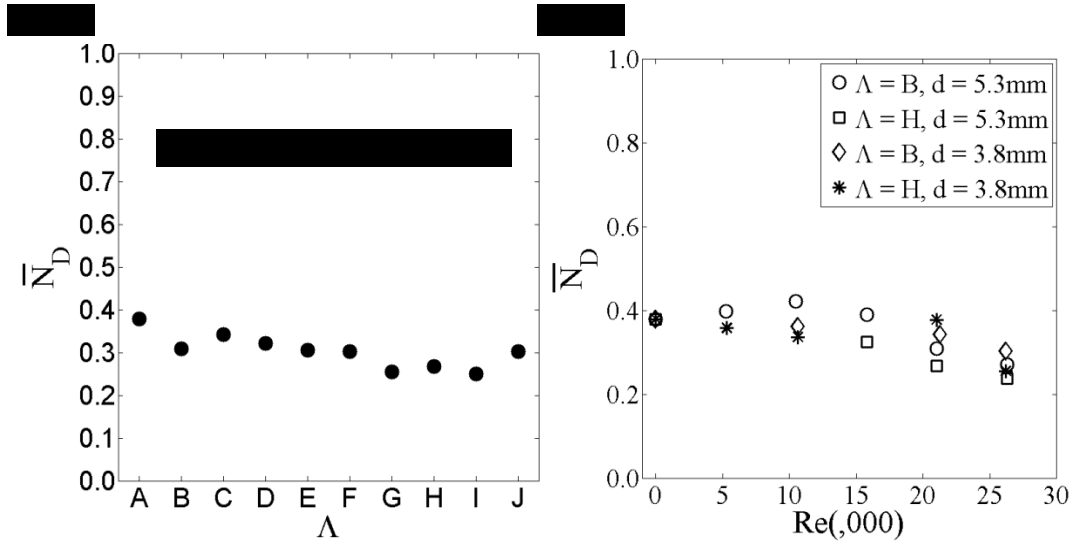


Fig. 18: Means values of the dispersion number,  $\overline{N_D}$  obtained from axial dispersion model for varying (a) layout,  $\Lambda$  and (b) Reynolds number,  $Re$  and diameter,  $d$ . Note that each data point is the average of 14 to 18 repeated tests.

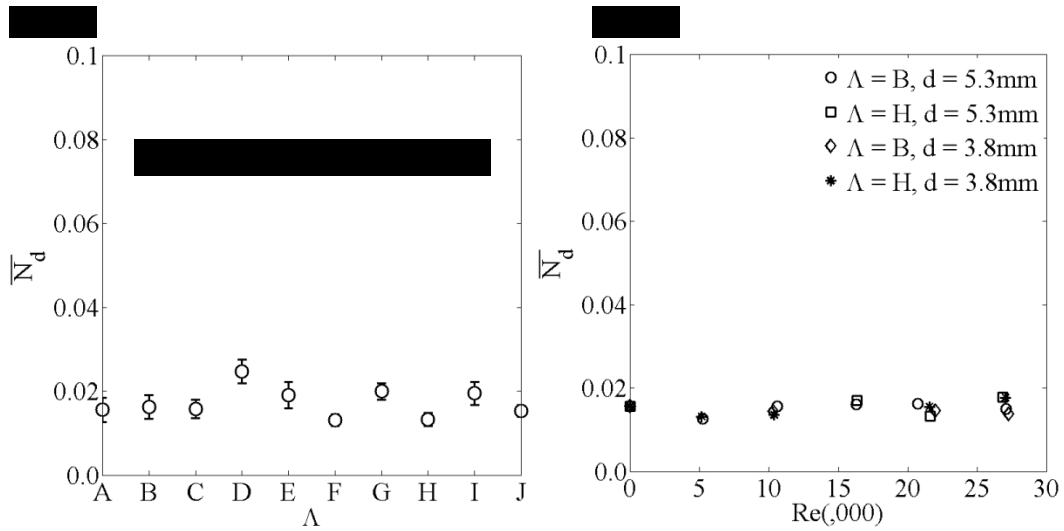


Fig. 19: Means values of the dispersion number,  $\overline{N_d}$  of the plug flow compartment, obtained from dispersive compartmental model for varying (a) layout,  $\Lambda$  and (b) Reynolds number,  $Re$  and diameter,  $d$ . Note that each data point is the average of 14 to 18 repeated tests.

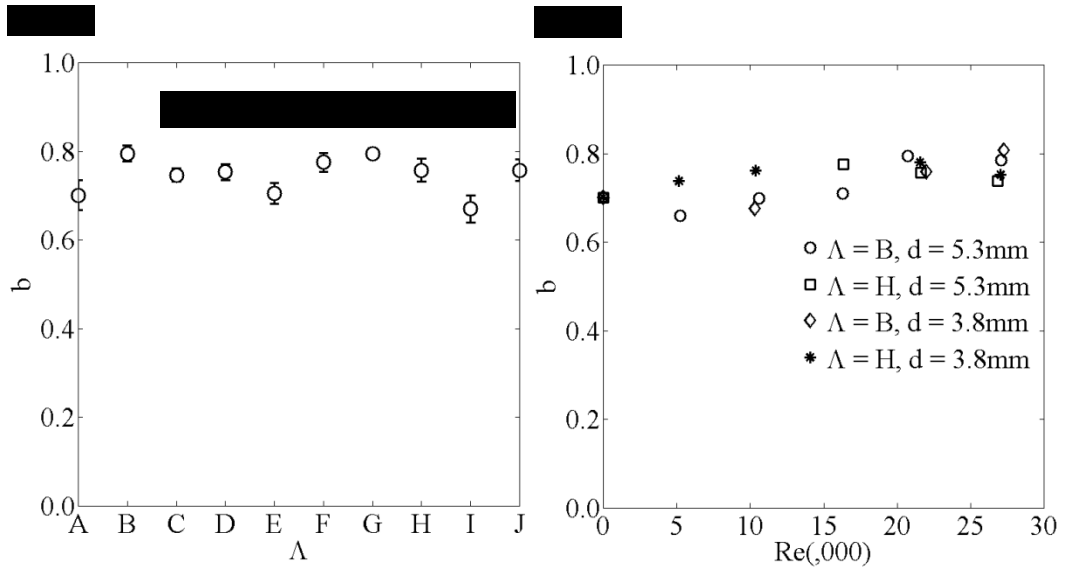


Fig. 20: Dispersive Compartmental Model estimated  $b$  for different (a) layouts,  $\Lambda$  and (b) Reynolds numbers,  $Re$  and diameters,  $d$  of jets.

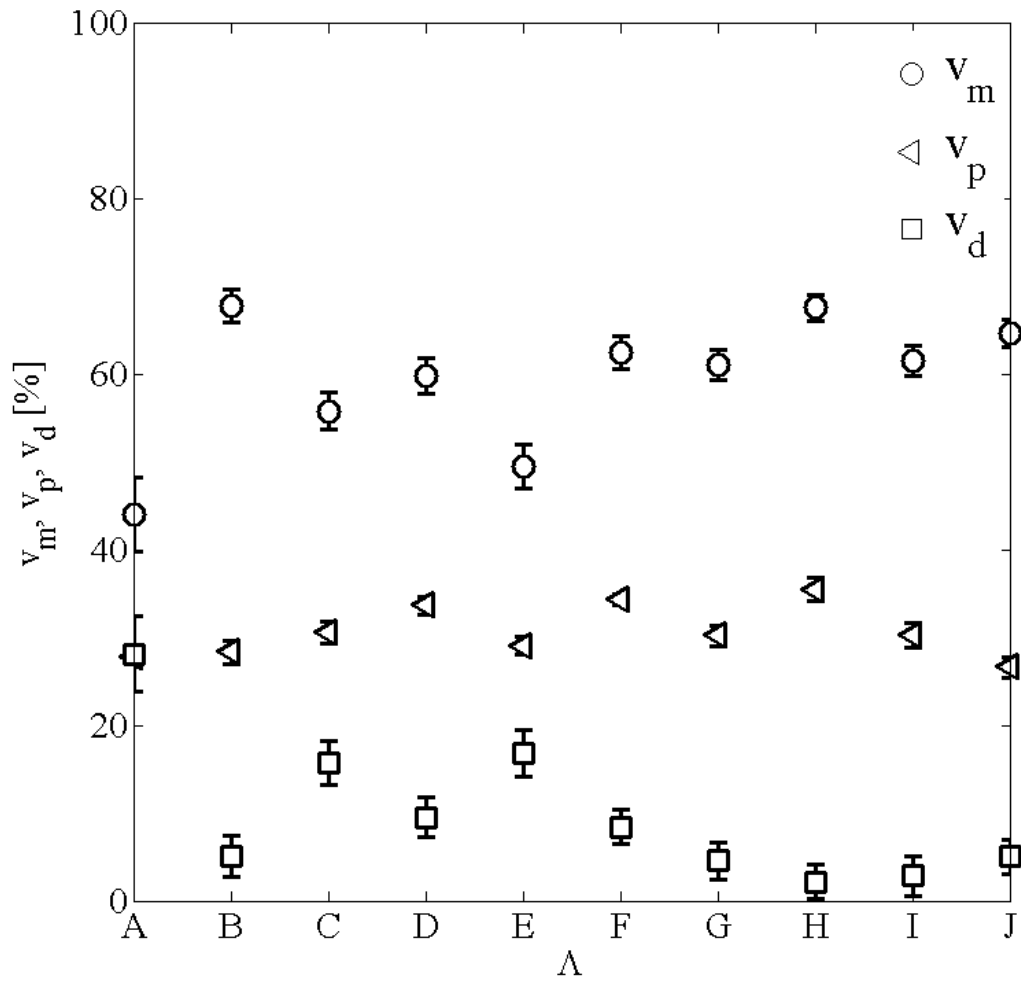


Fig. 21: Dispersive Compartmental Model estimated volumes of percentages of plug flow volumes,  $v_p$ , mixed flow volumes,  $v_m$  and dead flow volumes,  $v_d$  for different layouts,  $\Lambda$  and with  $Re = 21,400$  and  $d = 5.3\text{mm}$ . Error bars are margin of error at the 95% confidence limit.

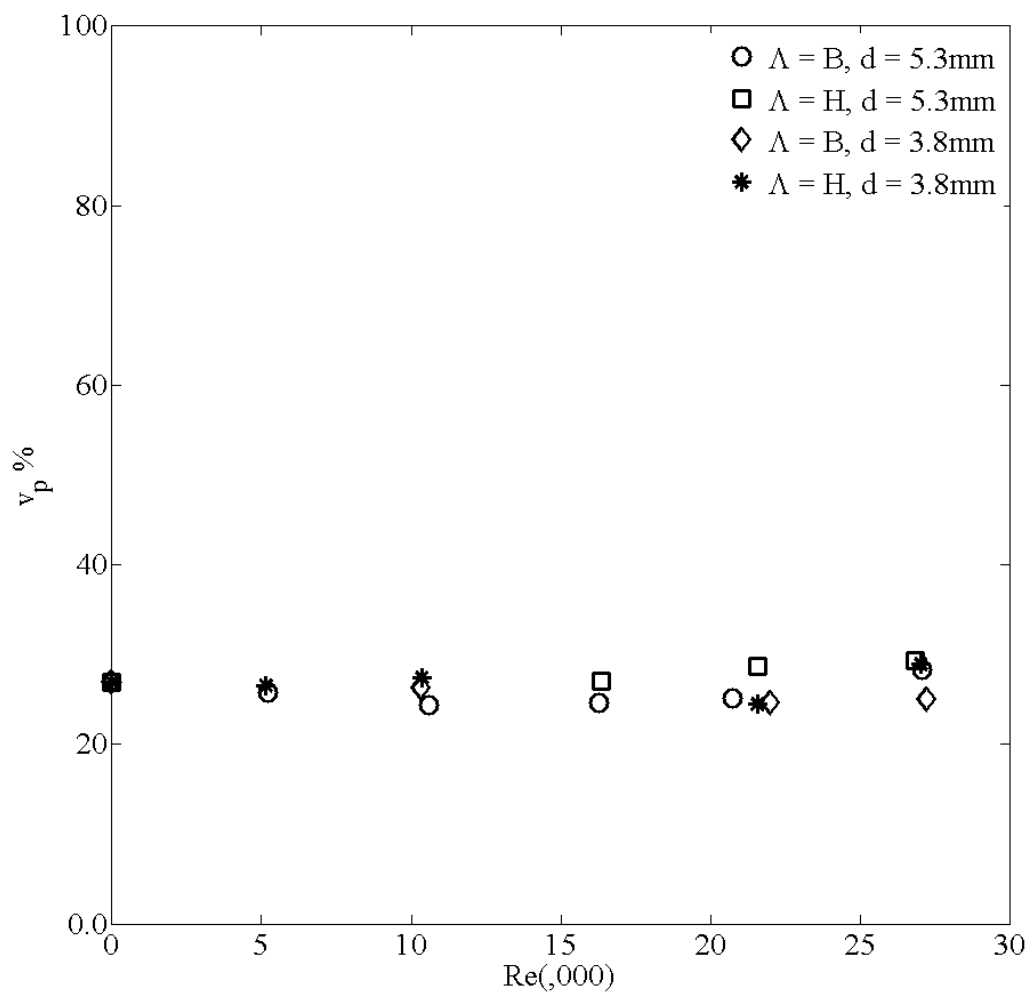


Fig. 22: Dispersive Compartmental Model estimated percentages of plug flow volume,  $v_p$ , for different Reynolds number,  $Re$  and jet diameter,  $d$ .

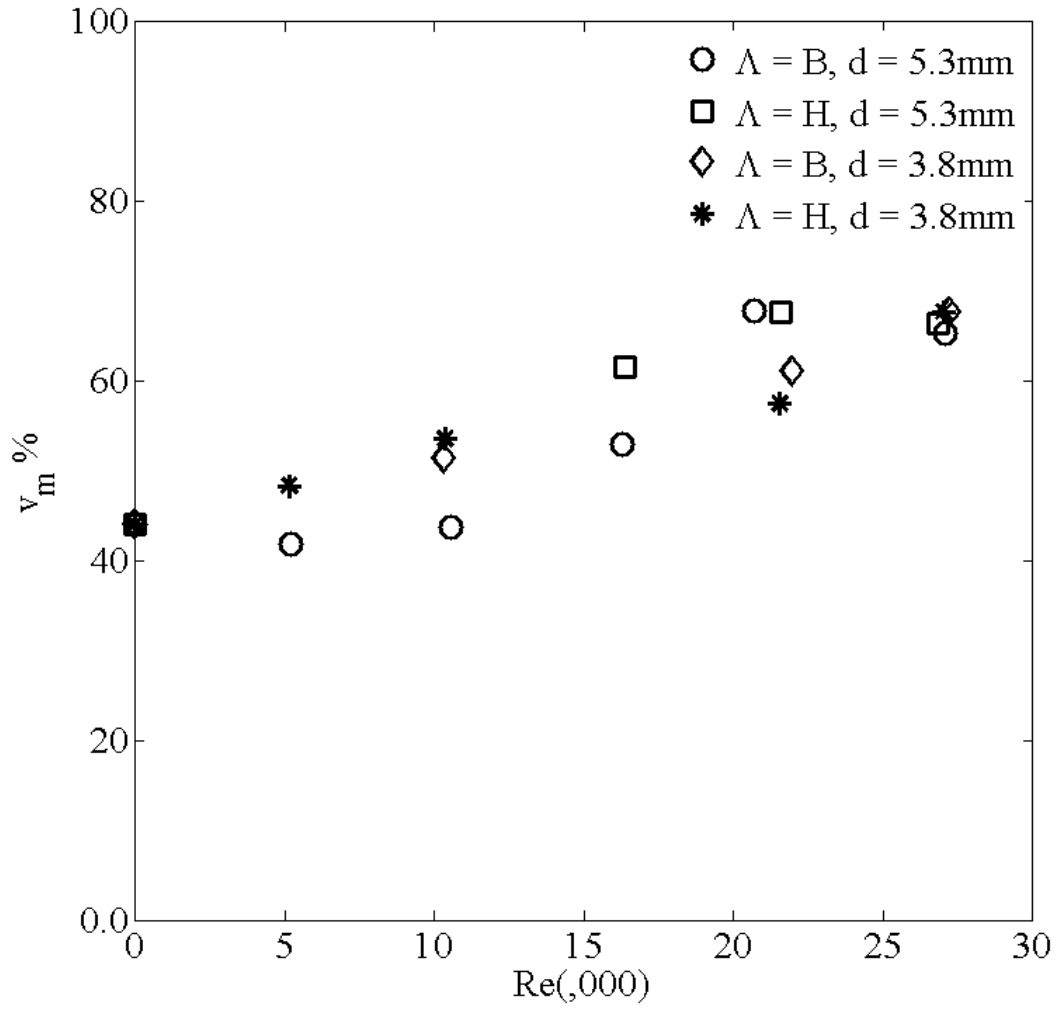


Fig. 23: Dispersive Compartmental Model estimated percentages of plug flow volume,  $v_p$ , for different Reynolds number,  $Re$  and jet diameter,  $d$ .

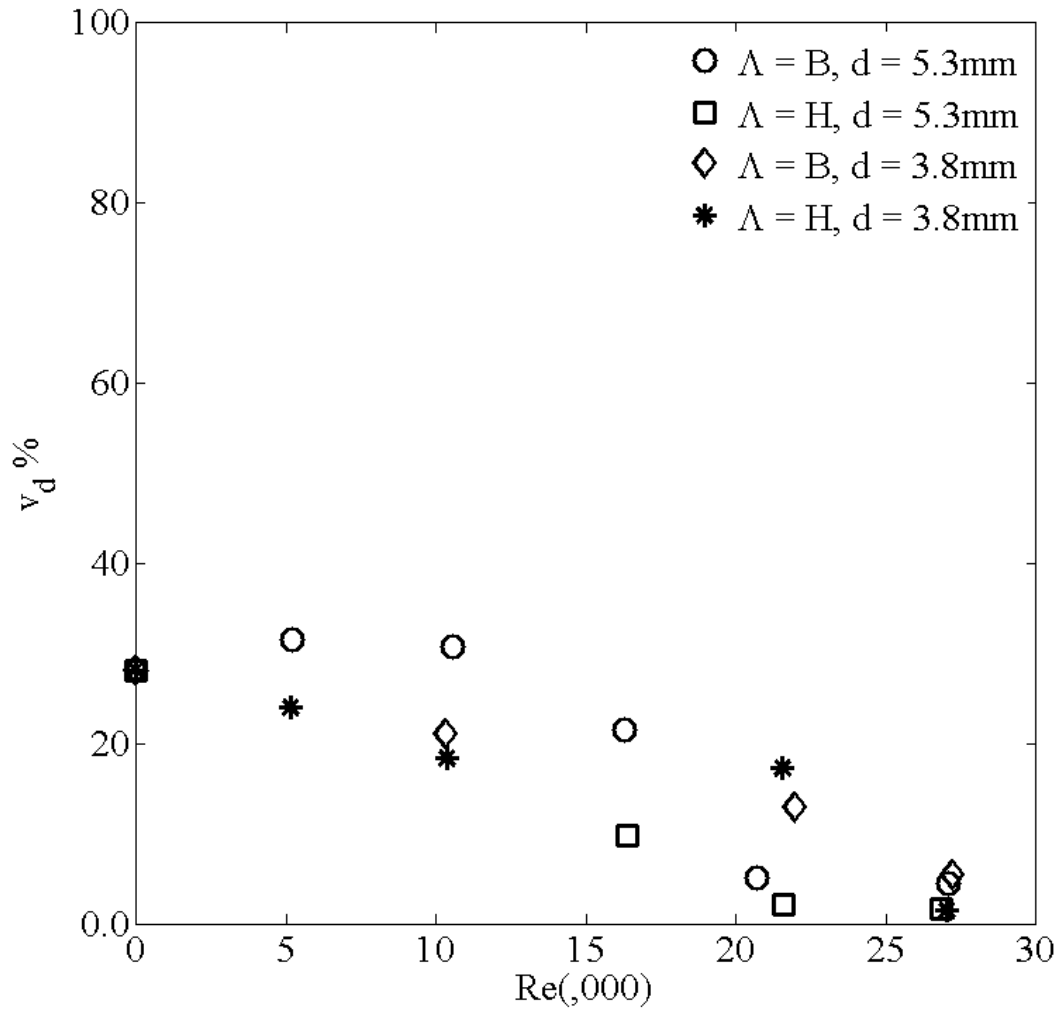


Fig. 24: Dispersive Compartmental Model estimated percentages of dead flow volume,  $v_d$ , for different Reynolds number,  $Re$  and jet diameter,  $d$ .

## **Chapter 3 : Planar Laser Induced Fluorescence (PLIF) Experiment in a Mixing Tank**

---

### **3.1 Introduction**

Turbulent jets have diverse industrial applications, such as mass transfer, reaction and solid-fluid processes. A common aim of these applications is to develop a perfect continuous stirred tank reactor (CSTR) but for practical purposes, the reactors are not perfectly CSTR and thereby the efficiency of the applications is reduced. A potential application in a wastewater treatment plant (WWTP) is the removal of organic materials comprised of fat, oil and grease (FOG) from inorganic grit particles in a preliminary treatment system known as grit removal system. The system requires a CSTR where strong turbulent stresses work on the removal of FOG. Multiple transverse jets are commonly used to produce strong turbulent stresses in a CSTR. In order to develop a reactor that is effective for removing FOG from grit, it is important to investigate the flow behavior in the reactor in order to acquire a deeper understanding of the mixing performance of the reactor.

In this study, the mixing flow was visualized using an optical diagnostic technique - planar laser-induced fluorescence (PLIF). PLIF has been widely used over the past three decades as a non-intrusive technique in fluid flows. In this technique, the concentration of fluorescent dye is measured in a particular plane within the flow. Flow visualization is carried out using spatial maps and time series of dye concentration within the plane. For example, PLIF was used for visualizing jets in a cross flow by Yoda and Fiedler (1996), turbulent mixing with jets by Reungoat et al.(2007) and mixing flow in a reactor with multiple transverse jets by Luo et al. (2013). In these studies flow structures, mixing layers, boundaries and mixing performance of a reactor were investigated.

Mixing performance depends on the operating conditions of the jets in a reactor with multiple transverse jets. Unger and Muzzio (1999) studied mixing

performance in two reactors with different geometries for a range of jet Reynolds number and showed that the jet Reynolds number had a significant influence irrespective of the geometry of the reactor. Luo et al. (2013) obtained improved mixing performance for high velocities of jets but Sandell et al. (1985) observed decreasing mixing performance for increasing Reynolds number using multiple jets. A different result is observed in the study of Tucker and Suh (1980). This study showed that mixing performance was improved for increased Reynolds number until a threshold value of 1000. Increasing the Reynolds number above this threshold value contributed nothing to the mixing performance. However, these findings may not apply to reactors with different geometry. Therefore, it is essential to investigate mixing performance of a reactor for a range of Reynolds numbers and to understand the flow behavior inside the reactor.

Flow visualization, for understanding the mixing performance, is usually carried out in a plane of interest. Flow segregation, vortex and chaotic flow regimes are observed from dye concentration in the plane (Hu et al. 2004; Baydar and Ozmen 2006). Identifying these flow regimes is important to understand the effect of Reynolds number on the mixing performance. Yoda and Fiedler (1996) studied flow regimes for free round jets using PLIF and observed flow vortices. The vortex shedding becomes unstable when the Reynolds number was increased. In the case of confined jets, Santos and Sultan (2013) observed stable flow regimes (either segregated or vortex flow) for jet-impingement in a confined space, at lower Reynolds numbers near the impingement, and chaotic flow at high Reynolds numbers. Very little is known about the flow regimes that occur in a confined space with multiple transverse opposing jets in a staggered layout. Flow visualization is an ideal way to study these flow regimes.

The present research builds on the RTD experiments and analysis described in the Chapter 2. That research determined the jet configurations and operating conditions that maximized the mixed flow volume within a square tank equipped with transverse jets and two inlets and outlets. The mixed flow volume was found

to be highest using four cross jets operating at Reynolds numbers greater than 20,000. The PLIF measurements presented in this chapter were used to delineate flow regimes, such as dead flow zones and mixed flow zones for varying Reynolds numbers.

PLIF measurements were conducted in the outlet plane (i.e., the horizontal plane located on the centerline of the outlets) for various Reynolds numbers. The outlet plane is strongly affected by upstream changes in geometry and operating conditions for the case of convective flows and, therefore, it is an ideal location for evaluating mixing performance (Liscinsky et al. 1993). A series of PLIF measurements were carried out to confirm the conclusions of the RTD study that mixing performance improved with increasing jet Reynolds number. The mixing performance was evaluated by visualization of dead flow zones from spatial distribution of concentration maps. In addition, concentration time series extracted from the PLIF images were used to validate the dispersive compartmental model (DCM) of Chapter 2.

### **3.2 Experimental Setup and Methods**

Fig. 25 shows a schematic diagram of the square tank and the PLIF experimental setup. The square tank was made of acrylic plastic for optical transparency. The tank was 42.7 cm square in plan with a height of 43.6 cm. Water from an elevated constant head tank enters the tank through the inlet pipes and the water level in the tank was controlled using a valve located downstream. Detail descriptions of the constant head tank, upstream supply, downstream control valves and positions for transverse jets can be found in Chapter 2. Fluorescent dye was injected into the flow using a double syringe pump (LEGATO 200, KD Scientific, USA) via two ports located on the inlets lines just upstream of the reactor as shown in Fig. 25. The PLIF system used a Nd:YAG laser (SOLO 120-15Hz, NewWave Research, USA) as the light source and a charged-couple device (CCD) camera (Hamamatsu C8484-05cp, Japan) with lens and filter for capturing light signals

emitted from dye particles. The laser produced a beam with a wavelength of 532 nm with energy of 120mJ per pulse. A laser light sheet was used to illuminate a horizontal plane passing through the center of the outlet as illustrated in Fig. 25. The thickness of the sheet was approximately 1.0 mm. The camera was mounted perpendicular to the laser sheet. The camera produces images with a resolution of 1344x1024 pixels with 12-bit depth at a rate of 10 Hz. The camera was equipped with a 50 mm lens (Nikon, Japan) which was located approximately 80 cm from the laser sheet so that field of view included slightly more than 25% of the area of the square tank. A 560 nm wavelength narrow band pass filter was placed in front of the lens, which allowed the light emitted by the fluorescing dye to reach the camera and scattered laser light was blocked. The camera, the laser and the syringe pump were connected to a PC equipped with data acquisition software, Dantec Dynamic Studio 3.41 (Dantec Dynamics A/C, USA). The PC synchronized the laser, camera and syringe pump. The software was also used for processing the captured PLIF images.

Experiments were conducted with two jet layouts: layout A and layout B. Table 3.1 shows the layouts. Layout A is the control case, where no jets were used and layout B has four jets, two from each sidewall. The jet diameter was 5.3 mm. The jet Reynolds number was varied from 0 to 27,000 and the 6 test cases are listed in Table 3.2. In all cases, the longitudinal flow rate was set to 3.5 L/s and water depth in the tank was 41.5 cm.

PLIF measurements were carried out using Rhodamine 6G (Rh6G) as a tracer material. Rh6G was chosen because of its solubility in water, low sensitivity to temperature, and its peak absorption is at 532 nm (Luo et al. 2013; Crimaldi 2008). The absorbed energy of the light is re-emitted by Rh6G at 560 nm, which is captured by the camera. The camera measures the intensity of light, which is related to the concentration of the dye. The relation between pixel intensity and concentration was determined by using 14 different concentrations of Rh6G dye ranging from 0 to 35  $\mu\text{g/L}$  at five different laser beam energy levels (20%, 40%,

60%, 80% and 100% of full energy level). For the calibration measurements, the tank was filled with a known volume of water and a known amount of dye was completely mixed with the water. The camera was used to capture 20 images at 10 Hz at each energy level. The spatial and temporal average of the pixel intensity was computed for each corresponding known concentration of the fluorescent dye. Dantec Dynamic Studio 3.41 (DDS) was used to plot the calibration equation at each energy level and the  $R^2$  values (i.e., square of the correlation coefficient) increased as the laser energy increased. The lowest  $R^2$  value was 0.907 for 20% energy level and the highest was 0.985 at 100% energy level, where 100% energy level corresponds to 120 mJ. The calibration curve at 100% energy level is shown in Fig. 26. All measurements were conducted using 100% energy level. The Dantec Dynamic Studio 3.41 used this calibration curve to convert the raw PLIF images into tracer concentration maps.

PLIF measurements were carried out using a step input of tracer. The step function was chosen so that flow regimes are visualized for continuous flow of tracer through the inlet. The two syringes were filled with 100 mL of tracer with a concentration of 15.86 mg/L of Rh6G dye. This high concentration of the tracer was injected into the inlet flow of the tank at a flow rate of 66.2 mL/min. This configuration was designed such that a completely mixed flow inside the tank would produce a uniform concentration of 10  $\mu\text{g/L}$  for a jet-Reynolds number of zero (i.e., no jet case). As the jet-Reynolds number was increased the well-mixed concentration decreased slightly due to the additional volumetric flow rate and at the maximum Reynolds number of 27000 it was 9.4  $\mu\text{g/L}$ . The residence time of tank at a flow rate of 3.5 L/s with no jets was 22.3 s and the duration of the step function (i.e., the time period dye was injected) was set to 100s, four times the residence time.

The tracer volume available for injection was limited to 100 mL in each syringe, which is the highest capacity of the syringe that fits in the syringe pump. The rate of tracer injection (i.e., 66.2 mL/min) was chosen to ensure that the duration of

tracer injection was sufficiently long enough for the step function (i.e., four times the residence time). Note that the tracer injection rate was determined based on volume of tracer and duration of the tracer injection. These constraints resulted in a tracer injection rate that was relatively small and the tracer entering the inlet pipes has very little momentum. Consequently, the tracer did not mix completely across the inlet pipe and the water entering the mixing tank had tracer concentrations that exceeded the completely mixed value of 10  $\mu\text{g/L}$ .

Prior to injecting tracer, the background concentration was first measured. Fifty images were captured, and converted to concentration maps by applying the calibration curve. The mean of these 50 concentration maps was used as the background concentration map. The camera was then triggered to begin capturing images at the instant tracer injection was started. The laser was operated at 10Hz, and 1000 images were captured for a total duration of 100s for each experimental run. The experimental run was repeated three times for each test to reducing uncertainty.

Fig. 27 shows an example of an instantaneous concentration map from one test. The field of view relative to the tank is also shown in this figure. The field of view of the images was 267 mm x 203 mm. Two edges of the captured images were trimmed due to interference from the sidewall and outlet boundary of the tank. The figure shows that the concentration was lower than 10  $\mu\text{g/L}$  in large parts of the plane, and that concentrations from approximately 15 $\mu\text{g/L}$  to 35 $\mu\text{g/L}$  were observed near the outlet. The observed images contained artifacts due to scratches on the front wall and the bottom of the tank. The scratches on the front wall caused distortions in the laser sheet that produced streaks in the PLIF images. The scratches on the bottom caused localized distortions to appear in the PLIF images. The artifacts in the PLIF images result in errors in the concentrations, estimated from the PLIF images. Fortunately, the image area near the outlet was free of these artifacts and, therefore, the concentration time-series extracted from this area were not corrupted by these types of errors. Note that only qualitative

analyses were applied to regions of the image that contained these types of distortion errors.

### 3.3 Analysis

Concentration at the outlet is important for measuring the mixing performance. Time series concentrations were extracted from a strip 50 mm by 1 mm across the outlet. The strip was bounded by  $x = 399$ ,  $x = 400$ ,  $y = 102$  and  $y = 152$ . This strip is located at the center of the outlet and 30 mm upstream of the outlet. The average concentration within this strip was assumed to be representative of the concentration at the outlet. Time series of these outlet concentrations were obtained by processing 1000 images from each run. A steady state concentration,  $C_{ss}$  was determined from the time series concentration by averaging the concentration for the period from 65s to 85s, which is three to four times the mean residence time. During this period, the concentration was approximately steady at the outlet, since the standard deviations of the mean were small; they only varied from 4.0% to 8.3%.

F-curves are useful to understand the mixing behavior. F-curves were derived from the time series of concentration at the outlet. Time series of concentrations are typically made non-dimensional by dividing by the inlet concentration, assuming the tracer is fully mixed at the inlet. Unfortunately, the tracer was not fully mixed at the inlet due to experimental limitations. Therefore, the steady state concentration was used as the divisor to obtain an F-curve from the time series concentration. This F-curve was used for application of the DCM, and the results are meaningful when the steady state concentration approaches the fully mixed concentration of the tank.

The dispersive compartmental model (DCM) described in detail in the Chapter 2, was applied to determine the mixed flow volume in the tank. In the DCM, the reactor was divided into three compartments: plug flow, mixed flow and dead flow compartments. A quantitative measure of the mixing performance is the size

of the mixed flow compartment inside the tank. The volumes of the compartments were obtained by predicting model F-curves. The model F-curves were predicted using nonlinear optimization and the experimental F-curves. The DCM model F-curve is obtained by integrating the expression for the DCM model E-curve (Eq. (2.12) and is given by,

$$F_{DCM}(t) = \begin{cases} \int_0^{V_p/Q} \frac{bQ}{V_m} e^{-\left(\frac{tQ}{V_p} + 1\right)^2 / (2\sqrt{N_d})} \\ \int_{V_p/Q}^{\infty} \frac{bQ}{V_m} e^{-\left(\frac{Qt}{V_m} + \frac{V_p}{V_m}\right)} \end{cases} \quad (3.1)$$

where  $V_p$  is the volume of the plug flow compartment,  $V_m$  is the volume of mixed flow compartment,  $N_d$  is the axial dispersion number,  $Q$  is flow rate of the mainstream, and  $b$  is a correction coefficient. The coefficient indicated the deviation of the performance of the mixed flow compartment from a perfect CSTR.

The DCM was applied with the following constraints,

$$V_m + V_p \leq V \quad (3.2)$$

$$V_p > 0 \quad (3.3)$$

$$V_m > 0 \quad (3.4)$$

$$b \leq 1 \quad (3.5)$$

where  $V$  is the total volume of the tank and the dead flow volume  $V_d$  is given by,

$$V_d = V - V_p - V_m \quad (3.6)$$

In predicting model F-curves, the four model parameters,  $V_p$ ,  $V_m$ ,  $b$  and  $N_d$ , were optimized. A nonlinear optimization method was used to compute the optimal

model parameters by minimizing the difference between the modelled and measured F-curves. The Levenberg-Marquardt algorithm (LMA) was used to search for the minimum value of the sum of squared errors (*SSE*) defined as,

$$SSE = \sum_{i=1}^n (F_m(i) - F_e(i))^2 \quad (3.7)$$

where,  $F_m$  is the modelled curve and  $F_e$  is the measured experimental curve. A MATLAB optimization tool (*patternsearch*) was used to compute the minimum of the SSE, where  $F_m$  was used as an object function. Eq. (3.1) was used as the object function for optimizing the model parameters. Eqs. (3.2-3.5) were used as constraints for performing the optimization. Fig. 28 shows a typical example of model and experimental F-curves. The model F-curve was observed in good agreement with the experimental data from initial time to time less than 5 sec, and at time larger than 35 sec.

### 3.4 Results

Sequential concentration maps were evaluated qualitatively using visual observation to understand the mixing performance associated with the transverse jets. These images were smoothed using a low pass filter with a 3x3 kernel to remove noise. Concentration maps at six different time steps ( $t = 0.2 \tau, 0.5 \tau, 1.0 \tau, 2.0 \tau, 3.0 \tau$  and  $4.0 \tau$ ) are shown for a jet Reynolds number of zero (i.e., no jets) in Fig. 29 and for a jet Reynolds number of 27,378 in Fig. 30. At time step  $0.2\tau$ , tracer was first visible near the outlet boundary locating at upper and lower right corners in Fig. 29, whereas tracer was observed at left edge of the plane in Fig. 6. In both figures, tracer was not mixed instantly. Tracer was transported to outlet by following the main hydraulic flow path in the tank in no jet condition, whereas transverse jets dispersed tracer laterally resulting in the appearance of tracer at left edge in Fig. 30. Tracer was observed accumulating at the upper and lower right corners in both figures at time step  $0.5\tau$  due to tracer transport through the main hydraulic flow path. This signified that these were locations for potential dead

flow zones where tracer was trapped. In later time steps, the variance of tracer concentration was decreasing. The average concentrations at time steps larger than  $2\tau$  were higher in the test with no jet than in the test with jet. This indicated that mixing performance was increased due to application of the transverse jets.

Steady state concentrations at the outlet are compared with fully mixed concentrations in Table 3.3 for the six jet Reynolds numbers. The fully mixed concentration  $C_{fm}$  is the theoretical value of concentration if the tracer was mixed fully throughout the entire tank resulting in zero variance of concentration. In tests 1, 2 and 3 ( $Re = 0, 5,600$  and  $10,700$ ) the tracer was not fully mixed inside the entire tank volume, because the steady state concentrations were 1.46, 1.32 and 1.28 times of the fully mixed concentration, respectively. At the three higher Reynolds numbers ( $16,700, 20,900$  and  $27,400$ ), fully mixed concentrations were almost achieved at the outlet. For these conditions, the steady state concentration at the outlet was 1.23, 1.16 and 1.11 times of the fully mixed concentration. These values indicated that tracer was not fully mixed inside the tank because of tracer trapped in dead flow zones in the test with no jets. There was a significant dead flow zones at this condition, and the dead flow zone was reduced significantly at Reynolds number of 27400.

In Fig. 31, plots of the normalized concentration  $C/C_{ss}$  at the outlet versus dimensionless time  $t/\tau$  are presented for the average of three repeated runs at each of the six jet-Reynolds numbers. The curves are similar to conventional F-curves, but instead of being normalized by the fully mixed concentration at the inlet, they were normalized using the steady state concentration at the outlet. Therefore, the effect of the dead flow zone, which was determined by the difference between one and the asymptotic value of each F-curve, was not possible to interpret. However, the average slopes of the F-curves, were examined to understand the mixing performance. A measure of the average slope is the time it takes for the F-curve (i.e.  $C/C_{ss}$ ) to reach a value of 0.90. At  $Re = 0$  (no jets) the F-curve rises slowly to the asymptotic value. This suggests the existence of a large dead flow zone, from

which tracer was released slowly to the main hydraulic flow path. At higher Re values F-curves rise slightly faster. Based on the observation of the plots, transverse jets aided to reach 90% of steady state concentration at the outlet by the time less than  $1.65\tau$ , whereas  $1.9\tau$  was required to reach that level of concentration at the outlet in the test with no jets. This demonstrates that transverse jets also performed a better mixing performance by fast mixing.

The locations of dead flow zones were evaluated from contour maps of steady state concentration. Fig. 32 presents contour plots of the steady state concentration, which was normalized by the steady state concentration at the outlet. The steady state concentration was the ensemble average of the concentration maps from  $t = 65$  to  $85$  sec. Note that all the contour plots were slightly distorted due to scratch in the bottom of the tank located at  $y = 21$  mm. The contour plots of Fig. 32(a) shows that contours are roughly symmetric with respect to the direction of flow towards the outlet. In the other plots, no symmetric contours are observed because transverse jets caused lateral dispersion of tracer material. This indicates that transverse jets help in mixing tracer in the entire tank. The contour maps were the ensemble average of concentration, where isolated high and low tracer concentration are possible locations of dead flow. A high tracer concentration at the lower right corner was observed in the Fig. 32(a) to Fig. 32(c). This location was a dead flow zone where tracer was trapped. The concentration at this location was reduced for high Reynolds number of jets as shown in Fig. 32(d). In this contour map, a high concentration at the upper right corner was not dead flow zone because this tracer was continuous to the outlet flow, that is, not isolated. The gradient of concentration was calculated for each contour map. Absolute gradients were 0.30, 0.27, 0.24 and 0.22 for the tests with Reynolds number 0, 10700, 16700 and 27400, respectively. These decreasing values with increasing Reynolds number indicate that the transverse jets increased the mixing performance of the tank.

The DCM was used to predict mixed flow, plug flow and dead flow volumes at different Reynolds numbers using the F-curves plotted in Fig. 31 and these results are plotted in Fig. 33. In Table 3.4, these predictions are compared with the corresponding results of the DCM computed from the E-curves in the RTD experiments from Chapter 2. At the three lowest Reynolds numbers ( $Re \leq 10700$ ) predictions based on the PLIF measurements do not agree very well with the values predicted from the RTD measurements. In particular, the PLIF predicted mixed flow volumes are approximately 1.6 times larger the values predicted from the RTD measurements. The reason for these poor agreements is that the tracer was not well mixed with inflow, and as a result, the outlet concentration was higher than the theoretical fully mixed concentration.

However, at the three largest Reynolds numbers the PLIF and RTD predictions are in reasonable agreement particularly for  $Re = 16,700$  and  $27,400$ . At these higher Reynolds numbers the PLIF predicted plug, mixed and dead flow volumes were on average 1.09, 0.93 and 1.25 times larger than the RTD based predictions. The DCM predicts that as the Reynolds number increased from 16,700 to 27,400 that the mixed flow volume increased and the dead flow volume decreased using either the PLIF or RTD measurements. The highest mixed flow volume and lowest dead flow volume was predicted to occur at the highest Reynolds number in both cases.

### **3.5 Conclusions**

The PLIF experiments demonstrated that transverse jets improved the mixing performance of the tank. The best mixing occurred when the jet Reynolds number was set to the highest value of 27400. The tracer was mixed more rapidly at this Reynolds number. At this Reynolds number,  $C_{ss}$  was close 90% of  $C_{fm}$ , and the gap between  $C_{ss}$  and  $C_{fm}$  was reduced when the Reynolds number was higher than 16700. Therefore, increases of Reynolds number improved the mixing performance of the tank.

The DCM was applied to the PLIF experiments with Reynolds number higher than 16700. The estimates of plug flow, mixed flow and dead flow volumes were comparable with the volumes found in the RTD experiments. The successful comparison indicated that the DCM could be used in tracer studies of computational fluid dynamics (CFD) models (Furman and Stegowski 2011) for computing the volumes of plug flow, mixed flow and dead flow zones. The volumes could be used for validation of the models.

The locations of dead flow zones were demarcated in the PLIF experiments. Dead flow zones were observed in the upper right corner, which was the area between the two outlets, and the lower downstream corner of the tank. These locations were also the stagnant flow zones based on the geometric shape of the tank. These are also possible locations for grit deposition.

## Reference

Ahimou, F., Semmens, M. J., Novak, P. J., and Haugstad, G. (2007). "Biofilm cohesiveness measurement using a novel atomic force microscopy methodology." *Appl. Environ. Microbiol.*, 73(9), 2897-2904.

American Society for Testing and Materials. (2000). "ASTM designation E 8-00 Standard Test Methods for Tension Testing of Metallic Materials." ASTM.

Anderson, R., and Holmberg, M. (2006). "Energy Conservation in Wastewater Treatment Operation." Lund University, Sweden: Master Thesis.

Andoh, R. Y. G., and Neumayer, A. (2009). "Fine Grit Removal Helps Optimize Membrane Plants." *WaterWorld*, 25(1), 28-28.

AWWA, A. (1998). "WPCF-Standard Method for Examination of Water and Wastewater."

- Baydar, E., and Ozmen, Y. (2006). "An experimental investigation on flow structures of confined and unconfined impinging air jets." *Heat and Mass Transfer*, 42(4), 338-346.
- Boller, M., and Blaser, S. (1998). "Particles under stress." *Water Science and Technology*, 37(10), 9-29.
- Brenner, A., and Diskin, M. H. (1991). "Model study of jet-circulated grit chamber." *J. Environ. Eng.*, 117(6), 782-787.
- Bridgeman, J., Jefferson, B., and Parsons, S. A. (2010). "The development and application of CFD models for water treatment flocculators." *Adv. Eng. Software*, 41(1), 99-109.
- Chisti, Y. (2001). "Hydrodynamic damage to animal cells." *Crit. Rev. Biotechnol.*, 21(2), 67.
- Coca, J., Gutiérrez, G., and Benito, J. (2011). "Treatment of Oily Wastewater." *Water Purification and Management*, 1-55.
- Crimaldi, J. (2008). "Planar laser induced fluorescence in aqueous flows." *Exp. Fluids*, 44(6), 851-863.
- De Silva, V., and Bates, B. R. (2004). "Fine grit removal challenges in wastewater treatment plants." *Proceedings of the Water Environment Federation*, 2004(7), 258-264.
- do Prado, G. S., and Campos, J. R. (2009). "The use of image analysis to determine particle size distribution of grit carried by sewage." *Engenharia Sanitaria E Ambiental*, 14(3), 401-410.

Dueck, J., Pikushchak, E., and Minkov, L. (2009). "Modelling of change of the classifier separation characteristics by water injection into the apparatus." *Thermophysics and Aeromechanics*, 16(2), 247-258.

El-Din, A. G., and Smith, D. W. (2002). "A neural network model to predict the wastewater inflow incorporating rainfall events." *Water Res.*, 36(5), 1115-1126.

Environment Canada. (2010). *Wastewater Systems Effluent Regulations*. Canada.

Finger, R. E., and Parrick, J. (1980). "Optimization of Grit Removal at a Wastewater Treatment Plant." *Journal (Water Pollution Control Federation)*, 52(8), pp. 2106-2116.

Fouad, M., Kishk, A., and Fadel, A. (2014). "The effects of scum on sewer flows." *Urban Water Journal*, 11(5), 405-413.

Frohnäpfel, B., Lammers, P., and Jovanović, J. (2008). "The role of turbulent dissipation for flow control of near-wall turbulence." *New Results in Numerical and Experimental Fluid Mechanics VI*, 268-275.

Furman, L., and Stegowski, Z. (2011). "CFD models of jet mixing and their validation by tracer experiments." *Chemical Engineering and Processing: Process Intensification*, 50(3), 300-304.

Gang, D. D., Rakesh, B., and Shankha, B. (2010). "Wastewater: Treatment Processes." *Encyclopedia of Agricultural, Food, and Biological Engineering, Second Edition*, 1(1), 1825-1836.

Gravette, B., Strehler, A., Finger, D., and Palepu, S. (2000). "Troubleshooting a grit removal system." *Proceedings of the Water Environment Federation*, 2000(11), 332-369.

Gruber, Y., Farchill, D., and Goldstein, M. (1988). "Design, Testing and Operation of Grit Chambers with Hydraulic Roll." *Water Science and Technology WSTED4 Vol. 20, no. 4/5, P 237-248, 1988. 6 Fig, 11 Ref.*

Gutierrez, C. G., Dias, E. F., and Gut, J. A. (2010). "Residence time distribution in holding tubes using generalized convection model and numerical convolution for non-ideal tracer detection." *J.Food Eng.*, 98(2), 248-256.

Habib, A. (2008). "Investigating the performance of an aerated grit chamber". University of Alberta, M.Sc. thesis, Canada.

Hart, J., Guymmer, I., Jones, A., and Stovin, V. (2013). "Longitudinal Dispersion Coefficients within Turbulent and Transitional Pipe Flow." *Experimental and Computational Solutions of Hydraulic Problems*, Springer, 133-145.

Hay, T. T. (1946). "Experience in Grit Removal and Handling at Racine, Wis." *Sewage Works Journal*, 18(1), 54-65.

Hendricks, D. W. (2006). *Water treatment unit processes: physical and chemical*. CRC press.

Hu, H., Saga, T., Kobayashi, T., and Taniguchi, N. (2004). "Analysis of a turbulent jet mixing flow by using a PIV-PLIF combined system." *Journal of Visualization*, 7(1), 33-42.

Ibemere, S., and Kresta, S. (2007). "Modelling the Mixing and Dissolution Kinetics of Partially Miscible Liquids." *Chem.Eng.Res.Design*, 85(5), 710-720.

Keane, J. J., and deSilva, V. (2009). "Dealing with Fine Grit at WWTPs." *Proceedings of the Water Environment Federation*, 2009(10), 6149-6159.

Kwon, B., Shon, H. K., and Cho, J. (2009). "Characterizations of Colloidal Organic Matter Isolated from Surface Water." *Sep.Sci.Technol.*, 44(13), 3224.

Le Cornu, P., Faram, M., and Andoh, R. (2000). "A Novel Device for the Removal of Grits and Oils." *CIWEM/AETT Millennium Conference; 'Wastewater Treatment: Standards and Technologies to meet the Challenges of the 21st Century'*, 727-738.

Levenspiel, O. (2012). *Tracer Technology: Modeling the Flow of Fluids*. Springer.

Levenspiel, O. (1999). *Chemical reaction engineering*. New York : Wiley, c1999; 3rd ed.

Libralato, G., Losso, C., Arizzi, N. A., Citron, M., Della, S., Stefano, Zanutto, E., Cepak, F., and Volpi Ghirardini, A. (2008). "Ecotoxicological evaluation of industrial port of Venice (Italy) sediment samples after a decontamination treatment." *Environmental Pollution*, 156(3), 644-650.

Liem, L., Stanley, S., and Smith, D. W. (1999). "Residence time distribution analysis as related to the effective contact time." *Canadian Journal of Civil Engineering*, 26(2), 135-144.

Liscinsky, D. S., True, B., and Holdeman, J. D. (1993). "Experimental Investigation of Crossflow Jet Mixing in a Rectangular Duct." NASA Technical Memorandum 106152, AIAA-93-2037, United States.

Luo, P., Jia, H., Xin, C., Xiang, G., Jiao, Z., and Wu, H. (2013). "An experimental study of liquid mixing in a multi-orifice-impinging transverse jet mixer using PLIF." *Chem.Eng.J.*, 228 554-564.

MacLoughlin, P. F., Malone, M., Murtagh, J. T., and Kieran, P. M. (2000). "The effects of turbulent jet flows on plant cell suspension cultures." *Biotechnology and Bioengineering*, 58(6), 595-604.

Mansour-Geoffrion, M., Dold, P. L., Lamarre, D., Gadbois, A., Deleris, S., and Comeau, Y. (2010). "Characterizing hydrocyclone performance for grit removal from wastewater treatment activated sludge plants." *Minerals Eng*, 23(4), 359-364.

Matvienko, O., and Evtushkin, E. (2007). "Theoretical investigation of the process of cleaning oil-polluted soil in hydrocyclone apparatuses." *Journal of Engineering Physics and Thermophysics*, 80(3), 502-510.

Metcalf, I. N. C., and Eddy, H. (2003). *Wastewater engineering; treatment and reuse*. McGraw-Hill New York.

Morales, L., and Reinhart, D. (1984). "Full-Scale Evaluation of Aerated Grit Chambers." *Journal (Water Pollution Control Federation)*, 56(4), pp. 337-343.

Munoz, A., and Young, S. (2009). "Two-dimensional model for predicting performance of aerated grit chambers." *Canadian Journal of Civil Engineering*, 36(9), 1567-1578.

Nawrocki, M. A. (1974). *A portable device for measuring wastewater flow in sewers*. Office of Research and Development, US Environmental Protection Agency;[for sale by the Supt. of Docs., US Govt. Print. Off.].

Neighbor, J., and Cooper, T. (1965). "Design and Operation Criteria for Aerated Grit Chambers." *Water and Sew. Works*, 112 448.

Oldshu, J. Y. (2004). "Fluid Mixing." *Encyclopedia of Physical Science and Technology*, 79-104.

Osei, K., and Andoh, R. (2008). "Optimal Grit Removal and Control in Collection Systems and at Treatment Plants." ASCE.

Osei, K., Mody, A., and Andoh, R. Y. G. (2010). "Field assessment of grit removal systems." *World Environmental and Water Resources Congress 2010: Challenges of Change, May 16, 2010 - May 20*, American Society of Civil Engineers, Providence, RI, United states, 3756-3763.

Pankajakshan, R., Mitchell, B. J., and Taylor, L. K. (2010). "Simulation of unsteady two-phase flows using a parallel Eulerian–Lagrangian approach." *Comput.Fluids*.

Pedocchi, F., and Piedra-Cueva, I. (2005). "Camp and Stein's Velocity Gradient Formalization." *J.Environ.Eng.*, 131 1369.

Philipossian, A., and Mitchell, E. (2003). "Dispersion number studies in CMP of interlayer dielectric films." *J.Electrochem.Soc.*, 150 G854.

Pignatello, J. J., and Xing, B. (1995). "Mechanisms of slow sorption of organic chemicals to natural particles." *Environ.Sci.Technol.*, 30(1), 1-11.

Pilli, S., Bhunia, P., Yan, S., LeBlanc, R., Tyagi, R., and Surampalli, R. (2011). "Ultrasonic pretreatment of sludge: A review." *Ultrason.Sonochem.*, 18(1), 1-18.

Puprasert, C., Hebrard, G., Lopez, L., and Aurelle, Y. (2004). "Potential of using Hydrocyclone and Hydrocyclone equipped with Grit pot as a pre-treatment in run-off water treatment." *Chemical Engineering and Processing: Process Intensification*, 43(1), 67-83.

Rajaratnam, N. (1976). *Turbulent jets*. Elsevier Science Limited.

Reungoat, D., Riviere, N., and Fauré, J. (2007). "3C PIV and PLIF measurement in turbulent mixing." *Journal of Visualization*, 10(1), 99-110.

- Sandell, D., Macosko, C., and Ranz, W. (1985). "Visualization technique for studying impingement mixing at representative Reynolds numbers." *Polymer Process Engineering*, 3(1-2), 57-70.
- Santos, R. J., and Sultan, M. A. (2013). "State of the art of mini/micro jet reactors." *Chem.Eng.Technol.*, 36(6), 937-949.
- Sarikaya, H. Z. (1992). "Discussion of" Model Study of Jet-Circulated Grit Chamber"." *J. Environ. Eng.*, 118(6).
- Sarimeseli, A., and Kelbaliyev, G. (2004). "Modeling of the break-up of deformable particles in developed turbulent flow." *Chemical Engineering Science*, 59(6), 1233-1240.
- Sawicki, J. M. (2004). "Aerated grit chambers hydraulic design equation." *J. Environ. Eng.*, 130(9), 1050-1058.
- Selomulya, C., Bushell, G., Amal, R., and Waite, T. (2002). "Aggregation mechanisms of latex of different particle sizes in a controlled shear environment." *Langmuir*, 18(6), 1974-1984.
- Sherony, M., and Herrick, P. (2011). "A fresh look at an old problem: Design criteria for effective grit removal." *Journal of New England Water Environment Association*, 45(1), 25-31.
- Soos, M., Moussa, A. S., Ehrl, L., Sefcik, J., Wu, H., and Morbidelli, M. (2008). "Effect of shear rate on aggregate size and morphology investigated under turbulent conditions in stirred tank." *J. Colloid Interface Sci.*, 319(2), 577-589.
- Tchobanoglous, G., Burton, F., and Stensel, H. D. (2003). *Wastewater Engineering: Treatment and Reuse*. McGraw Hill, NY.

- Thirumurthi, D. (1969). "A break-through in the tracer studies of sedimentation tanks." *Journal (Water Pollution Control Federation)*, 41(11), 405-418.
- Tucker, C. L., and Suh, N. P. (1980). "Mixing for reaction injection molding. I. Impingement mixing of liquids." *Polymer Engineering & Science*, 20(13), 875-886.
- Unger, D. R., and Muzzio, F. J. (1999). "Laser- induced fluorescence technique for the quantification of mixing in impinging jets." *AIChE J.*, 45(12), 2477-2486.
- USEPA. (2003). "Wastewater Technology Fact Sheet, Screening and Grit Removal."  
[Http://Water.Epa.Gov/Aboutow/Owm/Upload/2004\\_07\\_07\\_septics\\_final\\_sgrit\\_removal.Pdf](http://Water.Epa.Gov/Aboutow/Owm/Upload/2004_07_07_septics_final_sgrit_removal.Pdf), dated Nov 15, 2011.
- USJDAAF. (1988). "Domestic Wastewater Treatment." *Technical Manual, no. 5-814-3/AFM 88-11, United States Joint Department of the Army and Air Force*, 3.
- Vatistas, G. H., Jawarneh, A. M., and Hong, H. (2005). "Flow characteristics in a vortex chamber." *Can.J.Chem.Eng.*, 83(3), 425-436.
- Von Sperling, M. (2007). *Wastewater characteristics, treatment and disposal*. IWA publishing, .
- Wahl, M. D., Brown, L. C., Soboyejo, A. O., and Dong, B. (2012). "Quantifying the hydraulic performance of treatment wetlands using reliability functions." *Ecol.Eng.*, 47(0), 120-125.
- Wang, J., Zhang, J., Xie, H., Qi, P., Ren, Y., and Hu, Z. (2011). "Methane emissions from a full-scale A/A/O wastewater treatment plant." *Bioresour.Technol.*, 102(9), 5479-5485.

WHO, U. (2015). "Progress on Sanitation and Drinking Water: 2015 Update and MDG Assessment." *Geneva: World Health Organization*, .

Wilson, G. E. (1985). "Is there grit in your sludge?" *Civil Engineering—ASCE*, 55(4), 61-63.

Wilson, G., Tchobanoglous, G., and Griffiths, J. (2007). "The Nitty Gritty." *Water Environ.Technol.*, 19(9), 115-118.

Yoda, M., and Fiedler, H. (1996). "The round jet in a uniform counterflow: flow visualization and mean concentration measurements." *Exp.Fluids*, 21(6), 427-436.

Yuan, Y., and Farnood, R. R. (2010). "Strength and breakage of activated sludge flocs." *Powder Technol*, 199(2), 111-119.

## Tables

Table 3.1: Layouts ( $\Lambda$ ) showing the relative positions of cross jets by circles (open and closed), open circles are mounted on one sidewall and the closed on the opposite sidewall. Arrows are direction of mainstream flow.

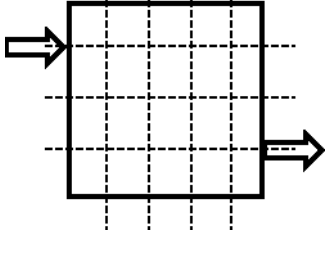
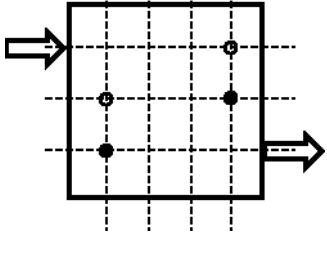
$\Lambda$	Description
A	
B	

Table 3.2: Test scenarios for the PLIF measurements.

Test No.	Layout	Reynolds number	Diameter of a jet (mm)
1	A	0	0
2	B	5500	5.3
3	B	10500	5.3
4	B	16500	5.3
5	B	21000	5.3
6	B	27000	5.3

Table 3.3: Fully mixed concentration,  $C_{fm}$  over the plane and steady state concentration,  $C_{ss}$  at the outlet for different Reynolds numbers.

Test	Layout	Re	$C_{fm}$	$C_{ss}$	$C_{ss}/C_{fm}$
			$\mu\text{g/L}$	$\mu\text{g/L}$	
1	A	0	10.17	14.88	1.46
2	B	5600	9.75	13.39	1.37
3	B	10700	9.54	12.17	1.28
4	B	16700	9.30	11.40	1.23
5	B	20900	9.14	10.58	1.16
6	B	27400	8.87	9.89	1.11

Table 3.4: DCM predictions of plug flow volume,  $V_p$ , mixed flow volume,  $V_m$  and dead flow volume,  $V_d$  using the RTD and PLIF measurements.

Test No.	Layout	Reynolds number	RTD			PLIF		
			$V_p$ (%)	$V_m$ (%)	$V_d$ (%)	$V_p$ (%)	$V_m$ (%)	$V_d$ (%)
1	A	0	18.1	45.3	36.7	18.2	75.8	4.8
2	B	5600	19.5	42.6	37.9	12.5	69.7	16.6
3	B	10700	17.7	45.0	37.3	12.3	64.5	22.0
4	B	16700	15.8	55.5	28.6	8.4	57.8	32.5
5	B	20900	12.8	76.8	10.4	14.1	58.5	26.2
6	B	27400	13.7	77.0	9.2	22.4	75.5	0.9

## Figures

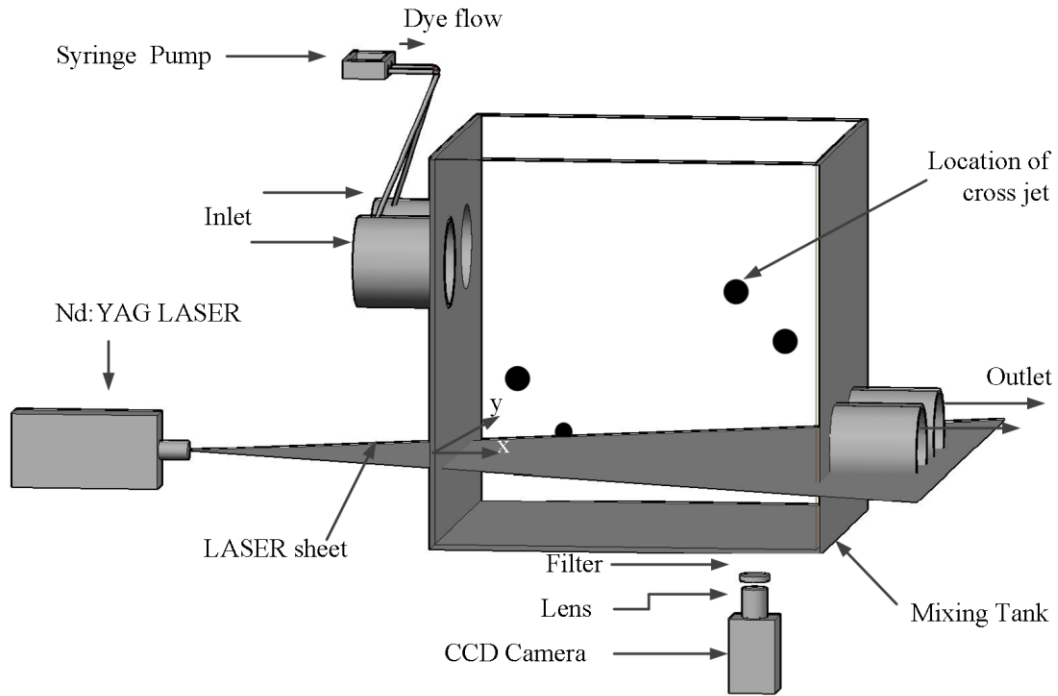


Fig. 25: A schematic diagram of PLIF setup showing a laser sheet, positions of laser and camera, and directions of mainstream flows and locations of cross jets.

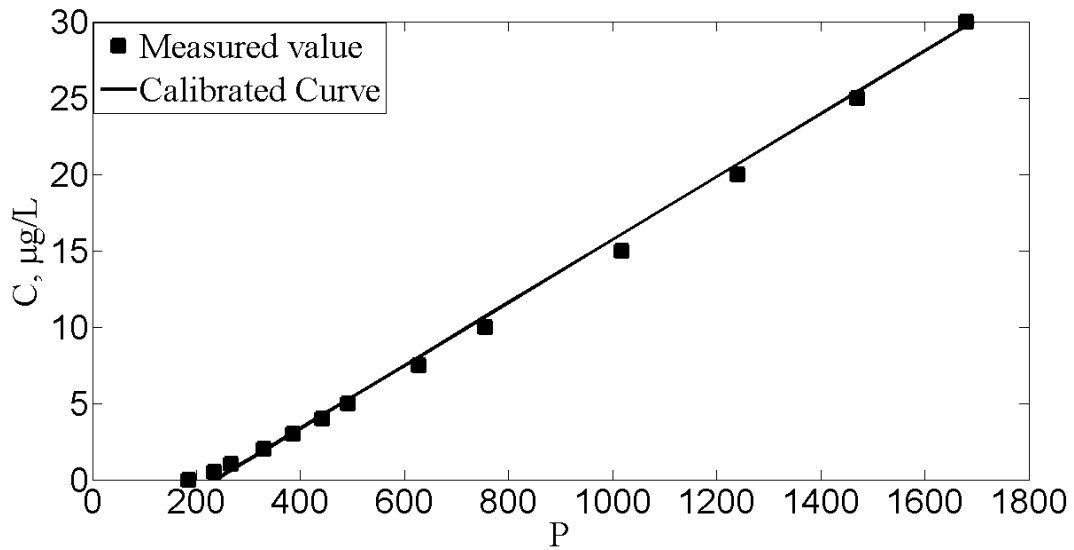


Fig. 26: Concentration of fluorescent dye Rhodamine 6G,  $C$  ( $\mu\text{g/L}$ ) versus pixel intensity,  $P$ , measured at laser energy of 120 mJ(100%); The  $R^2$  value of the calibration curve is 0.980.

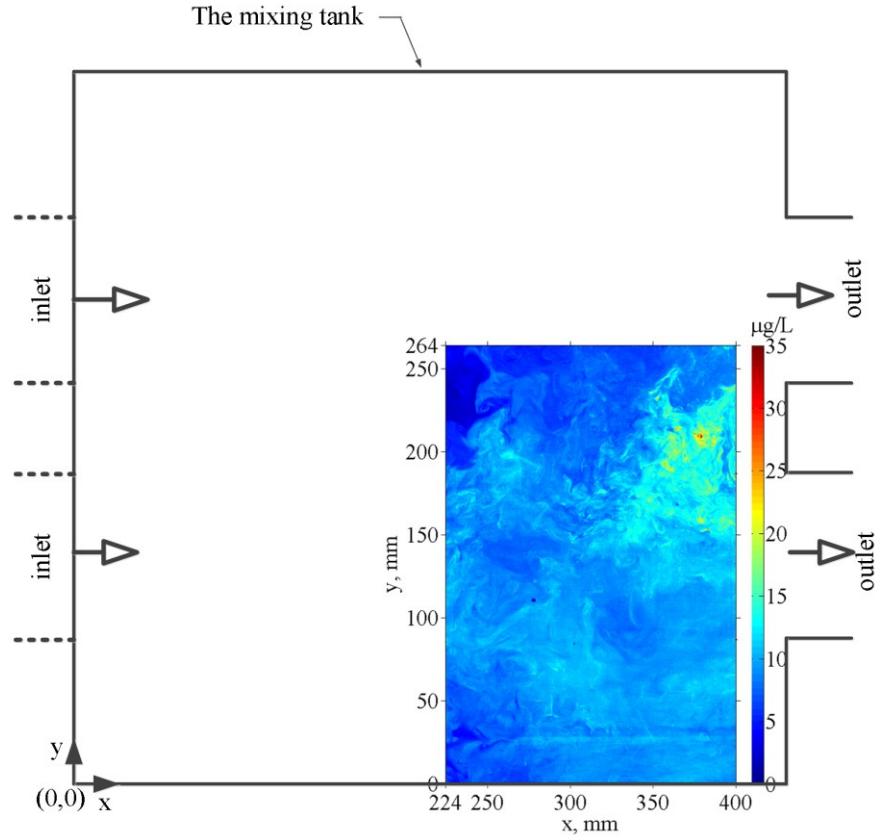


Fig. 27: Position of field of view in the tank and Instantaneous concentration map, measured at  $t/\tau = 1.0$  in an experiment with Layout = B, Reynolds number = 10765 and diameter of a jet = 5.3 mm, where  $t$  = time and  $\tau$  = mean residence time.

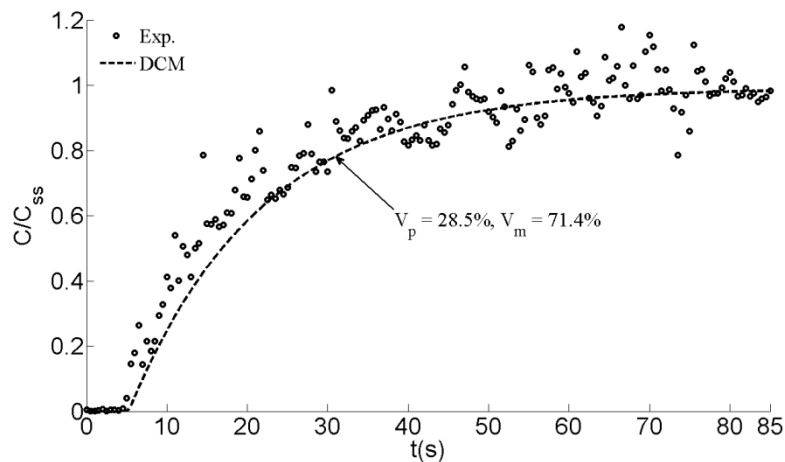


Fig. 28: Time series plot of  $C/C_{ss}$  where  $C$  = concentration of tracer and  $C_{ss}$  = steady state concentration defined as the average concentration from  $t = 65$  to  $85$  sec at outlet. Solid line is model F-curve by Dispersive Compartmental Model (DCM), and dots are experimental values of F-curve. [Layout = B, diameter of jet = 5.3mm and Reynolds number = 27353].

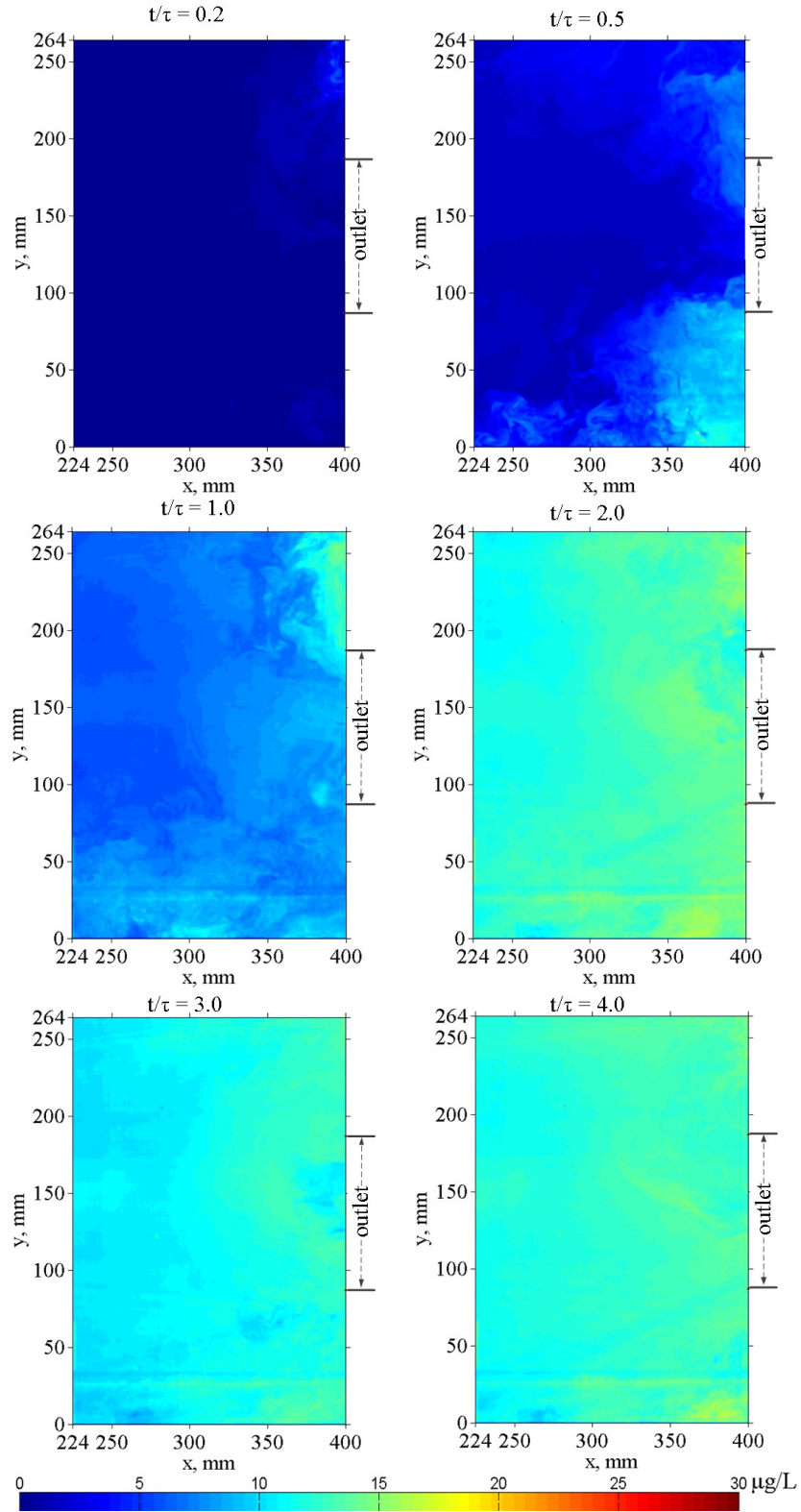


Fig. 29: Instantaneous concentration maps at  $t/\tau = 0.2, 0.5, 1.0, 2.0, 3.0$  and  $4.0$  of a PLIF experiment with Layout A (no jets).

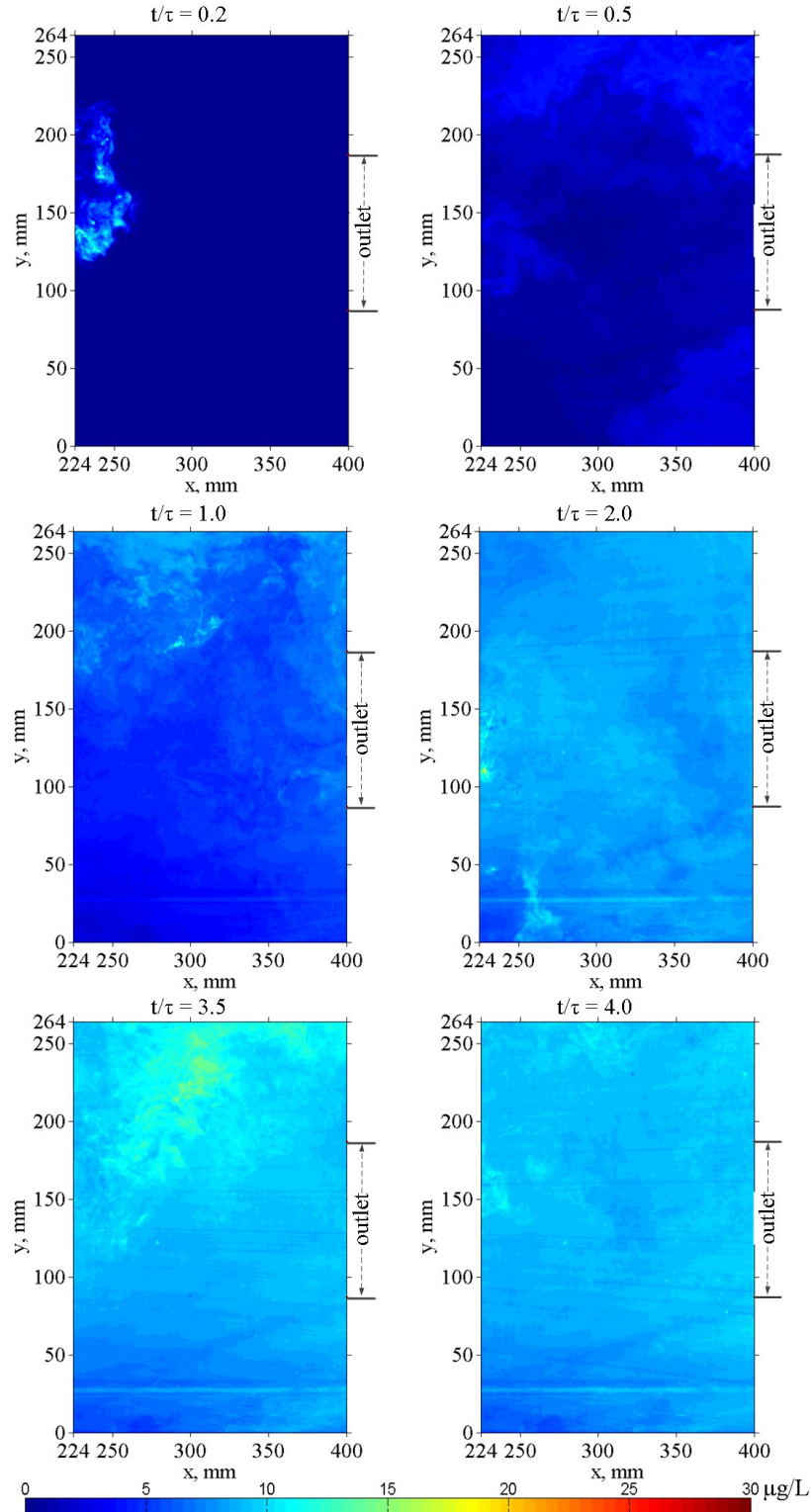


Fig. 30: Instantaneous concentration maps at  $t/\tau = 0.2, 0.5, 1.0, 2.0, 3.0$  and  $4.0$  of a PLIF experiment with Layout B, Reynolds number of 27378 and jet-diameter of 5.3mm.

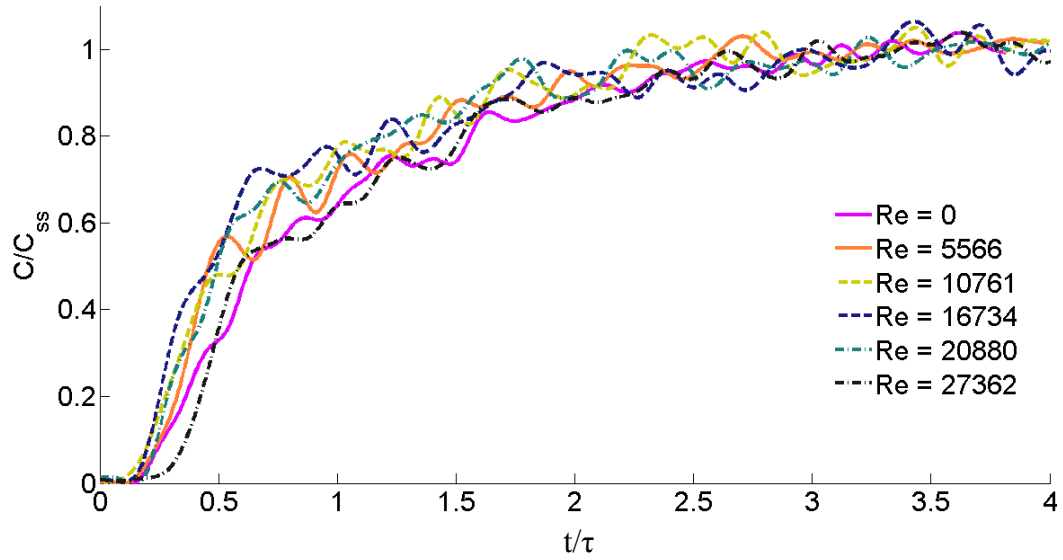


Fig. 31: Time series of dimensionless outlet concentration  $C/C_{ss}$  for varying Reynolds number,  $Re$ .  $C_{ss}$  is steady state concentration and  $\tau$  is residence time . [Layout A for  $Re = 0$  , and Layout B, and diameter of jets of 5.3 mm for all other  $Re$ ]

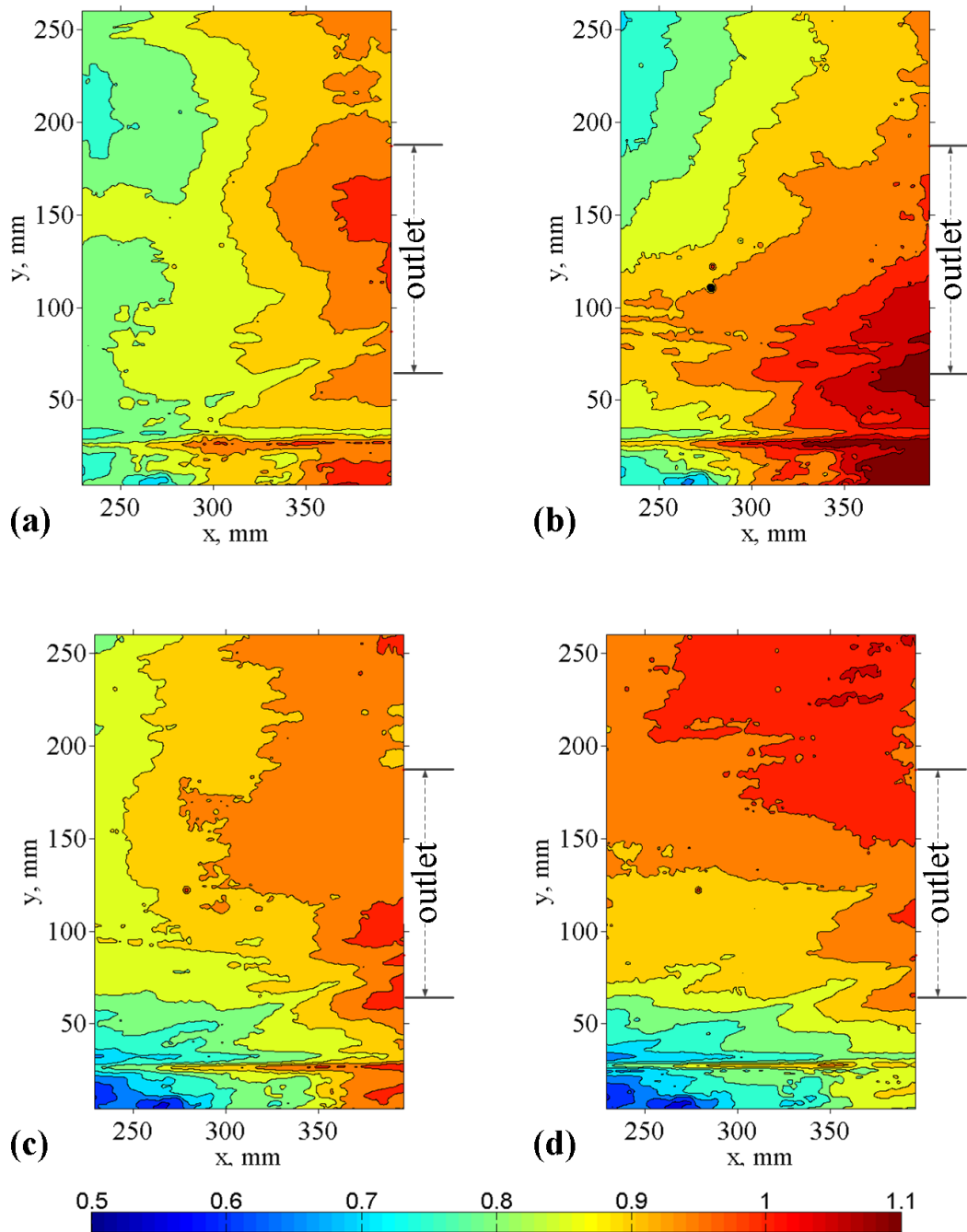


Fig. 32: Dimensionless concentration  $C_{ss}/C_{sso}$ , where  $C_{ss}$  is average steady state concentration for the period of 65 to 85 sec, and  $C_{sso}$  is the average concentration at outlet for Reynolds number (a)  $Re = 0$ , (b)  $Re = 10700$ , (c)  $Re = 16700$  and (d)  $Re = 27400$ . Diameter of jets was 5.3mm.

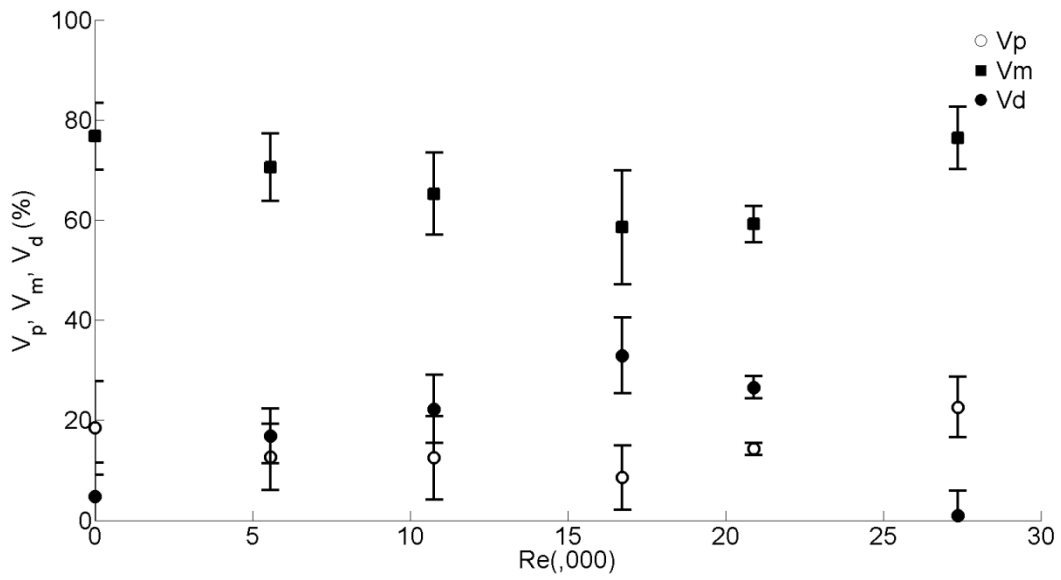


Fig. 33: Percentage of mixed flow volume,  $V_m$ , plug flow volume,  $V_p$  and dead flow volume,  $V_d$  for varying Reynolds number, estimated by DCM.

## **Chapter 4 : Field Assessment of a Model Grit Removal System at Gold Bar Wastewater Treatment Plant, Edmonton<sup>2</sup>**

---

### **4.1 Introduction**

Grit removal system is a preliminary treatment unit in a wastewater treatment plant (WWTP) for removing 210 $\mu$ m and larger particles (Metcalf and Eddy 2003). Modern grit removal systems, such as aerated grit tank, have a single tank for generating two flow zones (Gruber et al. 1988). These are a strong spiral flow zone for separating organic materials, mostly fat, oil and grease (FOG) from grit and a quiescent flow zone for settling grit particles. The spiral flow zone is generated by transverse air jets to the longitudinal section of the tank, and the quiescent flow zone is produced at another flow zone by maintaining a control velocity of water at 0.3 m/s for settling grit particles (Hendricks 2006). A complex curvilinear cross section is required to generate spiral flow that is difficult to construct and design (Munoz and Young 2009). There is a lack of knowledge on the functional relationship among the design factors, such as position, number and flow rate of air jets, as well as the position and size of baffles (Sawicki 2004). The cost of operating air jets is high because of compressing and injection into water (Anderson and Holmberg 2006). Therefore, generating these two flow zones in one tank is the preliminary cause for the difficulties, complexities of design, and high operating costs. An attempt to reduce the cost was proposed by Brenner and Diskin (1991) who used water jets to replace air jets. However, the complexities of design and operation were not solved. For solving the complexities, a new grit removal technique was developed by considering two separate tanks for two opposite flow zones and by using water jets for reducing the cost. In this study, the performance of the new system was evaluated by demonstrating field experiments for readiness of this technique.

---

<sup>2</sup> A version of this chapter was submitted to Journal of Environmental Management

Demonstrating a new model in the field is a step towards the readiness of a technology. The new technology of grit removal system comprised of a mixing tank for generating turbulent flow zone for separating FOG and grit, and a rectangular grit tank for generating the control velocity for settling grit and floating FOG. Reports on the field assessments for readiness of grit removal units are limited in the literature. Most of the studies have conducted on the hydraulic performance of the existing grit removal units. For example, Morales and Reinhart (1984) evaluated five running aerated grit tanks for ranking their performance. The performance was evaluated by studying hydraulic flow only; no grit measurements were taken into consideration. Because of maintenance requirement, Finger and Parrick (1980) investigated the grit characteristics from a grit removal system for solving problems of inefficiency and ineffectiveness. The measurements were total solid, volatile solid, and sieve analysis of grit. These studies were part of routine maintenance works, not for testing the system for readiness. However, two new grit removal systems were evaluated prior to installation, whereas the systems were built at a prototype. Osei et al. (2010) carried out the field performance of the two commercial grit removal units. The performance was evaluated by measuring the concentration of grit in influent water and effluent water and characterizing grit size captured in the systems. In case of a model-scale grit removal system, the challenges, uncertainties and measurement methods are not well known for evaluating the performance of the system. It is important to evaluate the mixing performance of a small-scale grit tank based on the methods of performance studies of full-scale grit tanks. The investigation would enhance the deep understanding of the system for its readiness as a new technique for grit removal systems.

The proposed grit removal system was built on a small scale. The grit tank was a 1:15 scaled down model of an aerated grit tank at the Gold Bar Wastewater Treatment Plant (GBWWTP), Edmonton. The width of the model grit tank was followed to develop the mixing tank, which was 43 cm x 43 cm square in plan.

The flow of the prototype grit tank was scaled down for the longitudinal flow of the model grit removal system by the Froude number similarity. The transverse flow by water jets was experimented in a prior tracer study (Chapter 2) to produce maximum mixed flow volume in the mixing tank. The transverse flow for the pilot scale mixing tank was proposed to develop by similarities of Kolmogorov scale of turbulence to grit size. The turbulent flow zone for cleaning grit was generated in the mixing tank based on the best configuration of jets in the prior study. Based on the results of the study, operating condition was improved so that a strong turbulent flow was generated in the mixing tank. Reynolds number was increased to improve the operating condition. It was hypothesized that the water jets with the best configuration and increased Reynolds number were able to clean grit particles in the mixing tank that led to the improvement of the grit removal system. Therefore, the performance of the mixing tank was evaluated with and without applying water jets. The difference in the grit removal under these two conditions was the effect of the water jets. The objectives of the study were measurements of grit concentration at inflow and outflow of the system, estimation of FOG-scum on water surface, and characterization of grit captured in the system. The characterization included the sieve analysis and measuring volatile component on the grit particles. The measurement of the grit concentrations was used to determine the grit removal efficiency of the system. The estimation of the FOG-scum was used to determine the cleaning performance of the mixing tank. Design diameter of grit was possible determined from the sieve analysis of the captured grit. The study was important, as the successful performance of the mixing tank would lead to a breakthrough solution of grit removal units.

#### **4.2 Experimental Setup and Method**

The model-grit removal system consisted of two tanks: a grit tank and a mixing tank. Fig. 34 shows a complete setup; a constant head tank was set for keeping a steady flow rate along the longitudinal direction of the tanks, which is the

longitudinal flow. Transverse flow ran through the transverse jets, which were mounted on each of the sidewalls. Intake of the longitudinal flow was the water source from the aerated grit tank of GBWWTP. The intake position was 1.5 ft away from the inlet of the aerated tank and at 5 ft depth from the top of 15 ft deep water. This intake position was selected, because water at this location was well-mixed and fine grit particles were expected. Fine grit was expected in the feed water to avoid sediment settlement in the mixing tank, because the average velocity in the mixing tank was 2 cm/s. It is noted that the model was built at 1/15<sup>th</sup> scale of a full size aerated tank of GBWWTP, and detail dimensions of the tanks were presented in Chapter 2. The water velocity at this intake position was low to ensure the stability of a submergible pump. A submergible sewage pump was set at the intake position to pump wastewater from the water source to the constant head tank. Water flow from the intake to the constant head tank was controlled by a valve. The flow from the constant head tank to the tanks was longitudinal flow, which was measured by a magnetic flow meter (MAG2IC-050PA1LSDAAAT2-XX-X, FoxBoro, Japan). The flow, which was the transverse flow running through the jets, was set up from a fresh water source at GBWWTP. The pressure of the fresh water source was large enough to supply water to the jet-nozzles through the manifold. A valve was used to control the flow rate. Another flow meter (IMT25-SEATB10K-BG, FoxBoro, China) was used to measure this transverse flow rate.

Experiments were carried out with two layouts of jets: layout A and H as shown in Table 4.1. Layout A was set up for control measurement. Layout H was a configuration of jets that produced maximum mixing in the square tank at Reynolds number of 27300. It is noted that the nomenclature of the layouts was kept consistent with that of layouts in Chapter 2. In the results of Chapter 2, the mixing performance was increased for higher Reynolds numbers, although the tests were limited to Reynolds number of 27300. Based on this result, Reynolds number was increased to 41600, which produced energetic turbulent flows and

maximum mixing in the square tank. The layout H and Reynolds number of 41600 were selected as jet parameters for testing the grit cleaning performance of the square tank. Two test cases were planned as shown in Table 4.2, where each test was repeated three times for decreasing statistical uncertainty.

Field measurements were involved in determining solid concentration at several location of the system. The samples for influent solid concentrations were taken from the constant head tank, while the samples for effluent concentrations were taken from inside of the system outlets. Water samples from these locations were collected for comparing the influent and outlet concentrations at two experimental conditions: without and with transverse jets. Solid samples were collected from the bottom and top surfaces of the grit tank. These samples were used for the measurement of fixed and volatile components to understand the gravity separation of heavy (fixed components) and light materials (volatile components). Water samples from the inlet and outlet were taken at each 30 mins after establishing a steady flow throughout. Each experimental run was carried out for 4 hours, which was long enough for collecting a good number of discrete water samples. The 250 mL plastic bottles were used for water samples and the bottles were kept in coolers before refrigerating in to the laboratory. These samples were required for measuring the solid concentrations of influent and effluent water. The solid samples at the bottom and top surfaces of three sections were taken at each hour. These samples were required for measuring the fraction of fixed and volatile components at these locations. At the end of each run, water was emptied by using syphons and the solid deposit was collected from the floor of the grit tank. The solid deposit was used for analyzing grit sizes captured on the grit floor. Settleable grit was measured by Imhoff settling cone for understanding grit settlement at influent and effluent water for conditions with and without jets. Three water samples of 2L each was collected for measuring the settleable grit. All of the samples were kept in a cold room in the environmental laboratory at the University of Alberta.

The measurements of water samples were concentrations of total solid (TS), total suspended solid (TSS), total fixed solid (TFS), total volatile solid (TVS), fixed suspended solid (FSS), and volatile suspended solid (VSS). Standard method 2540(B,D,E) was followed to determine these measurements for each water sample (AWWA 1998). A water sample of 100 mL was first evaporated at 105<sup>0</sup>C, and the residual was the mass of TS of that volume of water sample. The solid was burned at 550<sup>0</sup>C, the residual was the mass of TFS of the water. TVS was determined by subtracting TFS from TS. A 50 mL water sample was filtered through a 2 µm Millipore glass filter (thickness 1200 µm, made in USA). The residual on the filter was evaporated at 105<sup>0</sup>C and burned at 550<sup>0</sup>C to determine TSS, FSS and VSS in the similar way of determining TS, TFS and TVS. The same method of evaporation at 105<sup>0</sup>C and burning at 550<sup>0</sup>C was followed for solid samples, which were collected from the top surface of water and from the bottom of the grit tank.

The measurements of grit were settleable grit, percentages of fixed and volatile component in grit and scum material at the grit tank, and sieve analyses of the grit particles. First, the settling of grit particles was empirically measured by Imhoff settling-cone to estimate the amount of settleable grit in influent water and effluent water. The measurements were useful to understand the action of transverse jets in cleaning and consequently settling at the grit tank. Three Imhoff cones were used for three samples of each test. Standard method 2405F was followed to determine the amount of settling grit in mL/L (AWWA 1998). Fig. 35 shows the arrangement of the measurement with Imhoff cones. Settled grit shown in dark color was separated after the experiments. Next, the effect of gravity separation was studied by measuring the fraction of fixed and volatile components of the solid material grabbed from scum material of top surface and grit material of the bottom layer of the grit tank. The measurements of TS, TFS and TVS were carried out for these solid samples by following the standard method 2405B (AWWA 1998). Samples were evaporated at 105<sup>0</sup>C and burned at

550<sup>0</sup>C; and volatile and fixed solids were measured. Then, sieve analyses were conducted with the grit sludge collected from the grit tank. The grit sludge was washed several times in a one meter long settling tube. Fig. 36 shows two conditions of grit wash of two test samples. Volatile materials were separated from settleable grit after 45 mins of settling time. The volatile materials were taken out from the tube and clean water was poured for another wash. These steps were followed several times until no volatile sludge was observed floating in the tube. Settled grit was evaporated initially to reduce the amount of water and burned at 550<sup>0</sup>C for 15 mins to obtain fixed components. Grit was separated from the fixed components by blowing ash of volatile components. Sieve analysis of the grit of each test was carried out by following ASTM D422; ASTM stands for American Society for Testing and Materials (American Society for Testing and Materials 2000).

### **4.3 Analysis**

The difference of concentrations at influent and effluent water led to understand the effect of square tank with transverse jets. The difference in the total solids was the sign of grit removal in the tank. The difference in the suspended solid concentration was the confirmation of the grit deposition and FOG flotation in the grit tank. Differences of FSS and VSS, which are the components of TSS, were computed to determine the percentage of these components removed. The strength of the difference was determined by tests of statistical significance. All values of TSS, FSS and VSS at inlet and outlet were used for the statistical significant tests, where p-values were determined to estimate the strength of the difference.

The effect of grit cleaning was evaluated from the measurements of FSS, VSS, TSS and the fractions of volatile and fixed components of the solid samples. Total amount of solid, which was remained in the grit tank, was the difference of TSS at inlet and at outlet. The removal efficiencies of TSS, FSS and VSS were determined by following Eq. (4.1) to (4.3), where terms in [ ] are the

concentrations, and subscript “i” stands for influent concentration and “e” stands for effluent concentration.

$$\eta_{TSS} = \frac{[TSS]_i - [TSS]_e}{[TSS]_i} \quad (4.1)$$

$$\eta_{VSS} = \frac{[VSS]_i - [VSS]_e}{[VSS]_i} \quad (4.2)$$

$$\eta_{FSS} = \frac{[FSS]_i - [FSS]_e}{[FSS]_i} \quad (4.3)$$

The difference of VSS between inlet and outlet was the amount of volatile components, which were partly floated on water surface and settled with grit on the bottom of the tank. The total fraction of volatile components ( $f_{VS}$ ) was determined by the following equation,

$$f_{VS} = \frac{[VSS]_i - [VSS]_e}{[TSS]_i - [TSS]_e} \quad (4.4)$$

Similarly, the fraction of fixed components ( $f_{FS}$ ) of total suspended solid was determined by the following equation,

$$f_{FS} = \frac{[FSS]_i - [FSS]_e}{[TSS]_i - [TSS]_e} \quad (4.5)$$

The fraction of volatile material in scum and grit were determined by using the values of TS and TVS of these solid samples. Similarly, the values of TS and TFS of grit and scum samples were used to determine the fractions of fixed material in scum and grit. The fractions of solid phase and water phase were used to estimate amount of scum removed and grit deposit at the bottom of the tank.

Deposited grit materials were processed for sieve analysis. The sieve analysis was plotted for general understanding of the grit size distribution. The size distribution was used to determine the smallest particle size, which was removed 95% by this new grit removal system. Other sizes of particles, which were diameters of 10% ( $D_{10}$ ), 30% ( $D_{30}$ ), 50% ( $D_{50}$ ) and 60% ( $D_{60}$ ) finer particles, were determined.

These diameters were used to compute uniformity coefficient,  $C_u$  defined in Eq. (4.1) and the coefficient of curvatures,  $C_c$  defined in Eq. (4.2). These parameters are important to understand the grit characteristics and for potential uses in the landfills.

$$C_c = \frac{D_{60}}{D_{10}} \quad (4.6)$$

$$C_u = \frac{(D_{30})^2}{D_{10}D_{60}} \quad (4.7)$$

## 4.4 Results

### 4.4.1 Removal of TS and TSS

The effectiveness of transverse jets in cleaning grit particles was evaluated based on the solid concentrations. The concentrations of TFS and TVS at inlet and outlet are shown in Fig. 37 for the six tests. Each bar is the concentration of total solid in the plots. The error bars are the standard error of the samples. The standard errors of TFS varied from 0.03 mg/L to 0.15 mg/L, and those of TVS varied from 0.01 mg/L to 0.10 mg/L. These values were very small for the measured values of the TFS and TVS. The values of TS of all tests except E3 and E5, were close to the average values of total solid measured by Habib (2008) at GBWWTP, which was 972 mg/L. It is noted that typical value of TS of raw water to a grit removal tank varies from 350 mg/L to 1400 mg/L (Spellman, 2013). However, the high values of TS at E3 and E5 were reasonable because the highest value of TS was 2.3 times of its average value at GBWWTP (El-Din and Smith 2002). The high TS values measured in this study may be due to 17.9 mm precipitation occurred two days before the experiments. Note that the experiments were conducted between August 8 to August 11, 2014.

The inlet and outlet solid concentrations were compared, and there was not significant difference between TS of inlet and of outlet in the tests without jets as

shown in Fig. 4.4. The concentrations of TFS and TVS were also unchanged at these tests. The average of the difference of total solid concentrations was less than 1% of the inlet concentration. The model grit was not long and deep enough to settle grit of the raw wastewater without any cleaning at the mixing tank. The average difference of TS varied from 13% to 26.6% in the tests with transverse jets. In these tests, the concentration of TFS was reduced at the outlet by 17.4% and that of TVS was reduced by 21.6%. These reductions of solid at the outlet show the strong effect of transverse jets on cleaning grit in the square tank.

The effect of grit cleaning was directly influence on the differences of suspended solids between inlet and outlet. The components of suspended solids, FSS and VSS, are shown in Fig. 38. Each bar of the plots is the value of TSS. The error bars are the standard error of the samples. The values of TSS were close to the values reported previously. Habib (2008) measured TSS levels of 237 mg/L at influent of GBWWTP in spring 2008, while average TSS values of 286 mg/L were recorded at GBWWTP from June to August in 2014 (EPCOR Water Services, 2015). Fig. 5 shows no statistically significant difference between the inlet and outlet concentrations of TSS, FSS and VSS in the tests without jets that is consistent with the results of total solid concentrations.

The test of statistical significance for the difference was conducted and the parameters are shown in Table 4.3. The degrees of freedom for the first test E0 was 12, which was 18 for other tests, because of the loss of six samples during the experiment in test E0. The mean values in the table are the average values of TSS, FSS and VSS at the inlet. The table shows that the p-values were larger than 0.05 for TSS, FSS and VSS in the tests without jets. That indicates that the outlet concentrations of TSS, FSS and VSS were not significantly difference with the inlet concentrations of these solids. This clearly proved that no significant grit was removed in this tank, because grit was not cleaned in the square tank. However, the p-values are smaller than 0.05 for TSS, FSS and VSS in the tests with transverse jets. That signified that the outlet concentrations of TSS, FSS and

VSS were significantly different from the inlet concentrations. The outlet concentrations of TSS, FSS and VSS were reduced from the inlet concentrations with various ranges shown in the table. On average, TSS was reduced by 28.2%, FSS by 41.5% and VSS by 26.0%. The significant reduction of FSS and VSS indicated that the grit was cleaned in the square tank by the effect of transverse jets. Therefore, the heavy grit particles were settled on tank floor and light FOG was floated to the top water level of the grit tank.

#### **4.4.2 Removal of Grit and FOG**

The amount of grit deposit and FOG scum were evaluated for the tests with jets, as there was a significant difference of TSS, FSS and VSS between inlet and outlet. The difference of TSS at inlet and outlet was the amount of grit and scum remained in the grit tank. The fractions of VSS and FSS, which were remained in the grit tank, were 815 mg and 185 mg per gram of TSS, respectively. Materials of VSS and FSS that remained in the tank were partly observed on water surface as a thin scum layer, and at the bottom of grit tank as grit deposit. In these solid samples, the measured fractions of volatile and fixed materials were tabulated in Table 4.4, where these fractions of water phase are also shown. Table 4.4 shows that the fraction of volatile solid in the scum layer was larger than the volatile fraction in the grit material in each test. On average, volatile solid was 738 mg/g of total solid of scum, whereas volatile solid was 443 mg/g of total solid of grit material. The fixed solid was only 26.2% of scum solid, which is very small. This indicated that fixed solids, being cleaned in the mixing tank, were settled at the bottom. However, the fixed solid was 55.7% and volatile solid was 44.3% of the grit material. The percentage of volatile solid was very high and the grit could be classified as sloppy and highly odorous (Neighbor and Cooper 1965). This percentage of volatile content in grit was reasonable as the extreme value of volatile solid was found as 50% of grit (Habib 2008). Typically, the volatile content varies from 3.7% to 25.4% in the grit at GBWWTP (EWMCoE, 2012). It has been reported that the grit composition is highly variable, with a volatile

content from 1% to 56% (Tchobanoglous et al., 2003; Hendricks, 2006). However, the volatile content varies from 3.7% to 25.4% in the grit of GBWWTP (EWMCoe, 2012). The reason of high percentage volatile contents in grit was that the feed water contained 84% of TSS as volatile material (VSS). This high percentage of VSS produced sloppy grit deposit, which was observed during the grit wash for sieve analysis as shown in Fig. 36.

Fig. 39 shows the scum layer of VSS, which was accumulated on the water surface. The measured length of the scum layer was  $43 \times 50 \text{ cm}^2$ . At the exit end, not shown in the figure, the scum layer was small, which was  $43 \times 30 \text{ cm}^2$ . The scum was spilled because of small freeboard (2.5 cm only), and the spill was observed almost in each hour. Accumulated volatile material was estimated for an hour based on the difference of VSS at inlet and at outlet, which was 75.4 mg/L. A large part of these volatile materials was accumulated at the scum layer, which was 63% of 75.4 mg/L. This percentage value was used as a first approximate, which was the fraction of volatile components relative to the total volatile material in the grit tank. These approximations were used to estimate the thickness of scum layer, which was 2.75 mm. Specific gravity of scum, which is  $950 \text{ mg/cm}^3$  was used in this calculation (Fouad et al. 2014). The estimated thickness was reasonable because the measured thickness of scum is found as 6.25 mm in wastewater flow (Nawrocki 1974).

The amount of grit was calculated based on the measurements of FSS at inlet and outlet. The average difference of FSS was 18.5 mg/L, where 68% of the fixed solid was deposited at the bottom. The percentage value was the fraction of fixed components relative to the total fixed components in the grit tank. The calculated amount based on the measured FSS was 625 g, which was reasonably close to the field measurement of grit. In the field, the amount of grit at the bottom of the tank was approximately one kg. The grit removal capacity of this new technique was determined based on the measured FSS and flow rate. Table 4.5 shows the calculation of this grit removal system and the existing capacity of GBWWTP

(EWM, 2012). The new grit removal system can separate 3.4 tons grit per day based on the capacity of GBWWTP, which is 1600 million liter per day. The present capacity of GBWWTP is 600 to 700 tons per year, which is equivalent to 1.78 tons per day. The new system can remove 88% extra grit than the existing capacity of GBWWTP.

#### **4.4.3 Grit Characteristics**

Settleability of grit particles, measured by Imhoff settling experiment, is shown in Fig. 39. The error bars in the plot are the standard error of the samples. The plot shows that there is no difference between the settleable solid of inlet and outlet for the tests without jets. The difference was observed significantly in the tests with transverse jets. The average difference was 5.8% of inlet settleable solid for the tests without jets. For the tests with jets, the average difference was 48.5%, which indicates that large amount of grit was settled in the grit tank. The results of the Imhoff cone experiments were also supportive evidence for the case that transverse jets were able to clean grit particles, because the settleable grit was reduced significantly at the outlet in the tests with jets.

The characteristics of grit particles were observed by conducting the sieve analysis. Fig. 40 shows the particle size distribution of the grit collected from the tank floor and of the grit collected by EWMCoE (2012) and Habib (2008). The sample of the first experiment, E0 was not included in the figure as the sample was destroyed during the experimental process. All size distribution curves are for the grit collected in the month of August in different years at GBWWTP. The grit samples of EWMCoE (2012) and Habib (2008) were collected from the removed grit deposit of the aerated grit tank. The curves, E1, E3 and E5 are shown at further right to the curves, E2 and E4. These curves (E1, E3 and E5) are shown at very further right to the curves of EWMCoE (2012) and Habib (2008). That means that finer particles were settled in the tests with jets than the tests without jets. The curves G1, G2, G3 and H1 show that the aerated grit tanks of GBWWTP are not able to remove particles finer than to 210  $\mu\text{m}$  that satisfies the design

criterion of a grit removal system (Metcalf and Eddy 2003). However, this criterion is not enough for advanced treatment units of WWTP (Keane and deSilva 2009).

The effect of the jets was observed in settling finer particles. The sizes of the particles were examined to understand the deposited grit by the effect of the transverse jets. Table 4.6 shows the values of  $D_{10}$ ,  $D_{30}$ ,  $D_{50}$  and  $D_{60}$ , and  $C_c$  and  $C_u$  from the tests with the jets. The values of these diameters for the tests without jets were not included in the Table as there was no effect of the jets on the deposited grit. Table 4.6 also shows the values of these parameters obtained by Habib (Habib 2008) and EWMCoE (2012). Their data were obtained from the raw grit deposit from the grit tanks of the GBWWTP. The values of  $C_c$  and  $C_u$  of GBWWTP were consistent with the values of the tests of E3 and E5, and a little inconsistency was observed in the test of E1, which shows very lower values of diameters. The values of  $C_u$  were less than three, and that indicated that the grit was homogeneous. The values of  $C_c$  were close to one, and that indicated that the grit was poorly graded (Chen et al., 2014). The values of  $C_c$  and  $C_u$  could be increased by adding more grit of larger sizes so that the grit could be used as filter media and embankment materials (Dayal and Sinha, 2005).

Based on the results on the diameters, it was evident that transverse jets were effective in cleaning grit that resulted in the deposition of very fine particles. The values of  $D_{10}$  of grit deposited in GBWWTP were larger than the values of  $D_{10}$  obtained in the tests, E1, E3 and E5. That means, the new technique by the transverse jets performed better than the existing grit removal system in GBWWTP. The new grit removal system was dimensionally scaled down so that grit particles removed in the new system and the grit tanks of GBWWTP were comparable. Table 4.6 shows that this new technique was able to settle particles finer than  $100 \mu\text{m}$  (as  $D_{10} < 100 \mu\text{m}$ ). This achievement of removing very finer particle would lead to improve downstream treatment units, such as membrane filtration plants (Andoh and Neumayer 2009).

#### **4.4.4 Significance of the New Grit Removal System**

This new system was able to remove 95% of 44  $\mu\text{m}$  and larger particles. This was the highest achievement in removing fine particles compared to the removal achieved using commercial grit removal systems (De Silva and Bates, 2004; Andoh and Neumayer, 2009). Typically, aerated grit chambers are designed for 95% removal of grit with diameters larger than 200  $\mu\text{m}$ , with an increasing trend to achieve 95% removal of particles larger than 100  $\mu\text{m}$  (Munoz and Young, 2009). Now, this new technique is ready for further testing in a large scale for potential commercial uses in WWTPs.

The new system was able to settle a large amount of grit with fine particles and to float FOG as scum. The possible amount of grit deposit was 3.4 tons per day based on the average treatment capacity of GBWWTP. This amount of grit deposit is larger than the existing capacity of grit removed from GBWWTP that is close to 2 tons per day (GBWWTP, 2012).

The added advantage of the new technique is the extraction of FOG, which would have potential use as biofuel. FOG is susceptible to hydrolysis because of its inherent high moisture content and the presence of lipases, making suitable for biofuel production (Montefrio et al., 2010; Pastore et al., 2015). Anaerobic codigestion of municipal FOG has been used for methane recovery (Kabouris et al., 2009). FOG is not extracted from the conventional grit removal units (Von Sperling, 2007), whereas this new grit removal system has a potential for early removal of FOG. The amount of FOG was large in the experiments because the source of feed water contained very fine particles and a high percentage of volatile material.

#### **4.4.5 Scale Effects**

The model mixing tank was proposed to scale up by similarity of shear stresses at Kolmogorov scale. This similarity of the shear stresses leads grit particles undergoing to same shear stresses in the model and the prototype, therefore,

$$\tau_m = \tau_p \quad (4.8)$$

where,  $\tau_m$  is shear stress at the Kolmogorov scale in the model, and  $\tau_p$  is shear stress at the Kolmogorov scale in the prototype. Shear stress at this scale is expressed as follows:

$$\tau = \mu \frac{u_k}{\eta_k} \quad (4.9)$$

where,  $\mu$  is the dynamic viscosity of water,  $u_k$  is the velocity and  $\eta_k$  is the length of eddies at the Kolmogorov scale. Kolmogorov (1941) defined the velocity and length scale of eddies as:

$$u_k = (\varepsilon \nu)^{1/4} \quad (4.10)$$

$$\eta_k = \left( \frac{\nu^3}{\varepsilon} \right)^{1/4} \quad (4.11)$$

where,  $\nu$  is the kinematic viscosity of water, and  $\varepsilon$  is the rate of dissipation of turbulent kinetic energy per unit mass at that scale. Using Eqs. (4.10) and (4.11) in Eq. (4.8), the expression of shear stresses can be stated as follows:

$$\tau = \mu \left( \frac{\varepsilon}{\nu} \right)^{1/2} \quad (4.12)$$

The viscosity of water will be approximately equal in the model and prototype, therefore, Eq. (4.12) predicts that the energy dissipation rate will also be equal in the model and prototype (i.e.  $\varepsilon_m = \varepsilon_f$ ).

The energy dissipation rates are related to turbulent velocity,  $u'$  and length of the large scale eddies,  $l$ , which is expressed as follows:

$$\varepsilon = \frac{u'^3}{l} \quad (4.13)$$

This length scale,  $l$  is related to geometric length scale of the tanks; therefore, the following relationship can be established:

$$\frac{l_p}{l_m} \sim \frac{L_p}{L_m} \quad (4.14)$$

where,  $L_p$  is the length scale of the prototype and  $L_m$  is the length scale of the model. For a circular jet, value of  $u'$  proportionally varies with the velocity ( $U_s$ ) at the centerline of a circular jet (Tennekes and Lumley 1972). Rajaratnam (1972) expressed the relationship between  $U_s$  and inlet velocity of jet ( $U_0$ ) that led to establish the following relationships:

$$\frac{u'_p}{u'_m} \sim \frac{U_{s,p}}{U_{s,m}} \sim \frac{U_{0,p}}{U_{0,m}} \quad (4.15)$$

where,  $u'$  is the turbulent velocity,  $U_s$  is the centerline velocity of jets and  $U_0$  is inlet velocity of the jets. The subscripts,  $m$  and  $p$  in notations refer to the model and prototype scales. The expressions in Eqs. (4.14) and (4.15) were used in the relation of  $\varepsilon_m = \varepsilon_p$  and the results was as follows:

$$\frac{U_{0,p}^3}{U_{0,m}^3} = \frac{L_p}{L_m} \quad (4.16)$$

Assuming equal kinematic viscosity of water in the model and prototype scale, this equation was used to predict the following expression:

$$\frac{Re_p}{Re_m} = \left( \frac{L_p}{L_m} \right)^{4/3} \quad (4.17)$$

where,  $Re_p$  is the jet-Reynolds number in the prototype scale, and  $Re_m$  is the jet-Reynolds number in the model scale. This equation served the operating condition of the mixing tank in the prototype. The geometric length of the mixing tank in the prototype was determined by the ration of geometric length scales ( $L_m/L_p$ ) of the grit tank, because the width of the mixing tank was set same as the width of the grit tank.

The grit tank was proposed scale up based on Froude number similarity. The Froude numbers of the model and prototype are same, which results in the following relation:

$$\frac{U_p}{U_m} = \left( \frac{L_p}{L_m} \right)^{1/2} \quad (4.18)$$

where,  $U_p$  is the flow velocity of in the prototype and  $U_m$  is the flow velocity in the model scale. Eq.(4.14) was used to establish the relationship the smallest grit sizes in the model grit tank and porotype grit tank. The smallest grit size, ( $d_m$ ), which is removed completely in the model grit tank was related to the smallest grit size ( $d_p$ ), which is removed completely in the prototype grit tank. According to the Stockes' law, the settling velocity  $V_s$  is related to the grit size by the following:

$$V_{s,m} = \frac{(\rho_g - \rho)g}{18\mu} d_m^2 \quad (4.19)$$

The settling velocity, the overflow rate and horizontal velocities were assumed in the same order. Then, the above equation can be restated as,

$$\frac{d_m^2}{d_p^2} = \frac{V_{s,m}}{V_{s,m}} = \frac{U_p}{U_m} \quad (4.20)$$

Using the relationships in Eqs. (4.13) and (4.15), the grit size in the prototype can be expected by the following expression:

$$\frac{d_p}{d_m} = \left( \frac{L_p}{L_m} \right)^{1/4} \quad (4.21)$$

In the experiments, 95% of 44 micron grit was settled in the model grit tank. In the prototype grit tank, 95% of 87 micron grit size would be removed by the new grit removal system. The removal of the fine grit would lead to improved effectiveness of the downstream units.

#### **4.5 Conclusion**

A new grit removal system was tested to verify the effectiveness in removing grit and FOG. The system was effective because of the application of transverse jets in the square mixing tank. The transverse jets were applied with the layout B, jet-Reynolds number of 41600, and diameter of 5.3 mm. The results showed that the mixing tank with the transverse jets was able to significantly remove the concentration of suspended solid in the effluent water relative to the concentration in the influent water. In contrast, there were not significant differences between the concentrations of influent and effluent water in the tests without jets. This configuration and operating condition of the jets was able to clean grit particles in the square tank, and therefore, the effect of the cleaning was observed by the significant decrease of the influent concentrations of solids at the outlet. The reason of the good cleaning was the production of homogenous and strong turbulent mixing. Mixing was analogous to cleaning in a way that the more kinetic energy of the jets to the tank produced the more mixing in the flow. This led to the more energy dissipation and the more shear stresses in the flow. Therefore, a grit particle entering to the mixing tank was undergone through the shear stresses, which caused cleaning grit particles. This led to high percentage of grit removal efficiency. High percentage of fine particles was also removed in the system.

The success of this new grit removal system was the addition of mixing tank that splits the complexities of generating two opposite flows in an aerated grit tank. The existing capacity of the aerated grit tanks can be improved by using a prototype-mixing tank with multiple transverse jets. The uses of air jets are unnecessary for the existing WWTPs. This improvement would lead to increase the effectiveness and efficiencies of advanced treatment units, at the downstream of the grit removal units. This increase of advanced treatment units is necessary for addressing tougher effluent standard and serving more population.

## 4.6 Reference

American Society for Testing and Materials. (2000). "ASTM designation E 8-00 Standard Test Methods for Tension Testing of Metallic Materials." ASTM.

Anderson, R., and Holmberg, M. (2006). "Energy Conservation in Wastewater Treatment Operation." Lund University, Sweden: Master Thesis.

Andoh, R. Y. G., and Neumayer, A. (2009). "Fine Grit Removal Helps Optimize Membrane Plants." *WaterWorld*, 25(1), 28-28.

AWWA, A. (1998). "WPCF-Standard Method for Examination of Water and Wastewater." USA.

Brenner, A., and Diskin, M. H. (1991). "Model study of jet-circulated grit chamber." *J. Environ. Eng.*, 117(6), 782-787.

De Silva, V., and Bates, B. R. (2004). "Fine grit removal challenges in wastewater treatment plants." *Proceedings of the Water Environment Federation*, 2004(7), 258-264.

Edmonton Waste Management Center of Excellence (2012). "Grit Characterization at Gold Bar Wastewater Treatment Plant, Gold Bar Wastewater Treatment Plant, Edmonton

Gold Bar Wastewater Treatment Plant (2012). "Display Chart: Grit Tanks", Edmonton

El-Din, A. G., and Smith, D. W. (2002). "A neural network model to predict the wastewater inflow incorporating rainfall events." *Water Res.*, 36(5), 1115-1126.

Finger, R. E., and Parrick, J. (1980). "Optimization of Grit Removal at a Wastewater Treatment Plant." *Journal (Water Pollution Control Federation)*, 52(8), pp. 2106-2116.

Fouad, M., Kishk, A., and Fadel, A. (2014). "The effects of scum on sewer flows." *Urban Water Journal*, 11(5), 405-413.

Gruber, Y., Farchill, D., and Goldstein, M. (1988). "Design, Testing and Operation of Grit Chambers with Hydraulic Roll." *Water Science and Technology WSTED4 Vol. 20, no. 4/5, P 237-248, 1988. 6 Fig, 11 Ref.*

Habib, A. (2008). "Investigating the performance of an aerated grit chamber". University of Alberta, M.Sc. thesis, Canada.

Hendricks, D. W. (2006). *Water treatment unit processes: physical and chemical*. CRC press, .

Keane, J. J., and deSilva, V. (2009). "Dealing with Fine Grit at WWTPs." *Proceedings of the Water Environment Federation*, 2009(10), 6149-6159.

Kolmogorov, A. N. (1941). "The local structure of turbulence in incompressible viscous fluid for very large Reynolds numbers." *Dokl. Akad. Nauk SSSR*, 299-303.

Metcalf, I. N. C., and Eddy, H. (2003). *Wastewater engineering; treatment and reuse*. McGraw-Hill New York, .

Morales, L., and Reinhart, D. (1984). "Full-Scale Evaluation of Aerated Grit Chambers." *WPCF J*, 56(4), 337.

Munoz, A., and Young, S. (2009). "Two-dimensional model for predicting performance of aerated grit chambers." *Canadian Journal of Civil Engineering*, 36(9), 1567-1578.

Nawrocki, M. A. (1974). *A portable device for measuring wastewater flow in sewers*. Office of Research and Development, US Environmental Protection Agency;[for sale by the Supt. of Docs., US Govt. Print. Off.], .

Neighbor, J., and Cooper, T. (1965). "Design and Operation Criteria for Aerated Grit Chambers." *Water and Sew. Works*, 112 448.

Osei, K., Mody, A., and Andoh, R. Y. G. (2010). "Field assessment of grit removal systems." *World Environmental and Water Resources Congress 2010: Challenges of Change, May 16, 2010 - May 20*, American Society of Civil Engineers, Providence, RI, United states, 3756-3763.

Rajaratnam, N. (1976). *Turbulent jets*. Elsevier Science Limited, Elsevier.

Sawicki, J. M. (2004). "Aerated grit chambers hydraulic design equation." *J. Environ. Eng.*, 130(9), 1050-1058.

Spellman, Frank R.(2013). "Handbook of water and wastewater treatment plant operations". *CRC Press*,USA.

Von Sperling, M. (2007). *Wastewater characteristics, treatment and disposal*. IWA publishing, .

## Table

Table 4.1: Layouts ( $\Lambda$ ) showing the relative positions of cross jets by circles (open and closed), open circles are mounted on one sidewall and the closed on the opposite sidewall. Arrows are direction of mainstream flow.

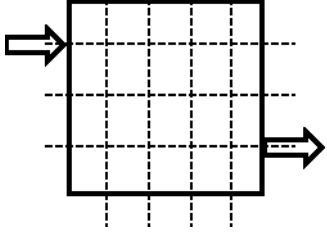
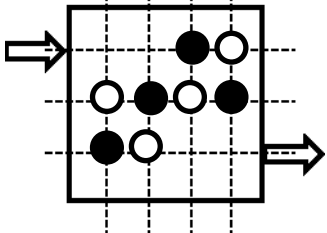
$\Lambda$	Description
A	
H	

Table 4.2: Test scenario for grit measurements at Gold Bar Wastewater Treatment Plant

Test No.	Layout	Reynolds number	Diameter of a jet (mm)
1	A	0	0
2	H	41 600	5.3

Table 4.3: Mean( $\mu$ ), probability (p-values), and efficiencies of removal ( $\eta$ ) of TSS, FSS and VSS, E0, E2 and E4 were the experiments without jets and E1, E3 and E5 were the experiments with jets. TSS stands for total suspended solid, FSS for fixed suspended solid and VSS for volatile suspended solid.

		E0	E2	E4	E1	E3	E5
	Degree of freedom	12	18	18	18	18	18
TSS	mean value (mg/L)	234	119	189	159	278	492
	p-value	0.0810	0.8289	0.2905	0.0000	0.0000	0.0000
	% of removal				29.4%	19.0%	36.8%
FSS	mean value (mg/L)	72	12	26	16	45	70
	p-value	0.8471	0.1952	0.6361	0	0	0
	% of removal				62.7%	21.9%	48.9%
VSS	mean value (mg/L)	162	106	163	143	234	422
	p-value	0.4803	0.0892	0.2512	0	0.0241	0
	% of removal				25.7%	18.4%	34.7%

Table 4.4: The fractions of volatile and fixed materials in solid and water phase, VS stands for total volatile solid, FS for total fixed solid and TS for total solid;  $f_{VS}$  and  $f_{FS}$  are fractions of volatile and fixed components in TSS, where TSS stands for total suspended solid, VSS for volatile suspended solid and FSS for fixed suspended solid.

Test	Scum sample		Grit sample		Water Phase	
	VS/TS	FS/TS	TVS/TS	TFS/TS	$f_{VS}$ (VSS/TSS)	$f_{FS}$ (FSS/TSS)
	mg/g	mg/g	mg/g	mg/g	mg/g	mg/g
E1	720	280	253	747	773	227
E3	745	255	449	551	861	139
E5	749	251	626	374	811	189
average	738	262	443	557	815	185

Table 4.5: Estimates of grit removal capacity of this system and Gold Bar Wastewater treatment plant, Edmonton

This new grit removal system					Gold Bar WWTP		
Amount of grit (observed)	Flow Rate	Duration	Total flow per day	Mass per Flow (MGD)	Grit per day by new model	Flow rate	Mass of Grit per Day
g	L/s	hr	MGD	kg/MGD	tons	MGD	tons
625	3.45	4	0.08	7.92	3.4	423	1.78

Table 4.6: Analysis of grit size distribution of the tests, Habib(2008) and EWMCoE(2012)

Parameters	E1	E3	E5	Habib (2008)	EWMCoE(2012)	
	Summer	Summer	Summer	Summer	Spring	Summer
$D_{10}$ ( $\mu\text{m}$ )	46	84	82	170	314	252
$D_{30}$ ( $\mu\text{m}$ )	89	138	137	280	436	374
$D_{50}$ ( $\mu\text{m}$ )	127	185	184	370	612	488
$D_{60}$ ( $\mu\text{m}$ )	146	207	207	450	895	547
$C_u$	3.16	2.46	2.52	2.65	2.8	2.17
$C_c$	1.18	1.09	1.10	1.02	0.8	1.01

## Figures



Fig. 34: Photo of experimental setup showing the components: (1) constant head tank, (2) mixing tank, (3) grit tank, (4) manifold for cross jets, (5) flow meter for the longitudinal flow and (6) flow meter for the transverse flow; Arrows show the flow direction.



Fig. 35: Imhoff cone experiment showing three samples of each of the two tests; Settleable grit is shown at bottom of the cones with black colors.

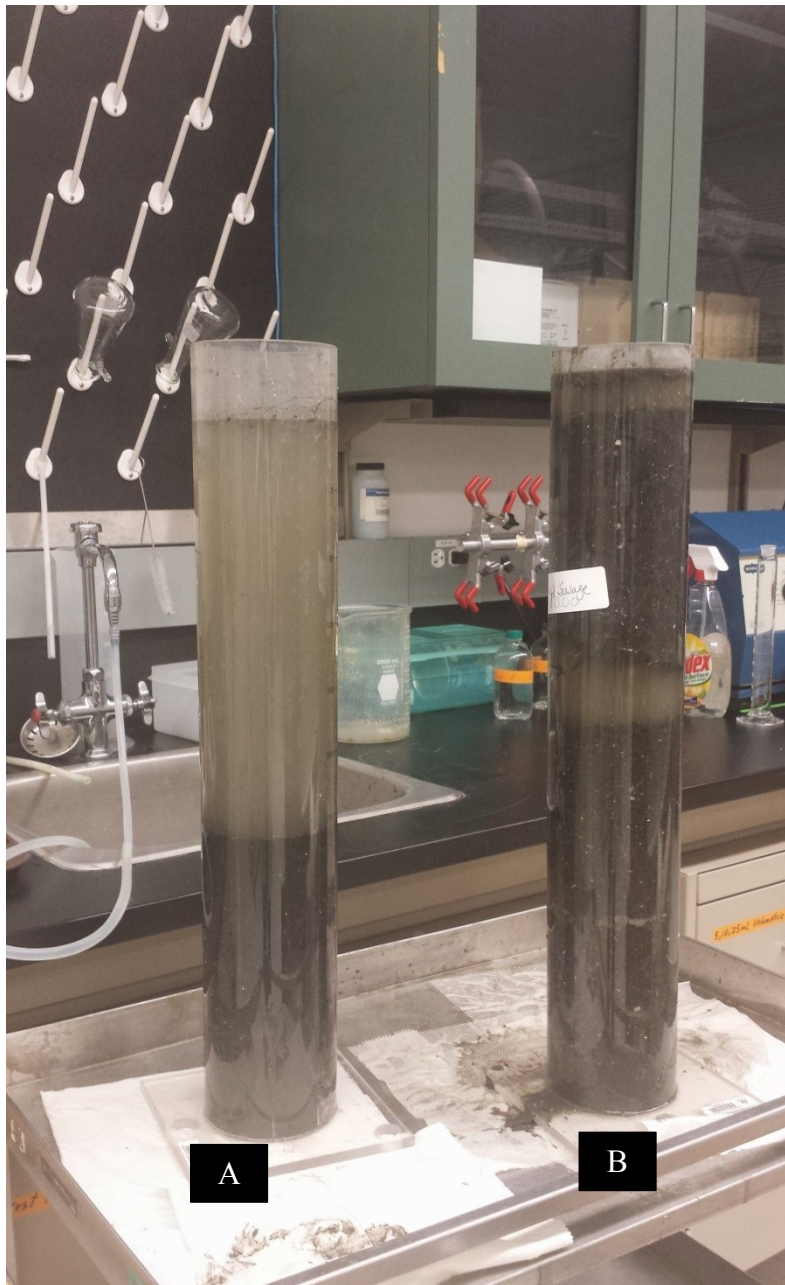


Fig. 36: Grit wash in a long settling tube, (A) shows final wash and (B) shows an initial wash of two samples.

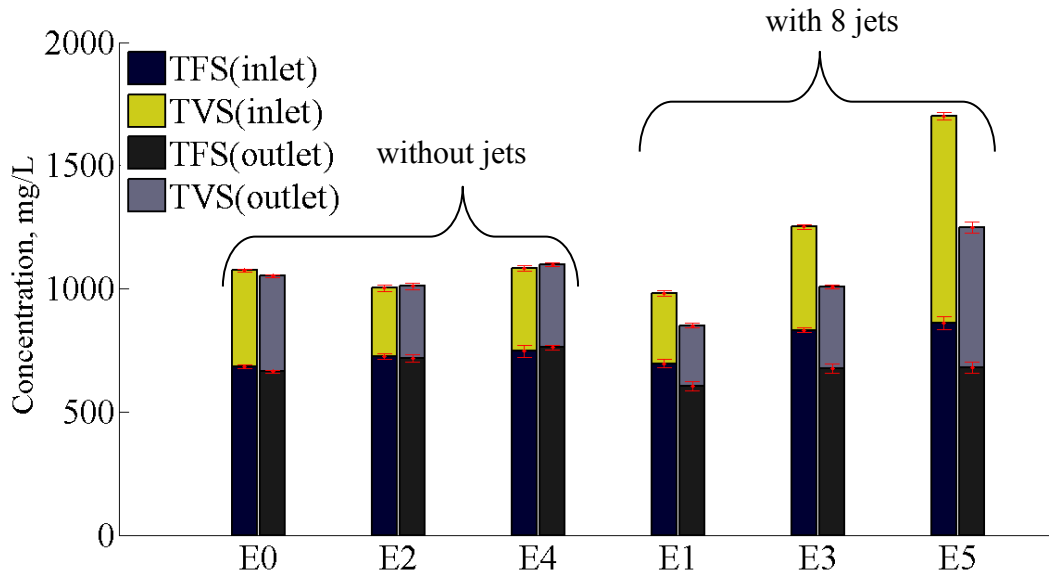


Fig. 37: Concentrations of TFS and TVS at inlet and outlet; TFS stands for total fixed solid and TVS stands for total volatile solid. Error bars represent corresponding margin of errors ; E0, E2 and E4 were the experiments without jets and E1, E3 and E5 were the experiments with jets

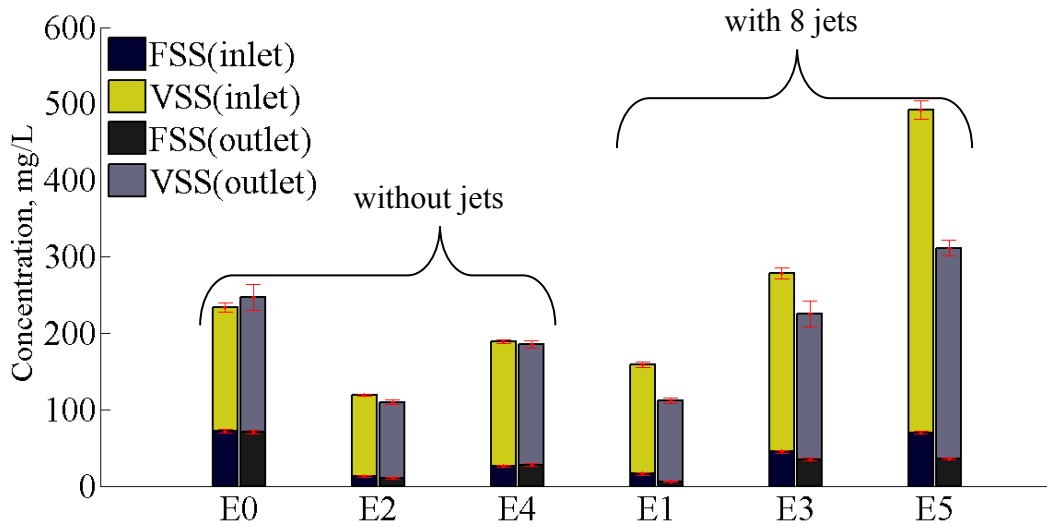


Fig. 38: Concentrations of FSS and VSS at inlet and outlet; FSS stands for fixed suspended solid and VSS stands for volatile suspended solid. Error bars represent corresponding margin of errors; E0, E2 and E4 were the experiments without jets and E1, E3 and E5 were the experiments with jets



Fig. 39: Entrance section of the grit tank showing scum layer on the top of the water.

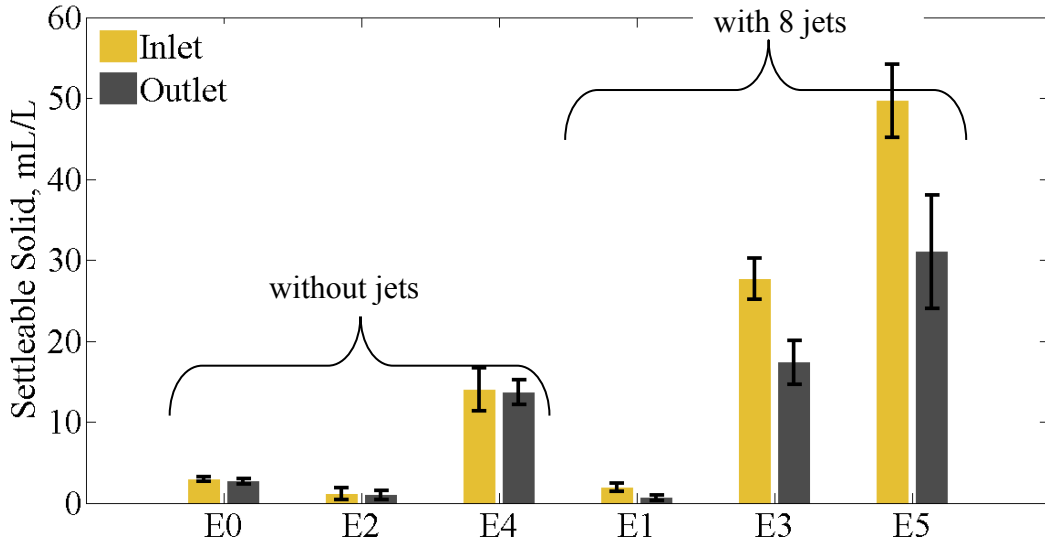


Fig. 40: Settleable solids measured by Imhoff settling cone in the experiments with and without transverse jets; E0, E2 and E4 were the experiments without jets and E1, E3 and E5 were the experiments with jets

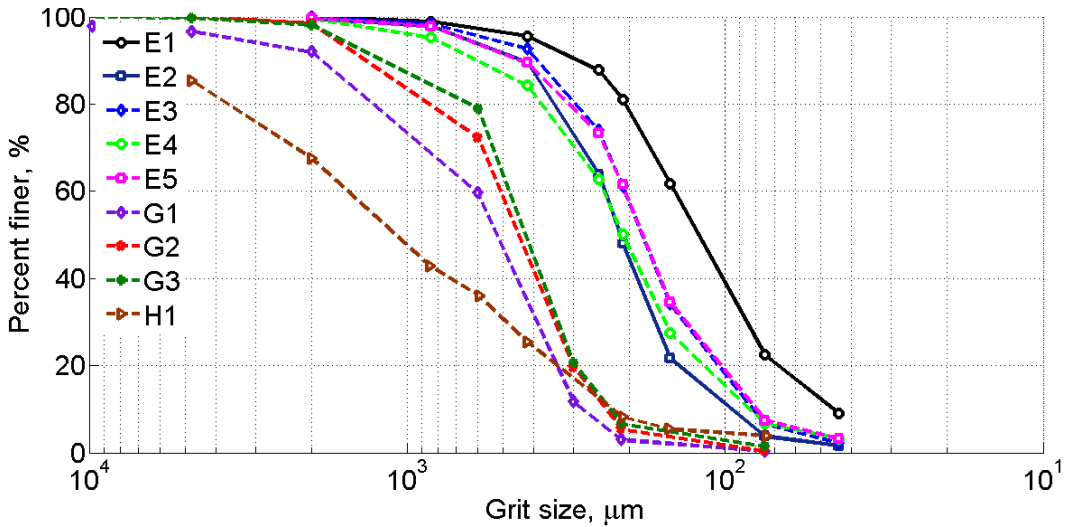


Fig. 41: Sieve analysis of grit deposit in the grit tank; E2 and E4 were the experiments without jets and E1, E3 and E5 were the experiments with jets; G1,G2 and G3 are the distributions of EWMCoE (2012) and H1 is the distribution of Habib(2008).

## Chapter 5 : Conclusion

### 5.1 Summary of Conclusion

The goal of the research was to develop an improved method of grit removal technology by introducing an additional mixing tank for separating fat, oil and grease (FOG) from grit using transverse jets. The configuration and operating conditions of the transverse jets, that is, the layout ( $\Lambda$ ), Reynolds number ( $Re$ ) and diameter ( $d$ ), were varied to achieve high mixing performance in the tank. The effects of varying  $\Lambda$ ,  $Re$ , and  $d$  were estimated using a dispersive compartmental model (DCM), not using conventional models, such as the axial dispersion model (ADM), the tank in series model (TiSM) and conventional compartmental model (CCM). The conventional models were found to be insensitive to these factors. The better performance of the DCM was due to the fact that it accounted for the dispersive nature of the plug flow compartment, which was not possible using any of conventional models.

The best jet configurations were found to be layouts B and H. The jet locations in these two layouts were away from inlets and outlets and, therefore, the jets penetrated into regions where the ambient velocities were low. The momentum ratio of the jet to ambient fluid was high at these locations. Moreover, the opposing jets which were offset from each other generated local eddies that increased mixing. Based on the tests of two jet diameters, larger diameter of jets produced higher mixed flow volumes. Increasing the jet-Reynolds number improved the mixing performance of the tank, but increasing the number of jets (more than 8 jets) did not improve the performance.

The mixing performance of layout A (no jets) and B were compared at various Reynolds number in Planar Laser Induced Fluorescence (PLIF) experiments. The results of the PLIF experiments showed that the mixing performance improved at Reynolds numbers larger than 16700. The DCM was applied to concentration time series data extracted from the PLIF images. The estimates of plug flow,

mixed flow and dead flow volumes were comparable with the volumes of RTD experiments at Reynolds numbers greater than 16700. This successful comparison indicated that the DCM could be used for validation of computational fluid dynamics models. In addition, these experiments enabled the location of dead flow zones in the measurement plane. Dead flow zones were observed in the upper right corner, which was the location in between the two outlets, and the lower right corner, which was a downstream corner of the tank. These locations were also the stagnant flow zones based on the geometric shape of the tank.

The new grit removal system was tested at Gold Bar Wastewater Treatment Plant (GBWWTP) to verify its effectiveness in removing FOG and enhancing grit removal. The transverse jet tests were conducted using the best layout, H and the Reynolds number of the jets was set at 41600. Using this configuration and operating condition the application of transverse jets was found to significantly reduce the concentration of suspended solids in effluent water. However, control tests conducted with no transverse jets showed that there were not significant differences between the concentrations of suspended solids in influent and effluent water. This is clear evidence that the new method increased the effectiveness of the grit removal system. The new system was able to remove 95% of 44  $\mu\text{m}$  and larger grit particles which is significantly better performance than commercial grit removal systems (De Silva and Bates 2004; Andoh and Neumayer 2009).

In the field experiments, the new technique was able to demonstrate that a large amount of grit with fine particles was settled and FOG in the form of scum was floated to the surface. If this new method was implemented at the Gold Bar WWTP it could potentially remove a total of 3.4 tons of grit per day based on the average treatment capacity of the plant. This amount of grit removal is significantly larger than the 1.78 tons per day that is removed by the existing system (GBWWTP, 2012).

The added advantage of the new technique is the extraction of FOG, which would have potential use as biofuel. FOG is not extracted from existing grit removal units (Von Sperling 2007), whereas this new grit removal system has a potential for early removal of FOG. Note that the amount of FOG was large in these field experiments because the influent water contained very fine particles and a high percentage of volatile material.

The new technique can be implemented in existing WWTPs by installing a prototype mixing tank upstream of an aerated grit tank. The aerated grit tank could then be operated without air jets because grit cleaning is performed in the mixing tank and therefore the downstream grit tank is only used for settling cleaned grit particles. The use of water jets could lead to reduce operational costs compared to the air jets required for aerated grit tanks. The new technique was able to remove fine particles and a large amount of grit that would increase the effectiveness and capacity of downstream treatment units (e.g. membrane bioreactors) in a WWTP. These types of improvements are required for addressing tougher effluent standards and in order to serve growing populations.

## **5.2 Recommendations**

The next logical step would be to conduct full-scale field tests to obtain additional measurements of the amount of grit removed using the new method under varying conditions. The geometric configuration of the full-scale system should be calculated using Froude number similarity that ensures gravity settlement of grit and floatation of FOG on water surface. The operating conditions of the full-scale jets should be determined by keeping the ratio of the Kolmogorov scale of turbulence and grit size the same as in the model.

The DCM was developed for single peak of E-curves and, therefore, it is not applicable to reactors that produce multiple peaks in their E-curves. The DCM could be modified to simulate multi-peak E-curves by adding multiple plug flow

and mixed flow compartments. The modified DCM would need to include more than two equations and be defined in more than two time intervals.

It is also important to confirm that the velocities in the dead flow zones in the full-scale mixing tank are sufficiently high to keep the grit suspended in the flow. Otherwise, grit settlement in the mixing tank may reduce its capacity. Velocity field can be studied by particle image velocimetry (PIV) and by applying CFD methods. CFD modelling could also be used for preliminary assessment of different tank geometries.

## **Reference**

De Silva, V., and Bates, B. R. (2004). "Fine grit removal challenges in wastewater treatment plants." *Proceedings of the Water Environment Federation*, 2004(7), 258-264.

Andoh, R. Y. G., and Neumayer, A. (2009). "Fine Grit Removal Helps Optimize Membrane Plants." *WaterWorld*, 25(1), 28-28.

Gold Bar Wastewater *Treatment* Plant (2012). "Display Chart: Grit Tanks", Edmonton

Von Sperling, M. (2007). *Wastewater characteristics, treatment and disposal*. IWA publishing.

## Appendix A

### Calculation of Scum and Grit

Table A.1: Calculations for the differences of concentration of TSS, VSS, and the ratio of VSS/TSS and FSS/TSS, TSS = total suspended solid, VSS = volatile suspended solid, FSS = fixed suspended solid

Test #	$\Delta$ TSS	$\Delta$ FSS	$\Delta$ VSS	VSS/TSS	FSS/TSS
	mg/L	mg/L	mg/L	mg/kg	
E1	47.06	10.71	36.36	772.53	227.47
E3	69.59	9.65	59.94	861.37	138.63
E5	180.78	34.22	146.56	810.69	189.31
Average	100.71	18.50	82.21	814.86	185.14

Table A.2: Calculation of volatile and fixed fraction in scum, grit and water samples, TSS = total suspended solid, VSS = volatile suspended solid, FSS = fixed suspended solid, VS = volatile solid, FS = fixed solid and TS = total solid

Test #	Scum sample		Grit sample		Water Sample	
	VS/TS	FS/TS	VS/TS	FS/TS	VSS/TSS	FSS/TSS
	mg/g	mg/g	mg/g	mg/g	mg/g	mg/g
E1	720	280	253	747	773	227
E3	745	255	449	551	861	139
E5	749	251	626	374	811	189
Average	738	262	443	557	815	185

Table A.3: Calculation of grit mass, FSS = fixed suspended solid, FS = fixed solid, and GBWWTP = Gold Bar Wastewater Treatment Plant, MGD = million gallon per day

Flow rate	L/s	3.45
Total flow per day	MGD	0.079
Duration	hr	4
$\Delta$ FSS	mg/L	18.5
Fraction of FS in grit		0.68
Amount of grit	g	625.13
Mass per Flow	kg/MGD	7.93
Daily average Flow of GBWWTP	MGD	423
Yearly grit collection in GBWWTP	ton	650
Mass of grit per day in GBWWTP	ton	1.78
Mass of grit by new model for average flow of GBWWTP	ton	3.34

Table A.4: Calculation of scum mass, FSS = fixed suspended solid, FS = fixed solid, and GBWWTP = Gold Bar Wastewater Treatment Plant, MGD = million gallon per day

Flow rate	L/s	4.85
Duration	hr	1.00
$\Delta$ VSS	mg/L	82.21
fraction of VS in scum		0.63
Amount of scum	g	897.25
Size of scum	cm	43.00
	cm	80.00
Area of scum (observed)	cm <sup>2</sup>	3440.00
Density of Scum	mg/cm <sup>3</sup>	950.00
Thickness of Scum	mm	2.75
Thickness of scum by (Nawrocki 1974)	mm	6.25

Nawrocki, M. A. (1974). *A portable device for measuring wastewater flow in sewers*. Office of Research and Development, US Environmental Protection Agency.

## Appendix B

### Noise Removal of Resident Time Distribution Measurements

Time series of digital voltage signals from the conductivity meters were sampled at 400 Hz for a duration of approximately 5 min. The voltage signals were converted to concentrations by applying calibration factors. This is raw concentration consisting of noise as shown in Fig. B1. The plot shows noises in the both time series.

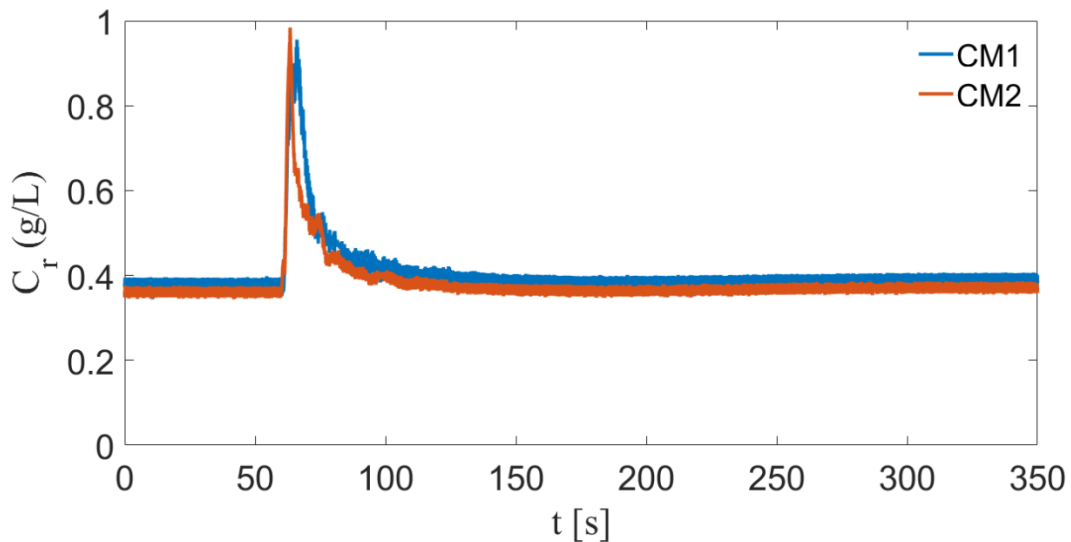


Fig. B1. Time series of raw concentration,  $C_r$  for a single RTD measurement [ $A = B$ ,  $Re = 5345$ ,  $d = 5.3$  mm, run number 02, CM1: conductivity meter 1, CM2 = conductivity meter 2, injection time is 58.3s.]

Fig. B2 shows estimates of the power spectral density (PSD) function made using the *pwelch* command (Welch's method) in MATLAB. The time series was divided into segments of 256 data points, a 256 long Blackman tapering window was applied and 50% overlap was used between adjacent segments. The amplitude of the PSD function was high ( $\sim 10^{-3}$  dB/Hz) at frequencies lower than 5 Hz whereas at frequencies greater than 5 Hz the amplitudes were approximately four orders of magnitude lower ( $\sim 10^{-7}$  dB/Hz). Therefore, the cutoff frequency at

5 Hz was correct choice. The justification of the cut off frequency was verified by observing the data prior to injecting tracer.

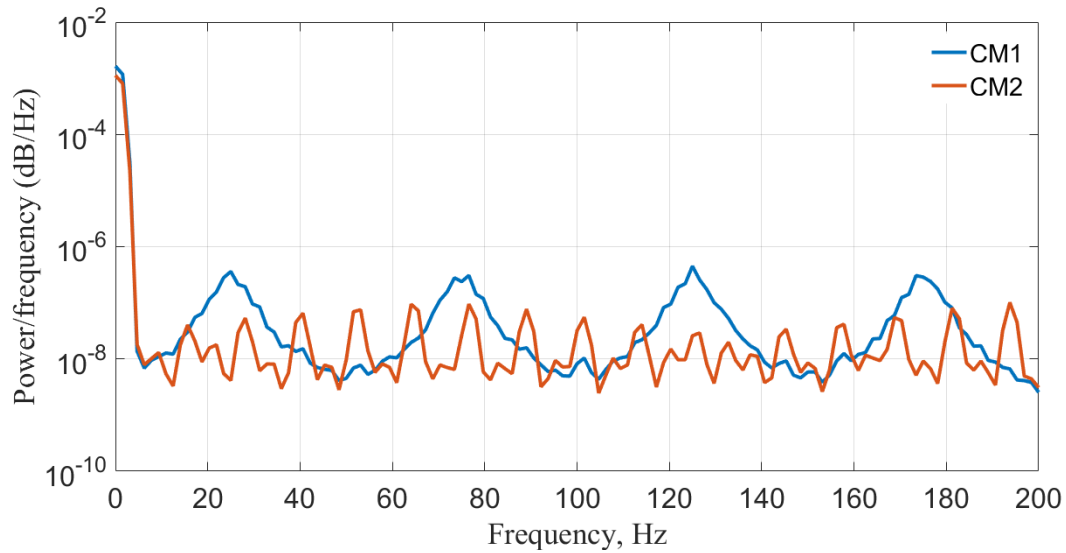


Fig. B2: Estimates of power spectrum density of the entire data-series by using *pwelch* tool in MATLAB with a “blackman” window of 256 data-size and 50% overlap [CM1: conductivity meter 1, CM2 = conductivity meter 2].

Fig. B3 is a plot of the time series of concentration prior to injecting the tracer. The concentration prior to injecting the tracer should be a constant value and, therefore, any time varying signals will be background noise. The standard deviation of the background noise of the signals plotted in Fig. B3 is 3.2 mg/L for CM1 and 1.9 mg/L for CM2. Typical noise levels ranged from 1.2 mg/L to 4.0 mg/L and these values are very small compared to the signal amplitudes observed when the tracer was injected. The PSD was plotted for this data in Fig. B4. The plot shows the amplitude of the PSD is  $\sim 10^{-7}$  dB/Hz, which was similar amplitudes observed in Fig. B2 at frequencies greater than 5 Hz.



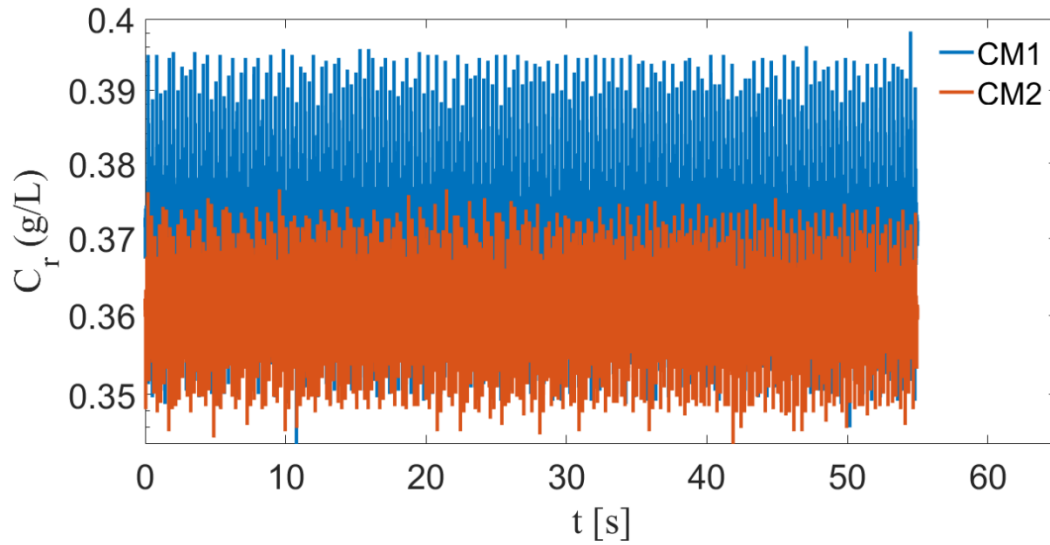


Fig. B3: Time series of concentration  $C_r$  prior to injecting tracer showing noise signals from conductivity meters [CM1: conductivity meter 1, CM2 = conductivity meter 2 ].

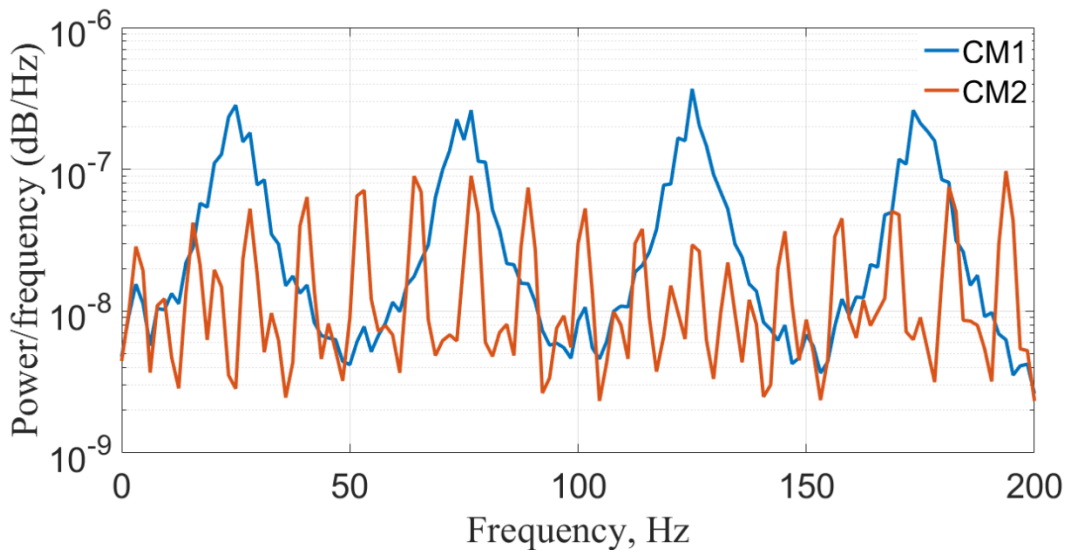


Fig. B4: Estimates of power spectrum density of the data prior to injecting tracer by using *pwelch* tool in MATLAB with a “*blackman*” window of 256 data-size and 50% overlap [CM1: conductivity meter 1, CM2 = conductivity meter 2].

Based on this analysis an 8<sup>th</sup> order “*Butterworth*” low-pass filter with a cutoff frequency of 5 Hz was used to pre-process the raw concentration time series. In Fig. B5 time series of the filtered concentration time series of the data from Fig. B1 is plotted. This plot clearly shows that noise was removed if it is compared with the plot in Fig. B1.

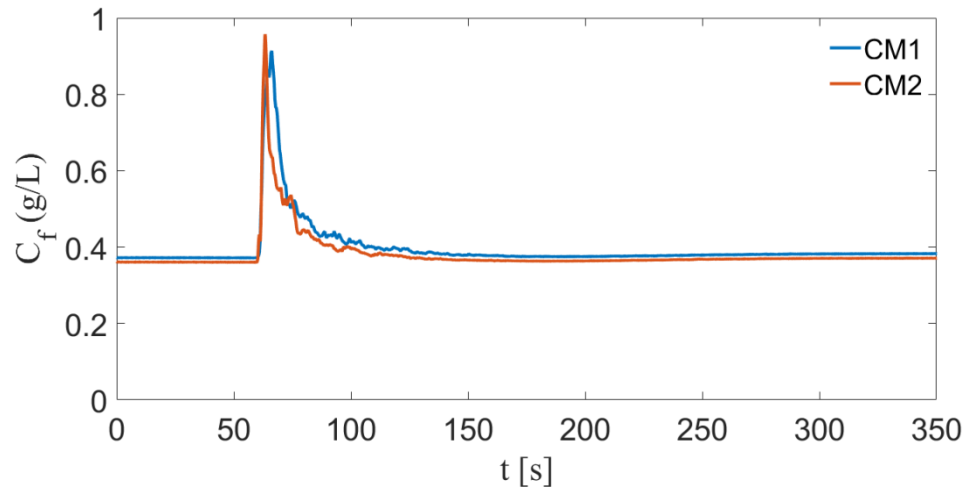


Fig. B5: Time series of filtered concentration,  $C_f$  for a single RTD measurement [ $A = B$ ,  $Re = 5345$ ,  $d = 5.3$  mm, run number 02, CM1: conductivity meter 1, CM2 = conductivity meter 2, injection time is 58.3s.]

In Fig. B6 the PSD of the raw and filtered concentration time series are compared. As expected the amplitudes of the raw and filtered are identical for frequencies less than 5 Hz. The plot also shows that the low-pass filter effectively removes all signals with frequencies greater than 5 Hz.

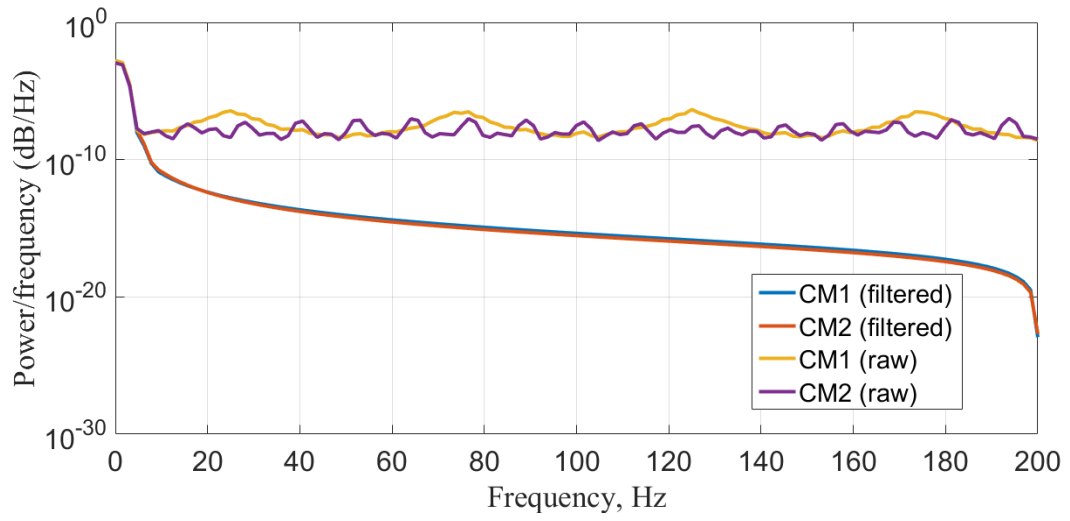


Fig. B6: Power spectrum of the filtered and raw concentration, where cutoff frequency was set at 5 Hz [CM1: conductivity meter 1, CM2 = conductivity meter 2].